INVESTIGATION OF THE AEROTHERMODYNAMICS OF HYPERVELOCITY REACTING FLOWS IN THE RAM ACCELERATOR

A. Hertzberg
A.P. Bruckner
A.T. Mattick
C. Knowlen

INVESTIGATION OF THE AEROTHERMODYNAMICS OF HYPERVELOCITY REACTING FLOWS IN THE RAM ACCELERATOR

A. Hertzberg
A.P. Bruckner
A.T. Mattick
C. Knowlen

Aerospace and Energetics Research Program
University of Washington
Seattle, WA 98195

December 28, 1992

ABSTRACT

New diagnostic techniques for measuring the high pressure flow fields associated with high velocity ram accelerator propulsive modes have been experimentally investigated. Individual propulsive modes are distinguished by their operating Mach number range and the manner in which the combustion process is initiated and stabilized. Operation of the thermally choked ram accelerator mode begins by injecting the projectile into the accelerator tube at a prescribed entrance velocity by means of a conventional light gas gun. A specially designed obturator, which is used to seal the bore of the gun, plays a key role in the ignition of the propellant gases in the subsonic combustion mode of the ram accelerator. Once ignited, the combustion process travels with the projectile and releases enough heat to thermally choke the flow within several tube diameters behind it, thereby stabilizing a high pressure zone on the rear of the projectile. When the accelerating projectile approaches the Chapman-Jouguet detonation speed of the propellant mixture, the combustion region is observed to move up onto the afterbody of the projectile as the pressure field evolves to a distinctively different form that implies the presence of supersonic combustion processes. Eventually, a high enough Mach number is reached that the ram effect is sufficient to cause the combustion process to occur entirely on the body. Propulsive cycles utilizing on-body heat release can be established either by continuously accelerating the projectile in a single propellant mixture from low initial in-tube Mach numbers (M<4) or by injecting the projectile at a speed above the propellant's Chapman-Jouguet detonation speed. The results of experimental and theoretical explorations of ram accelerator gas dynamic phenomena and the effectiveness of the new diagnostic techniques are presented in this report.

ACKNOWLEDGMENTS

TABLE OF CONTENTS

LIST OF FIGURES

SECTION I

INTRODUCTION

At the University of Washington, theoretical and experimental research is being carried out on a ramjet-in-tube projectile launcher concept called the "ram accelerator."[1-19] This device accelerates projectiles with propulsive cycles that are similar to the aerothermodynamic cycles of airbreathing ramjets or scramjets. A projectile resembling the centerbody of a supersonic ramjet (Figs. 1-3) is accelerated through a stationary tube filled with a premixed gaseous fuel-oxidizer mixture. The projectile itself carries no propellant. Flow field phenomena arising from the passage of the supersonic projectile stabilize a combustion process such that it travels with the projectile, generating a pressure distribution which continuously produces thrust. The chemical energy density and speed of sound of the gaseous propellant mixture can be adjusted (via pressure and composition) to control the Mach number and acceleration history experienced by the which can, in principle, be easily scaled up in size for a number of interesting applications; e.g., high kinetic energy impact studies, hypersonic testing at nearly full scale,[19,20] long range defense, and direct launch to orbit.[21-23]

Several modes of ram accelerator propulsion have been investigated experimentally and theoretically by the authors and their colleagues. One of these propulsive cycles is the thermally choked ram accelerator mode (Fig. 1), which operates with in-tube Mach numbers typically ranging from 2.5 to 4 and at projectile velocities below the Chapman-Jouguet (CJ) detonation speed of the propellant mixture.[2-4] In this mode the thrust is provided by the high projectile base pressure resulting from a normal shock system that is stabilized on the body by thermal choking of the flow at full tube area behind the projectile. The one-dimensional theoretical model of the thermally choked propulsive mode predicts that the normal shock recedes along the body as the projectile Mach number increases. In the hypothetical case where the projectile tail tapers to a point and the flow is inviscid, the normal shock gradually falls back to the full tube area. A normal shock in a constant area duct, followed by heat addition and thermal choking in steady flow, constitutes a CJ detonation wave. Thus, theory predicts that the thrust goes to zero as the projectile velocity approaches the CJ detonation speed of a particular propellant mixture.

While a projectile is accelerating up to approximately 85% of the CJ detonation speed of the propellant mixture, it has been observed that the thrust as a function of Mach number is accurately predicted by the one-dimensional theoretical model of the thermally choked propulsive mode. At projectile velocities above 85% of the CJ detonation speed, however, the thrust typically begins to exceed that predicted by the theoretical model, reaching a relative minimum at velocities near 95%

CJ speed, and then tends to increase with increasing velocity.[5-10] This anomalous thrust (in the context of thermally choked theory) coincides with the experimental observation of combustion activity occurring on the projectile body. The schematic in Fig. 2 shows generalized heat addition regions located on and behind the projectile that could contribute to the net thrust at velocities near the CJ speed. Experiments have shown that in this "transdetonative" velocity regime (typically Mach 4 to 6), the projectile can accelerate smoothly from velocities below to above the CJ speed of a propellant mixture. This transdetonative behavior was an unexpected experimental finding that has significant implications for enhancing the muzzle velocity of single-stage ram accelerators and reducing the number of propellant mixtures required in multi-stage facilities.

For accelerating projectiles at even higher Mach numbers several "superdetonative" ram accelerator modes have been investigated both theoretically and experimentally.[2,5,7-10,16-18] These modes operate at velocities greater than the CJ speed of the propellant mixture. One proposed supersonic combustion process that results in thrust involves shock-induced combustion, wherein the propellant mixture is ignited by one of several reflected oblique shock waves within the flow region between the projectile and tube wall, as shown in Fig. 3. The supersonic heat release raises the gas pressure on the afterbody of the projectile, resulting in thrust as the reacted propellant expands back to full tube area. Other combustion processes capable of providing thrust at superdetonative velocities have also been suggested, such as oblique detonation and mixed-mode combustion cycles (e.g. heat addition processes that occur in both subsonic and supersonic regions of the flow field). Superdetonative operation can, in principle, accelerate projectiles to nearly three times the detonation velocity of hydrogen-oxygen propellant mixtures, which corresponds to velocities in excess of 10 km/sec.[2,16-18]

Experiments have been conducted in the University of Washington ram accelerator facility at Mach numbers ranging from 2.5 to 8.5, using a wide variety of propellant compositions at fill pressures of 3 to 50 atm absolute.[1-15] The thermally choked propulsive mode has been investigated at velocities of 0.7 to 2.7 km/sec and Mach numbers of 2.5 to 4. Transdetonative experiments have accelerated projectiles, which were initially propelled by the thermally choked mode, to exit velocities corresponding to Mach 6 in methane-based propellant mixtures, achieving single-stage velocity gains as high as 1 km/sec. Many different propellant mixtures have demonstrated the ability to accelerate projectiles smoothly through their respective CJ speeds to superdetonative velocities. Exploratory experiments conducted entirely in the superdetonative velocity range of an ethylene-based propellant mixture have demonstrated positive thrust at Mach numbers up to 8.5, which corresponds to a maximum velocity equal to 150% CJ speed. Data from investigations on the three propulsive modes discussed above indicate that the acceleration

performance in each velocity regime is characterized by distinctively different pressure and luminosity phenomena which provide clues as to the nature of these propulsive cycles.

Prior and concurrent experimental work at the University of Washington (partially funded by USAF, NASA, ONR, DOE, and Olin Corporation) has demonstrated the feasibility of several ram accelerator propulsive modes and has verified the scaling laws with respect to velocity, fill pressure, projectile mass, acceleration and ballistic efficiency in the velocity range of 0.7 to 2.5 km/sec.[24,25] The NASA-sponsored research program described here has emphasized the development of new diagnostic techniques and means for improving the capabilities of the current sensors. This report discusses the status of the diagnostic techniques investigated to date, their contribution to the current interpretation of ram accelerator phenomena observed in all three operating velocity regimes, and the latest results of the theoretical investigations. A brief review of the Hugoniot theory of ram accelerator performance is presented in Section II. Details of the ram accelerator research facility, its current sensors, and new instrumentation are described in Section III. Data from recent experiments are presented and discussed in Section IV along with preliminary results from the new diagnostic techniques. Appendix A provides additional information on the development and application of the Hugoniot analysis to the ram accelerator.
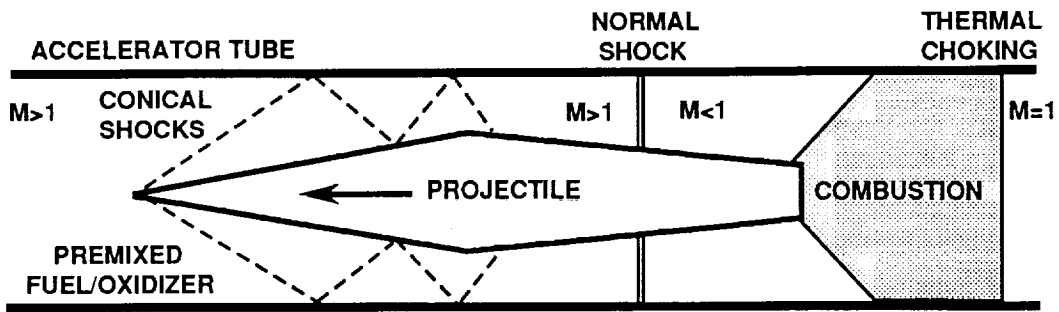
Fig. 1   Thermally choked ram accelerator propulsive cycle with subsonic combustion.
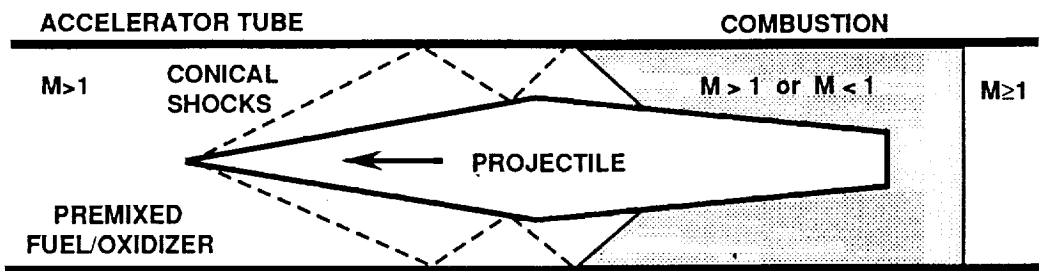
Fig. 2   Transdetonative ram accelerator propulsive cycle with mixed-mode combustion.
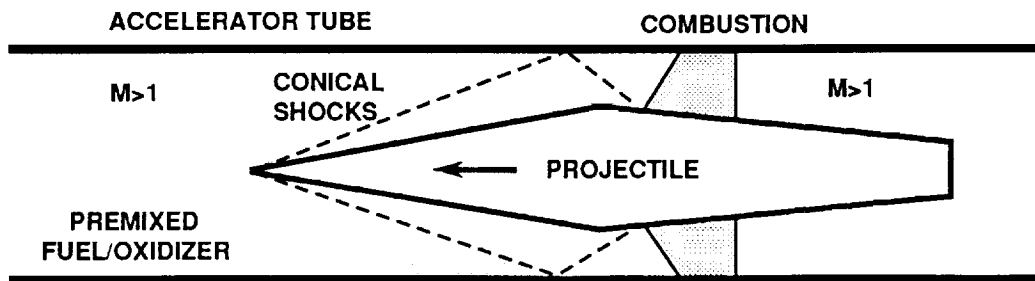
Fig. 3   Superdetonative ram accelerator propulsive cycle with supersonic combustion.

SECTION II

RAM ACCELERATOR HUGONIOT THEORY

The extraordinarily good agreement between the thrust predicted by the one-dimensional Hugoniot model of the thermally choked propulsive mode and the experimentally determined thrust at projectile velocities below the CJ speed, as noted in prior publications and contract reports, has been explained by recent theoretical investigations.[26,27] For accelerations up to 30,000g, it has been shown that a steady flow Hugoniot analysis of a control volume containing an arbitrarily shaped projectile (Fig. 4) can be used to determine the end state properties of the reacted propellant mixture as a function of the initial conditions and in-tube Mach number.[11] If the flow is assumed to exit the control volume at sonic velocity (with respect to the control volume) then the chemical equilibria and stream thrust (defined here as the sum of the static pressure and momentum flux) of the exhaust gas are uniquely constrained by the gasdynamic conservation equations. Thus, if the reacted propellant mixture is in thermodynamic equilibrium at the thermal choking point, it is unnecessary to know the details of the flow field when predicting the thrust on the projectile.

One of the most counter-intuitive aspects of thermally choked operation is the insensitivity of the projectile thrust to the aerodynamic efficiency of the supersonic diffuser. Indeed, the projectile acceleration is to a high degree independent of its geometry, as long as the flow area around the projectile throat (defined here as the point of maximum projectile cross-sectional area) is large enough to accept the incoming gas flow yet small enough to keep the normal shock train on the rear half of the projectile. This invariance of thrust with aerodynamic efficiency is a consequence of operating a propulsive cycle that is stabilized with an end state that corresponds to an entropy extremum (i.e., thermal choking). In the quasi-one-dimensional model of the thermally choked mode there is a normal shock that can move on the projectile body to compensate for non-isentropic flow field phenomena, whereas in actuality, there is a complicated pressure-coupling between the combustion region and the shock system on the rear half of the projectile. Regardless of the details of the flow around the projectile, the thermally choked ram accelerator has a unique end state condition that satisfies the conservation equations and, consequently, a unique thrust-velocity profile for every propellant mixture.

The general expression for the quasi-steady thrust (F) of any ram accelerator mode is determined from the one-dimensional gasdynamic conservation equations as a function of projectile in-tube Mach number (M_1) and the relative Mach number of the flow leaving the projectile (M_2), as follows:[27]

$$\frac{F}{AP_1} = \frac{\gamma_1 M_1}{\gamma_2 M_2}\left(1 + \gamma_2 M_2^2\right)\sqrt{\left(\frac{\gamma_2-1}{\gamma_1-1}\right)\frac{1+\frac{\gamma_1-1}{2}M_1^2+Q}{1+\frac{\gamma_2-1}{2}M_2^2} - \left(1+\gamma_1 M_1^2\right)} \qquad (2.1)$$

where P_1 is the propellant fill pressure, A is the tube cross-sectional area, γ_1 and γ_2 are the specific heat ratios before and after projectile passage, respectively, and Q is a nondimensional heat parameter defined as the ratio of the combustion heat release (Δq) to the product of the constant pressure heat capacity (c_{p1}) and static temperature (T_1) of the undisturbed propellant mixture, i.e., $Q = \Delta q / c_{p1} T_1$.

This thrust coefficient equation applies to all ram accelerator propulsive modes operating in a quasi-steady manner, even though no details of the internal flow have been considered.[26] If one knows how M_2 varies with M_1 in a given propellant mixture, then the projectile thrust can be readily estimated for any flight velocity. In addition, Eq. 2.1 indicates that the thrust increases with increases in the heat release parameter for a given γ_1, γ_2, M_1 and M_2. The details of the flow field around the projectile must be considered to accurately predict M_2 for the propulsive cycles operating in the transdetonative and superdetonative velocity regimes. However, thermal choking of the flow behind the projectile ($M_2 = 1$) corresponds to a state of maximum entropy, thus, the details of the process which brings the flow to choking do not affect the end state conditions of the thermally choked ram accelerator mode, and hence, do not have to be known to predict the thrust. A more complete discussion on the Hugoniot model of ram accelerator propulsive modes can be found in Appendix A.

ACCELERATOR TUBE

$M_1 > 1$

$M_2 \geq 1$

Q

F →

**Premixed
Fuel / Oxidizer**

**Combustion
Products**

1

2
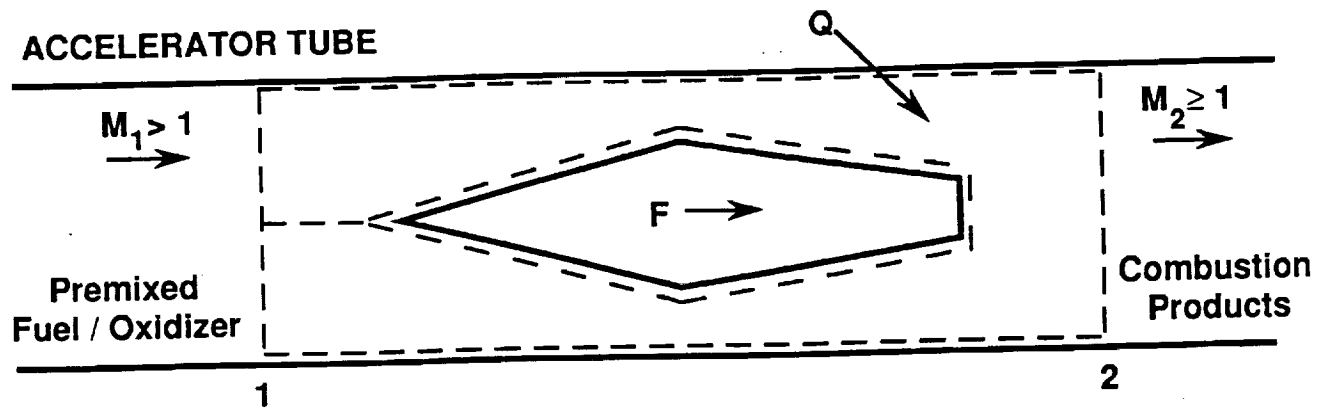
Fig. 4   Control volume for Hugoniot analysis of ram accelerator performance in the

projectile's frame of reference. Projectile exerts force on control volume in

the opposite direction of its motion.

SECTION III

EXPERIMENTAL FACILITY

The ram accelerator facility consists of a light gas gun, ram accelerator test section, final dump tank and projectile decelerator (Fig. 5).[28] The 38-mm bore, 6-m long, single-stage helium gas gun is capable of accelerating the obturator and projectile combination (typical combined mass of 60-100 g) to velocities up to 1.3 km/sec at a maximum breech pressure of 340 atm. The muzzle of the light gas gun is connected to a perforated-wall tube that passes through an evacuated tank which serves as a dump for the helium driver gas. A pair of opposing instrument ports is located 12.7 cm from the muzzle of the helium vent tube which enables monitoring the residual muzzle pressure and the time-of-passage of the projectile before it enters the test section.

1. RAM ACCELERATOR TEST SECTION

The 16-m long ram accelerator test section consists of eight 2-m long, 4150 alloy steel tubes having a bore of 38 mm and an outer diameter of 102 mm. There are a total of 144 instrumentation ports at 40 equidistant intervals along the test section of the ram accelerator. Each of the tubes has five instrument stations located at 40 cm intervals, three stations have four ports at right angles to each other and two stations, located between the four-port stations, have three ports separated by 120°. This design of multiple-port stations permits the simultaneous use of either three or four transducers for examining flow field phenomena. Diametrically opposed ports also provide the ability to observe asymmetries that may exist in the flow about the projectile. The dimensions of the instrument ports are such that standard piezoelectric pressure transducers (6.35 mm diameter access hole to the side-wall of the internal bore) can be located in any of these observation stations. Remaining ports are used to mount electromagnetic transducers and fiber-optic light guides and the unused ports are sealed with solid steel plugs. A more detailed discussion of these transducers is provided later in this section of the report.

The ram accelerator test section has been designed to operate at a maximum fill pressure of 50 atm. Thin Mylar diaphragms, ranging in thickness from 0.2 mm to 1.6 mm, are placed in the tube joints to seal each end of the ram accelerator test section and to separate tube segments filled with different propellant mixtures. The current facility is configured to operate with four stages and additional staging capability can be added as needed. The individual propellant gases are metered with sonic metering valves, brought together to mix, and then routed to the appropriate tube segments. Propellant mixture composition is validated by gas chromatography.

8

2. PROJECTILE DECELERATOR SECTION

The end of the ram accelerator test section is connected by a 0.76 m long drift tube of similar bore to a 2.4-m long evacuated dump tank, through which the projectile flies unconstrained. Two instrument stations, each having one pair of opposing instrument ports, are located in the drift tube to provide a final velocity measurement and to examine the pressure field about the projectile as it exits the test section. The first station in the drift tube is 35.8 cm from the end of the ram accelerator test section and the interval to the second instrument station is 34.9 cm. The final dump tank has an opposing set of 25 cm diameter viewing ports for high-speed photography and additional velocity measurements. The projectiles are brought to a stop by impacting metal witness plates and tightly packed rug remnants contained in a mild steel decelerator tube located within the far end of the dump tank. The decelerator tube has internal dimensions of 20 cm bore by 1 m long, and its wall thickness is 2.5 cm. The end of the decelerator tube is closed off by means of a 15 cm thick plate of 4150 steel alloy.

3. HIGHLY INSTRUMENTED TUBE SECTION

The 40 instrumentation stations in the ram accelerator test section are equidistant from each other when all eight tubes are joined together, resulting in an axial separation distance of 40 cm between stations. This is a very coarse instrumentation density, which has little ability to resolve details of the flow field phenomena occurring during some of the transient events that are of interest (e.g., mixture transitions, combustion initiation, unstarts, etc.). To enable detailed observations of the unsteady wave motions and projectile orientation effects, a short section of tube was manufactured with eight instrument stations located 2 cm apart in a 20.3 cm long tube segment (Fig. 6). Each instrumentation station has four orthogonal ports that are rotated 45° with respect to each other, resulting in a total of 32 instrument ports. The close spacing of the ports allows several transducers to simultaneously monitor the flow field at the tube wall from various axial and azimuthal locations around the projectile, in addition to being able to monitor events occurring within one half of a tube diameter before or after a diaphragm. The highly instrumented tube section is dimensioned to fit between any of the standard tube segments and is designed to operate at the maximum fill pressure of the test section.[14]

4. EXPERIMENTAL PROJECTILE CONFIGURATION

A schematic of the nominal projectile geometry used in most experimental work to date is illustrated in Fig. 7. The projectile is fabricated in two hollow pieces, nose cone and body, which thread together at the throat. The hollow design reduces the projectile mass and allows experiments to be conducted at moderate fill pressures. The projectiles have been manufactured

with masses ranging from 45 to 100 g, depending on variations in projectile material and structural details. The fins serve to center the projectile in the tube and the octagonal cross section of the body is simply a machining convenience. Annular magnets are mounted in the nose-body joint and in the body cavity at the base of the projectile. These magnets induce signals in the tube-mounted electromagnetic sensors, thus providing data on the time-of-passage of these reference points.

Most experimental projectiles to date have been fabricated from either magnesium alloy (ZK60-AT5) or aluminum alloy (7075-T6). Until recently these projectiles were manufactured in-house by our own machine shop. Due to machinery tolerance, however, discrepancies existed between individual, theoretically identical projectiles, resulting in mass variations of up to 4%. In an investigation of whether these discrepancies affect projectile performance, computer numerically controlled (CNC) machined projectiles (average mass variation of 0.1%) were used in some of the experiments. These ram accelerator experiments did not reveal significant performance differences between the CNC projectiles and the in-house machined projectiles.

(a) Nose Cone

The primary variables considered in the design of the nose cone are the cone half-angle and mass distribution. Nose cones with large half-angles (>15°) tend to reduce the upper operating Mach number limit of the thermally choked ram accelerator mode due, possibly, to pre-ignition of the propellant mixture by one of the reflected conical shock waves. Experiments have indicated that nose cones with a small half-angle (<8°) result in excessively long and heavy noses that move the projectile's center of gravity (CG) ahead of the fin leading edge for projectiles having the nominal body length of 72 mm. This is believed to reduce the upper velocity potential due to asymmetric pressure forces on the nose arising from a canted projectile. Wide operating Mach number ranges have been observed with projectiles having nose cone half-angles between 8° and 12.5°. The nominal nose cone currently being used has a half angle of 10° and a base diameter of 30 mm (Fig. 7).

It has been calculated that the nose tip requires less wall thickness than its base to withstand the experimental pressures. Consequently, the nose cones have a smaller internal angle than the exterior angle, in order to provide a wall thickness which decreases toward the nose tip. The depth of internal coning is a primary factor in determining the CG of the nose cone and, consequently, it is a factor in the location of the overall CG of the assembled projectile.

10

(b) Body Configuration

The design of the projectile body involves many variables. Material properties, CG location, external geometry and aerodynamic effectiveness are all factors considered in the design of the appropriate body configuration. Desirable mechanical properties of the body material include high strength-to-mass ratio, low chemical reactivity in a reducing atmosphere (most propellant mixtures used have been fuel rich) and high temperature capability. In addition, materials having high impact and abrasion resistance are desirable to reduce the amount of fin erosion that the projectile experiences.

The primary body geometry variables that interact with the flow are: the fin dimensions and their leading edge configuration (e.g., blunt or sharp), the body length, and the effective throat and base diameters (i.e., the diameter of a circle having an area equal to the actual cross-sectional area). The leading edges of the fins affect the area profile in the region behind the throat and also interact with the system of reflected conical shock waves generated between the cone and tube wall. Fin thickness is a significant contributor to the flow area profile along the body. The body length determines fin length (for a given leading fin edge geometry) and the distance between the recirculating zone at the base of the projectile and the projectile throat. Body length and nose cone half-angle determine the turning angle of the flow around the nose-body joint for different projectiles having the same base and throat cross-sectional areas. The nominal projectile has a body length of 72 mm and a fin thickness of 3.8 mm, with a fin leading edge rake angle of 12.5°. The fins are dimensioned for a diametric clearance of 0.1 mm between the projectile and the tube wall.

The nose cone base diameter normally sets the maximum effective diameter of the projectiles used in the experiments, and this determines the throat-to-tube flow area ratio. However, details of the external shape of the leading edges of the fins and the projectile geometry at the nose-body joint govern the actual area profile in the throat region, defined here as the region between the projectile throat and the point where the fins first contact the tube wall. The effective flow area is nearly constant throughout this 2-cm long region of the nominal projectile configuration. Throat area ratio and aerodynamic efficiency have significant effects on both the starting Mach number and the static temperature of the propellant gas flowing through the throat region.

(c) Obturator Configuration

In early experiments the projectile carried within it an ignitor consisting of a pistol primer and a small charge (~0.5 g) of black powder.[3] An important modification which eliminated the

need for the internal charge was the development of an external ignition system.[13] The key element of this new ignition system is the obturator. To date, two types of obturator have been successfully used, both fabricated from polycarbonate (Lexan). The first type is an 8-mm thick solid disk of material having a mass of ~10 g. The second is a two-piece assembly with a combined mass of 15 g (Fig. 7). Its main body has a length-to-diameter ratio of 0.42 and is perforated axially with a series of 19 regularly spaced holes whose total cross-sectional area is approximately 40% that of the tube. A thin flat plate of the same material is used to seal these perforations against the driving gas (helium) in the light gas gun. This plate is snugly fitted into a shallow cavity machined in the back of the main body of the sabot.

5. RAM ACCELERATOR TEST SECTION INSTRUMENTATION

(a) Electromagnetic Sensors

The time-of-passage of the projectile at each instrument station is determined with an electromagnetic (EM) transducer that detects the magnets carried aboard the projectile.[29,30] The average velocity between transducers is calculated from these times and the distance between them, thus providing a velocity profile of the projectile throughout the test section.[26] These EM sensors consist of ~20 turns of 32 gauge copper coil wire wrapped around a solid polycarbonate core having an O.D. of 2 mm.[30] The sensing coil is inserted into a single-unit protective stainless steel casing that is designed to withstand the high pressure transients of the experiments. The typical output signal amplitude of the EM sensors is ~5 mV and its total time duration is ~15 μsec. Electromagnetic signals are amplified by a factor of 100 with amplifiers having a 2 MHz bandwidth and then added together through a summing amplifier.[30] The summed EM signals originate from sensors that are typically positioned 0.8 m to 2 m apart, which results in a minimum temporal separation of ~320 μsec for a projectile traveling at a velocity of ~2500 m/sec. During normal ram accelerator operation, this temporal separation has been found to be more than sufficient to readily distinguish the axial location of a particular signal from the string of EM signals. The outputs from all 43 EM transducers are fed to six data channels in this manner.

(b) Pressure Transducers

Pressure sensors are used to monitor the tube-wall pressure field that is generated by the passing projectile and the associated combustion activity. Early experiments were plagued with inadequate and unreliable pressure transducers. After five years of working with the supplier of the piezoelectric pressure transducers (PCB Piezotronics, Inc.), robust and reliable sensors have been developed that are providing high quality data on the ram accelerator pressure fields. The piezoelectric pressure transducers currently used in the experiment have model numbers

119M39/402M99, 119M44/402M99, and 119A/402M99. Their natural resonant frequencies are in the range of 450 to 500 kHz and their sensitivity varies from 9 to 18 mV/atm. These pressure transducers have a 6800 atm maximum operating pressure rating and a rise time of 1 μsec. The ability of the transducers to follow the transient behavior of the pressure waves about the projectile has made them invaluable in interpreting the gasdynamic phenomena generated by the projectile motion in the ram accelerator.

Pressure signals from various stations are routed through a multiplexer unit which isolates the individual signals and monitors each sensor during the time frame of projectile passage. The circuit shown in Fig. 8 is capable of multiplexing eight signal inputs to a single output. In the quiescent state Channel 1 is continuously monitored by a comparator. When the output from Channel 1 exceeds 100 mV, a timer is triggered and the channel continues to be monitored for approximately 1 msec. After this time, the multiplexer switches to monitor Channel 2, and the sequence continues in a similar manner through Channel 8. Multiplexed signals are DC coupled, and the bandwidth is approximately 10 MHz. The sensors on a multiplex string are typically situated at stations that are spatially separated by at least 3 m. This multiplexing configuration allows monitoring of up to five pressure transducers on a single DAS channel for projectile velocities up to 3000 m/sec.

(c) Fiber-Optic Luminosity Probes

Luminosity probes have been developed to monitor the light emissions from the combustion phenomena occurring in the vicinity of the projectile.[31] The fiber-optic cable consists of a 1-mm diameter polymethyl-methacrylate core surrounded by a fluorine polymer cladding and a black plastic jacket (1.5-mm O.D.). The fiber itself has a 56° angle of acceptance and is inserted into the probe as shown in Fig. 9. This two-piece luminosity probe consists of an outer housing manufactured from 4140 steel alloy and a brass back plug for holding the optical fiber. Each piece of the probe contains a 1.5 mm diameter hole through its center to accommodate the sheathed optical fiber. As the brass back plug is threaded into the outer housing its coned tip is forced into a coned seating surface having a slightly different angle. Consequently, the tip of the brass plug crimps the fiber-optic cable, creating a pressure seal around the fiber and on the coned surfaces. The outer housing is sized to fit inside the standardized instrument ports of the ram accelerator test section. This two-piece design for the luminosity probe was chosen for several reasons. Most importantly, the fiber can be recessed in the probe housing to reduce the effective acceptance angle of the unit. This results in more accurate spatial discrimination of the signal output. A second advantage of this probe design is that the fiber can be easily removed for maintenance and/or replacement.

The optical fiber guides the in-tube broad-band light emissions to a photodiode whose output is logarithmically amplified by the amplifier circuit shown in Fig. 10. Logarithmic amplification, as opposed to linear amplification, permits the examination of low intensity luminosity associated with shock waves and the high intensity luminosity resulting from combustion, without exceeding the voltage limits of the data acquisition system (discussed in next subsection). The output end of the optical fiber is manually aligned with the photodiode to maximize light sensitivity. The resulting signals are multiplexed in a manner similar to the pressure signals. Qualitative comparison of the outputs from different stations is based on the relative intensity levels of the luminosity data in the vicinity the projectile. The correlation of the luminosity data with the EM and pressure signals has provided significant information on the combustion phenomena that occur during ram accelerator operation.

(d) Data Acquisition System

Data from the experiment are collected and stored with a LeCroy data acquisition system (DAS) and are processed on an IBM-compatible 386 type micro-computer using the LeCroy Wave-Form Catalyst software. Major components of the DAS are two LeCroy CAMAC crates (Model #1434), five Quad 10-bit transient digitizing modules (Model #8210) with ten memory modules (Model #8800A), three Quad 12-bit transient digitizing modules (Model #6210), and two CAMAC to GPIB interfaces (Model #8910A). The eight digitizing modules (five 10-bit and three 12-bit) provide 32 data channels with a minimum memory time window of 16 msec at a sampling rate of 1 MHz. Maximum amplitude range for data storage is ±5 volts with a digitization level of 10 mV. Triggering of the DAS can be accomplished with the output signals from any of the sensors located along the ram accelerator test section.

6. INSTRUMENTATION UNDER DEVELOPMENT

(a) Microsecond Response Thermocouple

A design for a thermocouple having a response time on the order of microseconds has been developed and prototypes have been built and tested.[32] The basic requirements for a thin-film thermocouple system are to have a junction of two dissimilar metals exposed to a temperature change and a method of reading the resulting output voltage. The main focus of this design was to have a simple, inexpensive way to manufacture rugged thermocouples that could, for a period of time, survive their environment. The design reported on here is a variation to the one built in Germany during WW II by Bendersky,[33] and later suggested by Hall and Hertzberg.[34]

The temperature range of interest suggests the use of steel and nickel as the two dissimilar metals to form the measuring junction. Nickel was chosen for its high temperature durability and the steel-nickel combination was needed due to its capability of measuring the extreme temperatures experienced in the ram accelerator. The thermocouple, shown in Fig. 11, consists of 4340 steel alloy with a thin, 5 to 15 μm thick layer of nickel deposited on its face, which is the plane at which the thermal electromotive force (EMF) is generated. The lead wire to the nickel plating is 0.635 mm diameter nickel wire coated with Teflon, which was chosen as an insulator due to its excellent resistance to both mechanical shock and moisture.[35] This nickel wire is fed down the center of the hollow steel plug. The top of the plug is bored out as large as possible (for strength reasons it has to retain a minimum wall thickness of 2.5 mm) to aid in filling the plug with Devcon 2-ton clear epoxy and to help decrease the likelihood of a short circuit, which is possible if a segment of exposed nickel lead wire comes in contact with the steel casing. The bore of the casing is stepped down until the final aperture is slightly larger than that of the coated nickel wire, thus minimizing the gap between this wire and the casing that has to be bridged by the nickel plating laid on top of the probe face.

The epoxy is inserted into the top of the probe using a medical syringe, after which the syringe plunger is removed and the coated nickel wire is fed down through the needle into the probe and out through the face. This procedure centers the wire in the probe and helps prevent the Teflon coating from being removed as the wire is installed. A short length of wire (3 to 5 cm) is left exposed at the top of the probe body and about 1 mm of nickel wire is left extending beyond the probe face after the hardening of the epoxy. The face of the probe is sanded down using 250, 400 and 600 grit wet/dry sandpaper until the face is flat and smooth. The probe face is then coated with a 5 to 15 μm thick layer of nickel using an electroless nickel deposition technique. This process was chosen because there are no outgassing restraints placed on the surface being coated. Electroplating was considered but Teflon and epoxy are both exposed on the probe face and since neither material can carry an electrical current, this technique for forming the thermocouple junction was eliminated as an option.

Shown in Figure 12 is a schematic of the entire thermocouple. A 4/40 screw in the top of the plug attaches the lead wire connection for the steel body. Both the nickel and steel lead wires were made as short as possible due to the high magnetostriciton of the nickel wire, which generates unwanted voltage when vibrated. Both lead wires are soldered to a BNC connector and the output from these probes is run through a 10 gain amplifier. A reference junction was deemed unnecessary for ram accelerator application due to the high temperatures being measured. (The need for such a reference junction is usually found when measuring temperatures near room temperature.)

There is very little maintenance needed for these thermocouples once they are assembled. Each probe is removed after each shot (before swabbing the test section) and, using a propanol soaked cotton swab, the face is cleaned until all of the sooty deposit is removed. After the test section has been swabbed the probes are reinstalled. The benefit of this type of thermocouple probe is that not only is it inexpensive and easy to manufacture, but after the nickel plating on the probe face has eroded, the probe can be easily refurbished. Using a fine grit sandpaper to remove the original nickel plating, the probe need only be replated. An easy way to determine if all the original nickel plating has been removed from the face of the probe is to apply a small amount of copper sulfate to the face using a cotton swab. If the nickel is entirely removed, the steel will react with the solution to create a copper finish, which needs only to be sanded off before replating.

The method of calibration used produces some experimental error. Due to the high temperatures involved, any calibration table which could be extrapolated to temperatures near those predicted by Chapman-Jouguet detonation theory for our typical gas mixtures was deemed acceptable, with the prospect for refinement in the future. By inspecting a typical plot of a calibration table,[33] as shown in Fig. 13, it can be seen that the plot of voltage versus temperature is linear for the temperature range anticipated in the ram accelerator.

The reacting gas environment, which the measuring junction is exposed to during a shot, tarnishes the nickel plating on the probe face, causing prior calibration plots to be incorrect and thus making the re-calibration of these probes necessary after every shot. This need required an efficient and rapid calibration technique. It was decided that four temperature points between 100°C and 200°C would, within an acceptable error margin, reproduce this near-linear curve to calibrate temperatures found in the ram accelerator environment. These values are found using a procedure, which is referred to as the stirred liquid bath method, that was suggested in Reference 35. By heating a container of vegetable fat on an electric burner, temperatures in excess of 200°C are easily obtained (water and automotive oils either boiled or burned at the high calibration temperatures). A reference thermometer, placed directly in the bath, is used to measure the bath temperature and to stir the liquid bath to ensure an accurate temperature measurement and a uniform bath temperature. The face and shaft of the thermocouple are then placed in a borosilicate glass protection casing and immersed in the liquid bath at varying temperatures. An oscilloscope is used to record the voltage output and the experimental set-up as described is shown in Fig. 14. By recording the voltage output corresponding to the known temperature, calibration plots similar to that shown in Fig. 13 are generated. The actual time history of the gas temperature at the tube-wall can then be found by using this plot and the voltage output of the calibrated thermocouple.

(b) Spectroscopic Apparatus

Identifying the concentration levels of the chemical species within the flow field of a ram accelerator projectile will help further the understanding of the combustion processes involved in the various propulsive modes. Detection of metal oxides would indicate that the projectile itself is being consumed during the acceleration process and that the corresponding chemical reactions should be included when modeling the combustion process. Highly resolved, time-accurate species concentration data would enable the determination of where the propellant ignition is occurring as a function of in-tube Mach number and be very useful for validating CFD codes for reactive flow fields. In preliminary efforts to acquire these data, we have applied spectroscopic techniques to analyze the luminosity output of the optical fiber probes.

The light emitted during a firing of the ram accelerator was collected by a flush-mounted fiber-optic cable. The fiber guided the light to the slit entrance of a spectrograph (Boller & Chievens Cassegrain Spectrograph built by Perkin-Elmer in 1980) which was equipped with a charge coupled device (CCD) camera.[36] The spectrograph has interchangeable and tiltable grating assemblies to allow a selection of wavelength coverage. The camera shutter is open for the duration of the shot (approximately 4 msec). The light gathered by the camera is therefore time-integrated. The data are then read out, reduced and analyzed.

A fiber-optic light guide with a pure silica core was chosen for its low attenuation over the spectral range of 400 to 1100 nm (Table 1). The fiber length was approximately one meter and its cladding was a hard polymer that was covered with a black sleeve to prevent damage. The fiber was mounted in a steel plug with epoxy, as shown in Fig. 15. A heat-cured epoxy, which was

Table 1: Fiber-Optic Light Guide Specifications

Specifications	Spectrometer Probe Fiber	Luminosity Probe Fiber
Core material	Pure silica	Polymethyl-methacrylate
Core diameter	1.0 mm	1.0 mm
Outer diameter	1.4 mm	2.2 mm
Maximum attenuation	14 dB/km at 820 nm	160-250 dB/km at 660 nm
Numerical aperture (NA)	0.37	0.47

resistant to solvents, was chosen for the harsh environment it was exposed to in the ram accelerator tube. About 5 cm of the fiber cladding was removed to provide good adhesion. The inside of the plug was cleaned with a flux remover for the same purpose. After curing was complete, the end of the fiber was cleaved and polished to provide maximum light transmittance.

The spectrograph was made to be used at the f/13.5 Cassegrain focus of a telescope and is essentially light-tight when mounted in this fashion. The spectrograph is positioned 10 m from the entrance to the ram accelerator test section and a schematic of the optical system is shown in Fig. 16. The available adjustments are slit width, collimator focus, and grating angle. It is also equipped with a comparison He-Ne lamp. The focal length is 69 cm, the slit height is 2.5 cm, and the slit width was set to 0.016 cm. The spectrograph was originally designed for plate photography, but has been adapted for use with a CCD camera. The grating was blazed for 500 nm with a dispersion of 9.01 nm/mm (experimental) and was meant to be used in the first order blue. This grating has a ruled area 64 mm x 64 mm with 60 grooves/mm. An additional grating was mounted for this experiment. It had a blaze angle of 11°6' with 500 grooves/mm. These parameters correspond to best efficiency at 770 nm and the dispersion was determined to be 10.7 nm/mm.

Coupling a fiber to a spectrometer is not the best way to analyze low-intensity emission, due to the very low efficiency of a fiber-fed spectrometer. However, during the acceleration of a ram accelerator projectile, there is enough light radiated by the combustion that a usable signal reaches the silicon detector or CCD array. The limiting factor of an optical system is called the "etendue."[37] Any light that does not fall within this limit is lost. The etendue of a spectrometer is the product of the entrance slit area and the accepting/transmitting solid angle. The solid angle is $\Omega = 2\phi/66°$, where one steradian (sr) subtends approximately 66° and the half angle is $\phi = \arctan(a/2f)$, where a is the aperture and f is the focal length. Although the spectrometer was designed for a f/13.5 telescope, the collimator diameter is a little larger in order to catch all the light from the long slit. Even though this experiment does not use the whole slit height (h), the smaller effective focal ratio (f/#) matches the fiber numerical aperture (NA) better, thereby increasing throughput. Thus, for a 7.5 cm aperture, the focal ratio is effectively 9.2. For a Cassegrain spectrograph having a slit width of w = 0.016 cm:

$$\text{etendue} = h \times w \times \Omega = (2.5)(0.016)(.0943) = 3.77 \times 10^{-3} \text{ cm}^2\text{-sr.} \qquad (3.1)$$

The etendue of the fiber is the product of the core area and the accepting/transmitting solid angle. For fibers, the half angle is $\delta = \arcsin(\text{NA})$. The etendue of the plastic optical fiber used in the broadband luminosity probes is $9.020 \times 10^{-5} \text{ cm}^2\text{-sr}$.

The total useful light coupled to the spectrometer can be calculated using the area ratio of overlap:[37]

$$A_s / A_f = [\, 2 \, (f/\#) \, \tan \, (\arcsin \, (NA))]^{-2} \qquad\qquad (3.2)$$

The NA to focal ratio mismatch couples approximately 1.9% of the light. The percentage of the image that is not obstructed by the slit is given by the product of the fiber diameter and the width of the slit divided by the fiber core area (20.4%). Thus, the total useful light coupled to the spectrometer is 0.4%. In addition, for each reflective surface, there is a 4% loss, so the light losses within the spectrometer due to the collimator and the grating further reduce the throughput to 0.36%. Using a pure silica fiber-optic light guide increases the throughput by a factor of two. Silica fibers not only have a smaller NA but they also transmit a wider range of wavelengths (250 to 1200 nm), and therefore were selected to guide the in-tube radiation to the spectrometer.

A sophisticated data acquisition system with a two-dimensional CCD array was used. The CCD camera was cryogenically cooled with liquid nitrogen to virtually eliminate dark current, or optical noise caused by thermal excitations. The CCD has excellent quantum efficiency for the range 300 to 1100 nm. The high resolution array has 1024 x 1024 elements with each pixel 15 μm on a side. Since the image height was approximately 300 μm, the image spanned 20 rows of the array. The rows were added on the chip (this is called binning) in order to increase the signal-to-noise ratio (S/N) by decreasing the amplifier noise added to the data during readout. The amplifier on readout induces approximately ten electrons of noise on the data. Surprisingly, in the first spectral data set taken in the near infrared (NIR) region, the CCD was saturated by light, so thereafter binning was adjusted for data gathered in that spectral region. Figure 17a shows how the CCD is illuminated by the fiber-guided radiation during a shot and Fig. 17b shows the unreduced data of the peak row. The camera shutter was manually triggered before and after each shot, so the spectrum is time-integrated.

The data were calibrated by taking into account the background noise, spectral irradiance of the calibration lamp, and the throughput of the system. Figure 18a displays the response function for the spectral region 650 to 790 nm with the grating having the best efficiency at 770 nm. The response function of the system, which includes the fiber, spectrometer, and CCD, is obtained by directing the calibration lamp into the opposing port of the spectrometer probe. These data are preferably taken about two hours before the ram accelerator shot, however, experimental schedules are often unpredictable and several days may elapse between the calibration readings and the shot data.

Calibrations are also taken with several different bandpass filters which allows accurate determination of wavelength and grating dispersion. After the response function and wavelength calibrations are obtained, the ram accelerator tube is sealed, pressure-checked, and evacuated. About ten minutes before the shot, when the room is dark, a background reading or bias is taken. The bias contains all of the electrical offsets and is subtracted from all exposures when the data are reduced. The response function of the system was calibrated using a quartz tungsten halogen (QTH) lamp. This source has a blackbody temperature of 3063 K. The flat field is obtained by dividing the response function by the normalized input function and it is then used to correct the shot data, resulting in Fig. 18b. The y-axis of the data is in counts and each count is equal to six electrons or photons detected at the CCD.

Broadband filters were placed in front of some of the sensors during the spectroscopic investigations in order to obtain complementary data. Several broadband filters were used. Their spectral ranges were calibrated with a spectrophotometer. First, a background scan was taken and then each filter was placed between the slit and the calibration source. The blue filter at full width half maximum (FWHM) had a bandpass of 440±6 to 500±9 nm. The red filter at FWHM had a bandpass of 575±12 to 725±22 nm. The infrared filter was characterized by a bandpass of 735±22 to 1000 nm.

(c) Imaging of Flow Fields From Fiber-Optic Arrays

One of the goals of the ram accelerator research program was the acquisition of images of the ram accelerator projectile and the adjacent (luminous) flow field in the test section. Such images would aid the understanding of combustion and flow dynamics involved in the various acceleration modes of the device. Although limits on resources prevented the construction of an imager for this purpose, a significant effort was expended to design such an imager, and this section summarizes the progress made.

The goal of this exercise was to acquire an image of the projectile in a 30-50 cm section of the 38-mm diameter tube with a spatial resolution of ~1 mm. A straight-forward approach would be the placement of a 30-50 cm transparent section in the tube so that the entire field could be recorded in a single frame with a high-speed framing camera or a CCD device. Previous experiments and computations have demonstrated that it is difficult, at high fill pressure (>20 atm), to operate with a 30-50 cm long transparent section in the test section because of strength limitations of the transparent materials of interest. However, a practical technique for using a transparent section (made from Lexan) about 1 cm long has been demonstrated that can safely operate at the maximum fill pressure of the test section. Thus, the available imaging

20

techniques are restricted to smear cameras or high frame rate cameras which will record successive images of the transparent section to build up a picture encompassing 30-50 cm of the flow. Because of the high cost of commercial smear cameras and the limited information obtainable from their images, the use of a high frame rate camera was pursued.

The required frame rate for the imager depends on whether a 1-D (line scan) or a 2-D (area) image is captured. To achieve a 1 mm resolution, a line scan camera (40x1 pixels) would require a frame rate of at least 2 MHz for a projectile speed of 2 km/sec. An area camera (40x10 pixels) would require a frame rate of 200 kHz, and a 0.5 μsec exposure. No affordable commercial line-scan or area cameras (CCD devices) were found that are capable of this frame- or line-rate. However, we have been able to design a relatively simple and inexpensive line-scan device which can easily reach the desired scan rates. Therefore, a project was undertaken to develop a fast line imager using discrete photodiodes.

Previously, a system using a photodiode to record luminescence from the in-flight projectile and propellant gas had been developed as a diagnostic. This technique is now routinely used to obtain light signatures at several stations in the tube. Although not designed to provide an image, this system is well suited to serve as an element of a line imager because of its fast time response and wide dynamic range. The latter is due to the use of logarithmic amplification of the photodiode signal, as illustrated in the electrical schematic of Fig. 10. Logarithmic amplification results from the use of a low-capacitance diode as the feedback element of a transimpedance network, which uses a fast (15 nsec rise time) amplifier with a voltage gain G = 25, built of discrete components. The small-signal time constant of the logarithmic amplifier is approximately given by $\tau = (C_d+C_i)^* \times R_d/G$, where C_i is the photodiode capacitance, C_d is the feedback diode capacitance, and $R_d = V_d^*/I_b$ is the resistance of the feedback diode with a forward bias current I_b (V_d^* = .05 V). With a bias of 1 μamp (set by resistance R_1), and with C_d+C_i = 20 pF, τ = 40 nsec (rise time of about 120 nsec). The NEP is set by Shot noise of the bias current in the feedback diode and is roughly 5 nW. The dynamic range is about 10^5.

An array of 40 photodiodes, each with its own logarithmic amplifier, would serve as a line imager. For maximum flexibility (and to allow easy expansion to more than 40 pixels) an image of the projectile is formed by a lens on one end of a linear array of fiber optics, with one fiber per photodiode, as illustrated in Fig. 19. Each fiber thus transfers light for one pixel to the corresponding photodiode, and the photodiodes need not have any prescribed geometrical arrangement.

In order to build an area image of the projectile, successive line images must be recorded and stored at intervals of about 0.5 µsec. This is accomplished using an analog-to-digital converter (ADC), which converts the analog voltage from an amplifier to a digital signal and stores this signal to static random access memory (SRAM). Given the logarithmic output from the photodiode units, an 8-bit converter is sufficient for imaging the projectile.

To minimize the number of components and the complexity, the analog signals are multiplexed either 4:1 or 8:1, so that only 10 or 5 ADC/SRAM modules are needed (instead of 40). Each ADC/SRAM unit is identical and all are clocked in parallel. Inexpensive "flash" ADC and SRAM chips are available that will allow data acquisition at rates of 30 megasamples per second (MSPS) for each ADC/RAM module. The data acquisition cycle is repeated at a line rate of 2 MHz to build up a digital image in RAM. Five hundred cycles are needed to image a 50-cm length at a resolution of 1 mm, so that either 2 kB or 4 kB of SRAM memory is needed on each module, depending on multiplexing. An 8 kB, 25-35 nsec SRAM is certainly adequate for any anticipated line-image rate. The digital image (roughly 20 kB) can be read into computer memory at a modest rate after the experimental run, for visualization and enhancement. The time multiplexing of 4 or 8 signals in each unit results in a slightly skewed image, but the skewing is comparable to image smear from imaging onto a fiber, and in any event this effect can be eliminated by simple image processing once the data have been recorded.

This approach is very flexible in that additional linear pixels can easily be added for improved diametrical resolution. This expansion capability is not possible using a monolithic detector array. With small modifications the circuit approach discussed above is capable of pixel rates of 5 MHz, to allow < 0.4 mm resolution in the direction of projectile travel. In addition, the detectors and electronics can be situated a considerable distance from the driver tube, for safety reasons and to minimize microphonics. A color image is possible by using additional fibers and interleaved color masking. This imaging scheme is also applicable to shadowgraph images of the flow.

22

LIGHT GAS GUN   RAM ACCELERATOR TEST SECTION   DECELERATOR SECTION

DRIVER   LAUNCH TUBE   He DUMP TANK   INSTRUMENT PORTS   FINAL DUMP TANK   CATCHER TUBE

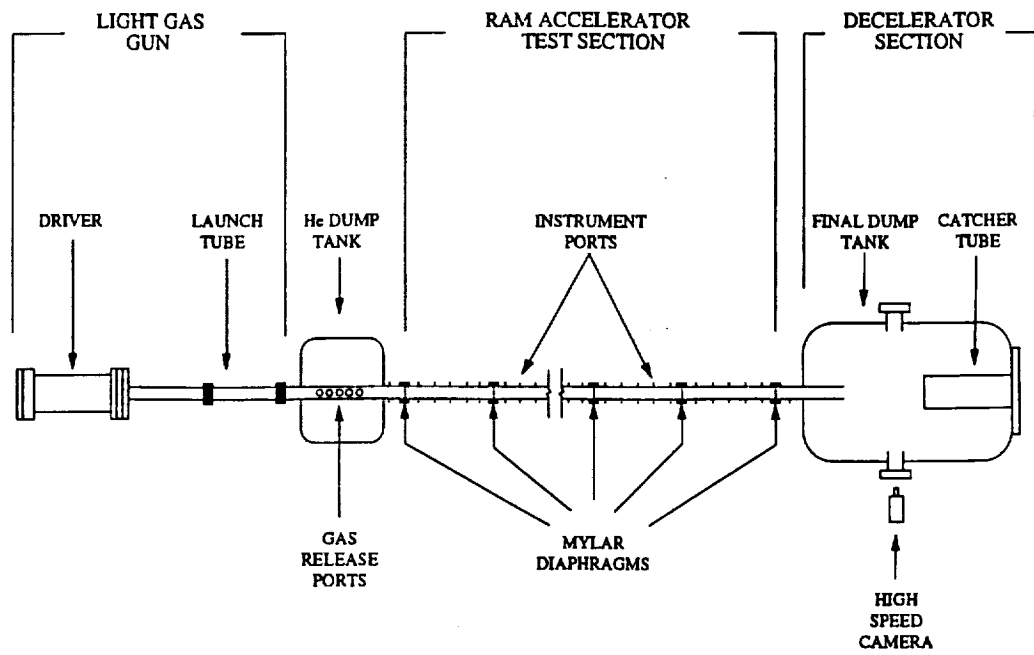GAS RELEASE PORTS   MYLAR DIAPHRAGMS   HIGH SPEED CAMERA

Fig. 5   Schematic of ram accelerator facility.
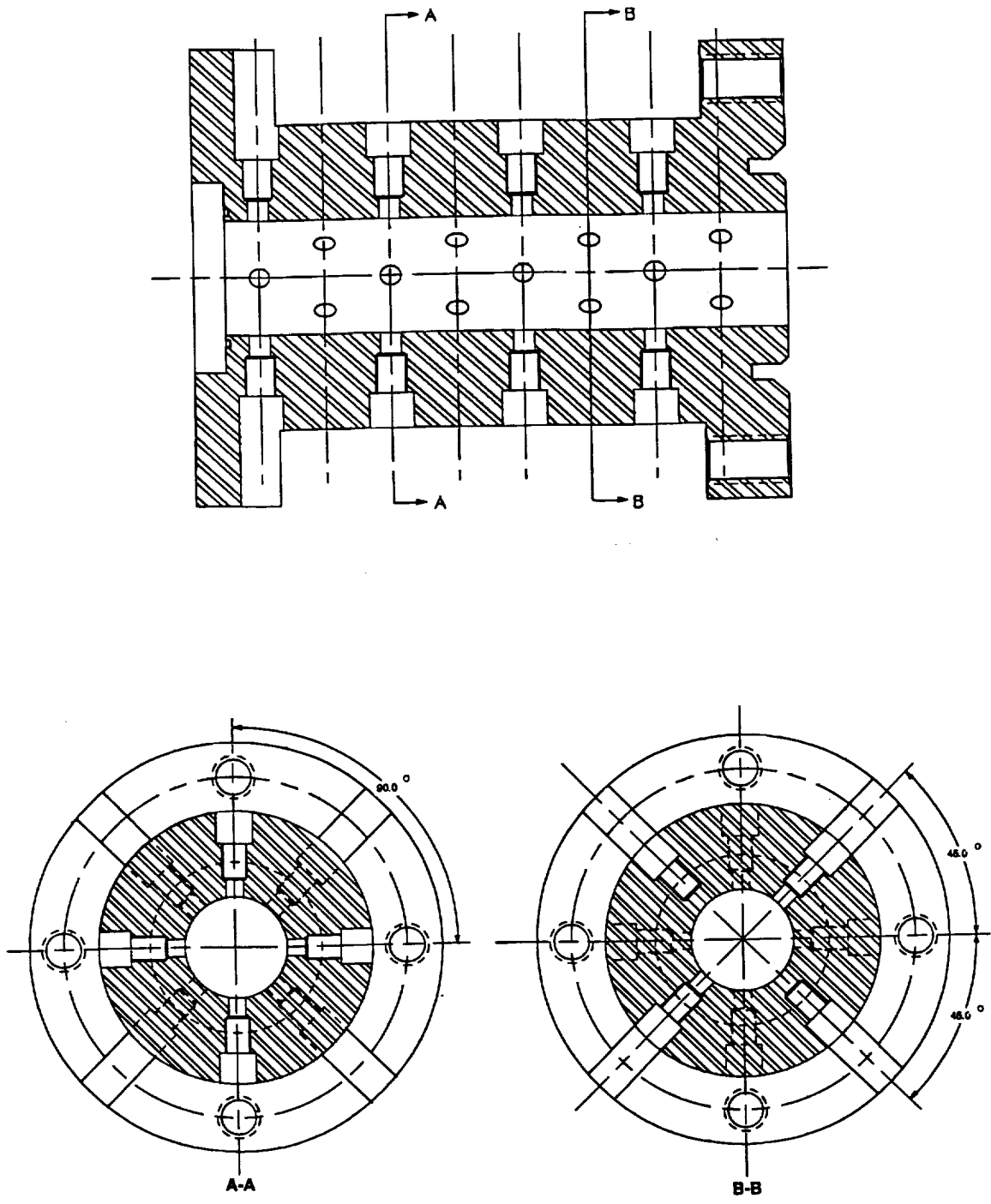
Fig. 6   Highly instrumented tube section.
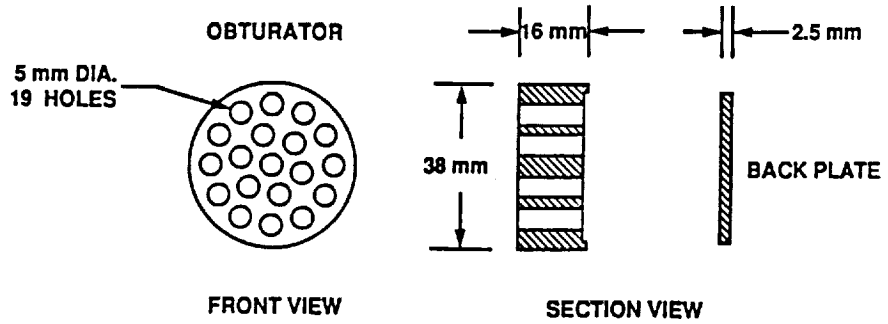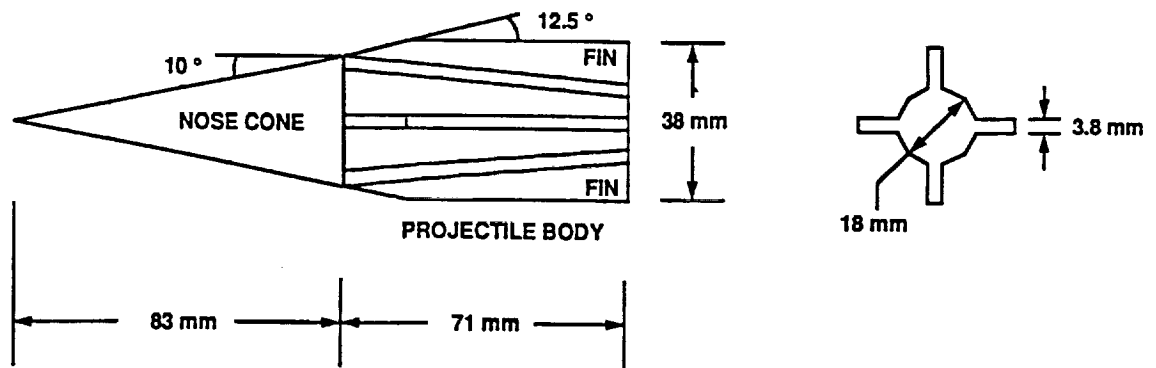
Fig. 7 Experimental projectile and obturator.

Fig. 8   Circuit diagram of multiplexer for pressure signals.
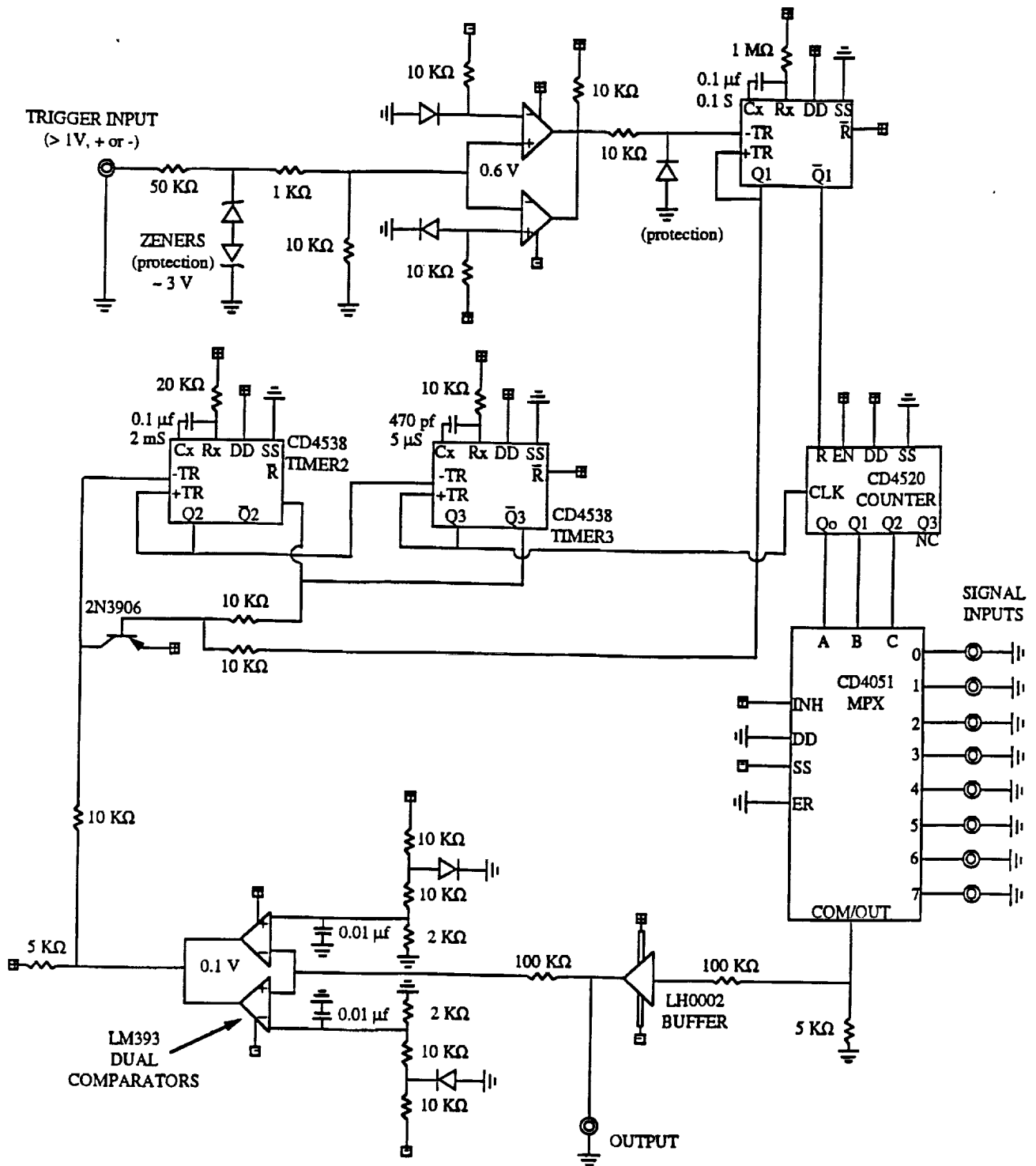
NOTE: All diodes are 1N4148 unless otherwise noted.
         Power supply leads on all IC's must be decoupled by 0.1 μf capacitors (not shown).
         All signal inputs are connected to ground by 10 KΩ resistor (not shown).
         + and - refers to +12 V and -12 V.

26

FIBER-OPTIC CABLE

FIBER HOLDER PLUG

(BRASS)

PRESSURE SEALS

FIBER GUIDE HOUSING

(STEEL)

LIGHT CHANNEL
(1.5 mm DIA.)

6 mm
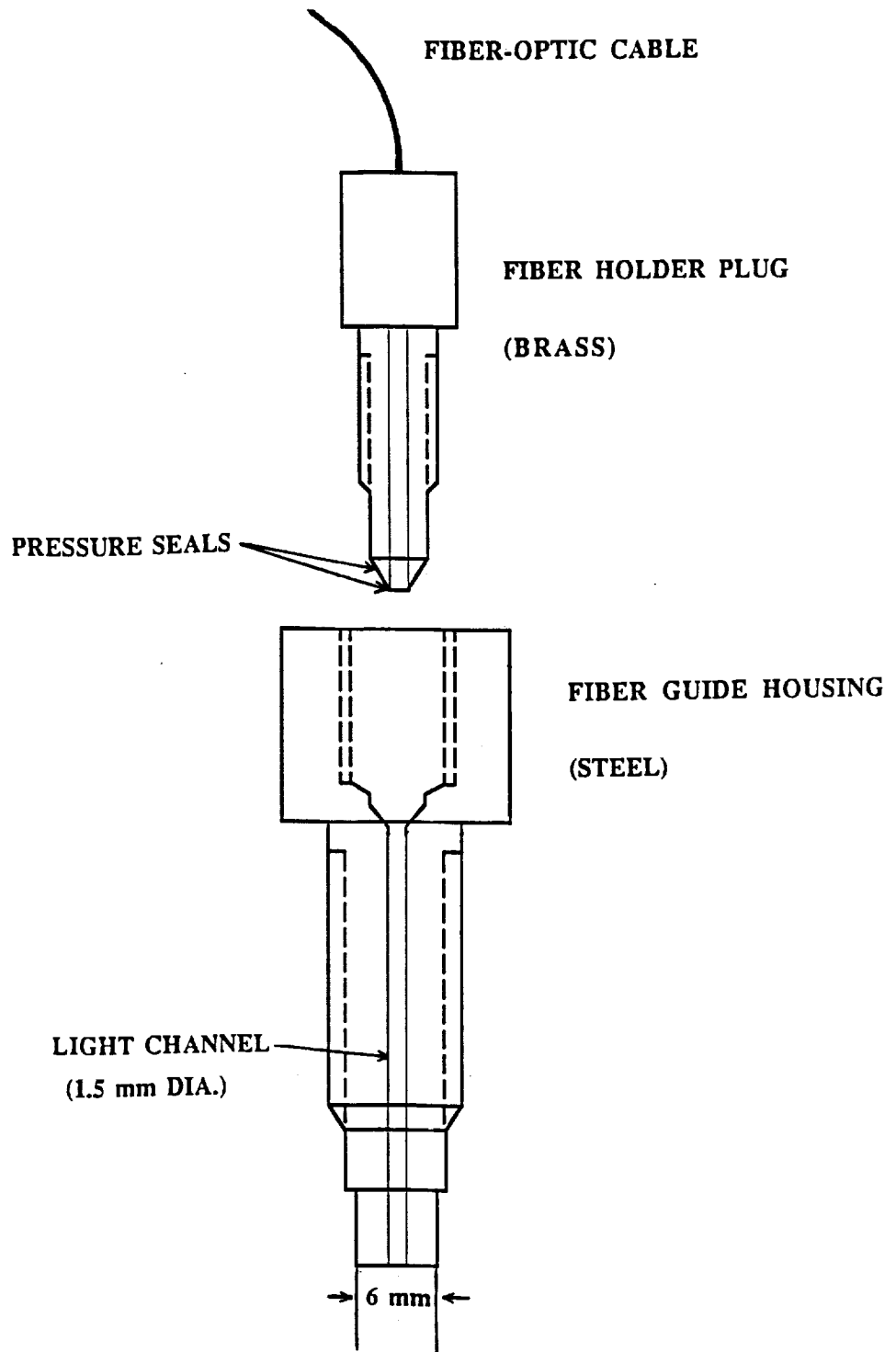
Fig. 9   Schematic of fiber-optic luminosity probe.

27

PHOTODIODE
Psig

Isig

1 MΩ

TRANSIMPEDANCE AMP
GAIN = 25
TRANSISTORS ARE 2N3906

10 KΩ

-6 V

100 KΩ   2.6 KΩ

FEEDBACK DIODE
LN 4148

1 KΩ

33 μf

10 KΩ   510 KΩ

LF357

-12 V   100 KΩ   +12 V   10 KΩ

CURRENT BOOSTER
GAIN = 20

LH0002

OUTPUT
Vout

RESPONSE: Vout (volts) ~ ln[1 + 1/2 Isig(μA)]
PHOTODIODE: Isig(μA) ~ 0.5Psig(μW)
BANDWIDTH: 1 Hz to 1 MHz
NOISE: Vout(noise) ~ 1 MV (rms)
DYNAMIC RANGE: 10-8 W < Psig < 10-2 W (S/N > 1)
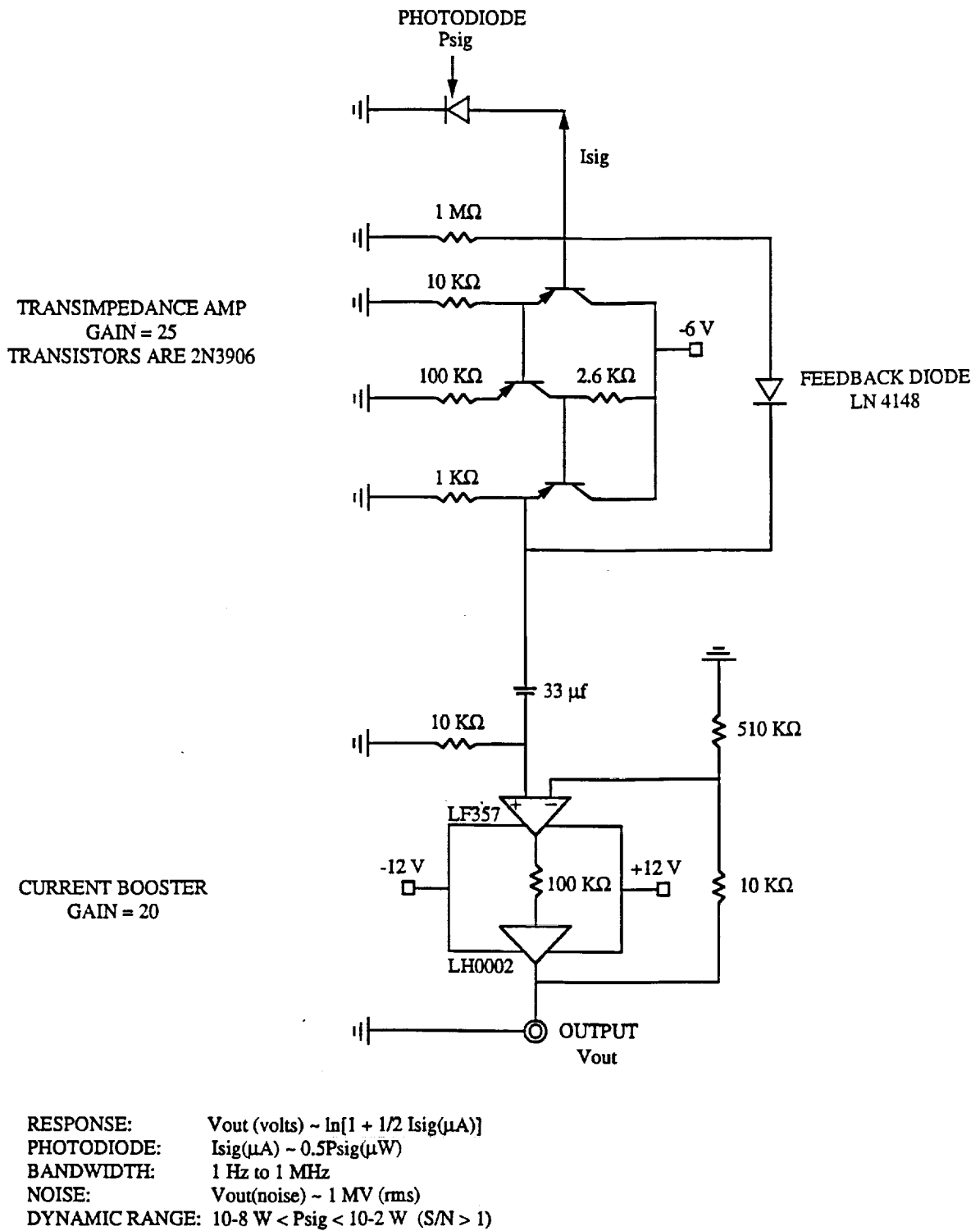
Fig. 10   Circuit diagram for logarithmic amplifier for PIN diode output.

28

STEEL CASING

THREADS

SIDE VIEW   FACE VIEW
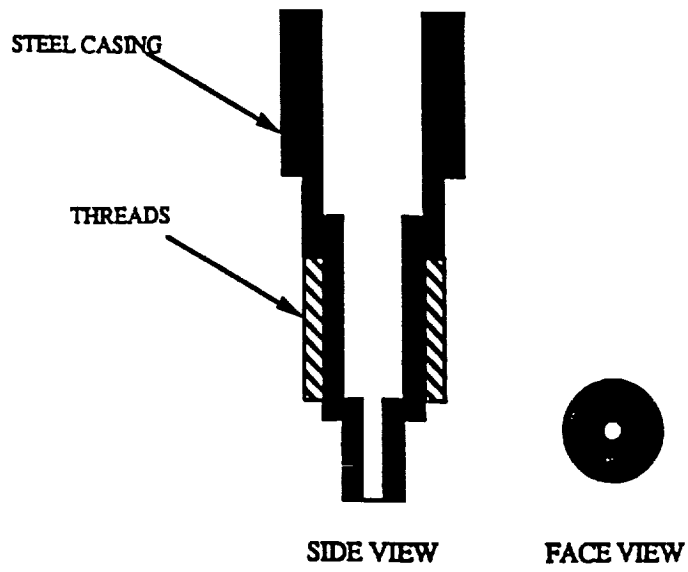
Fig. 11   Schematic of thermocouple probe casing.

BNC CONNECTOR

STEEL LEAD
WIRE

NICKEL LEAD
WIRE

NICKEL FILM
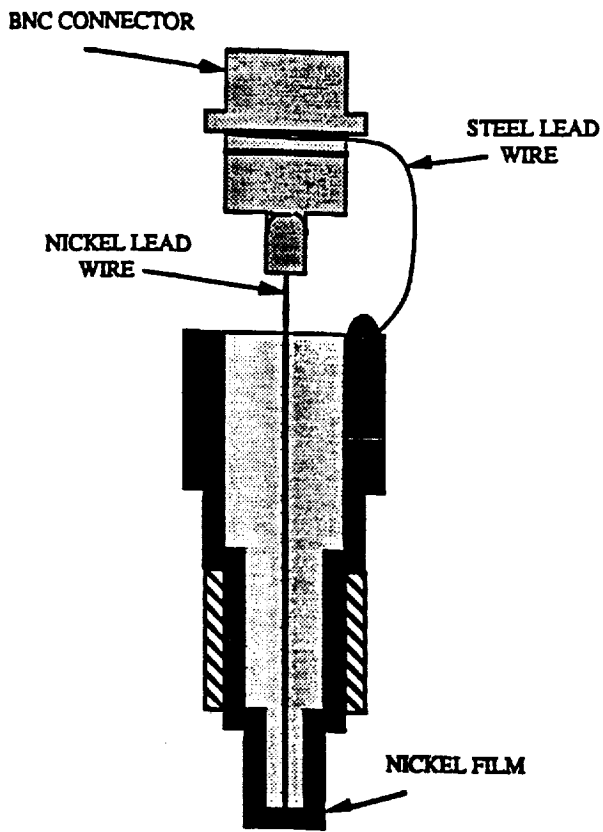
Fig. 12   Schematic of complete thermocouple probe assembly.
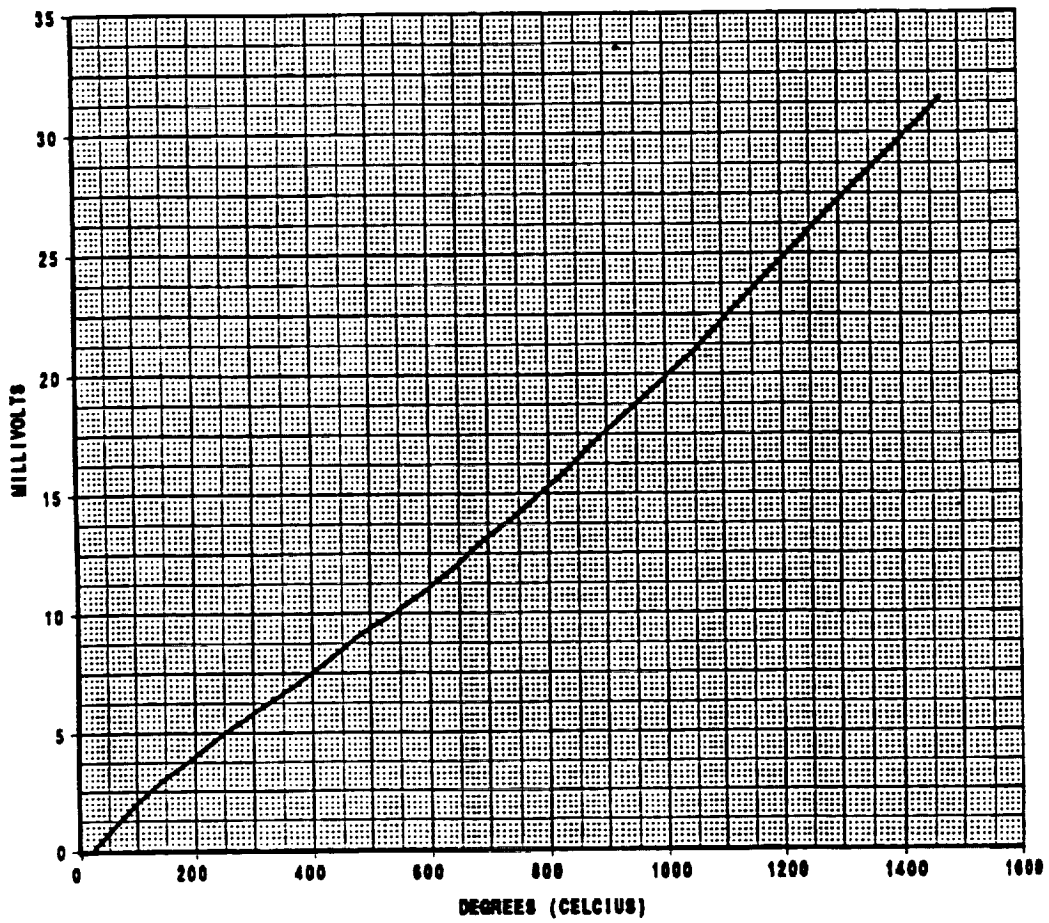
Fig. 13 Representative calibration curve for nickel-steel thermocouple.
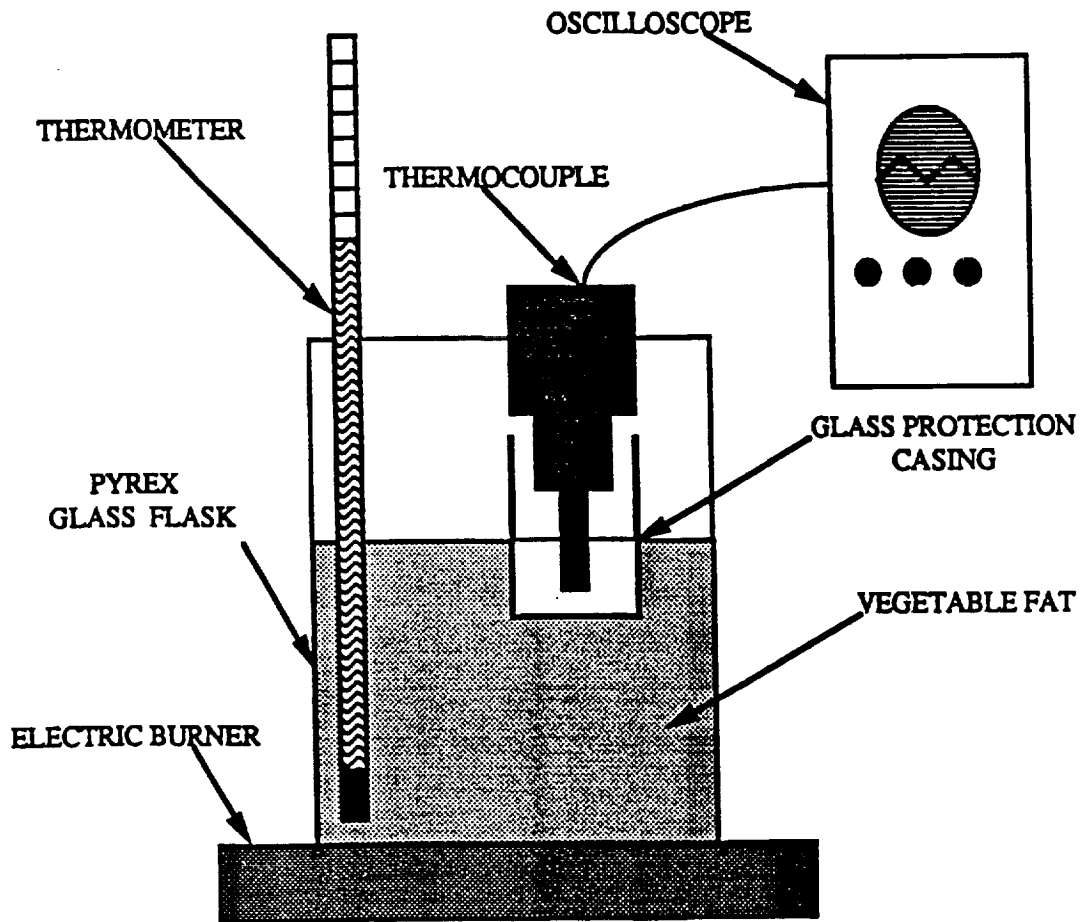
Fig. 14   Schematic of thermocouple calibration apparatus.

Fiber Optic Light Guide

Epoxy

Threaded Steel Plug
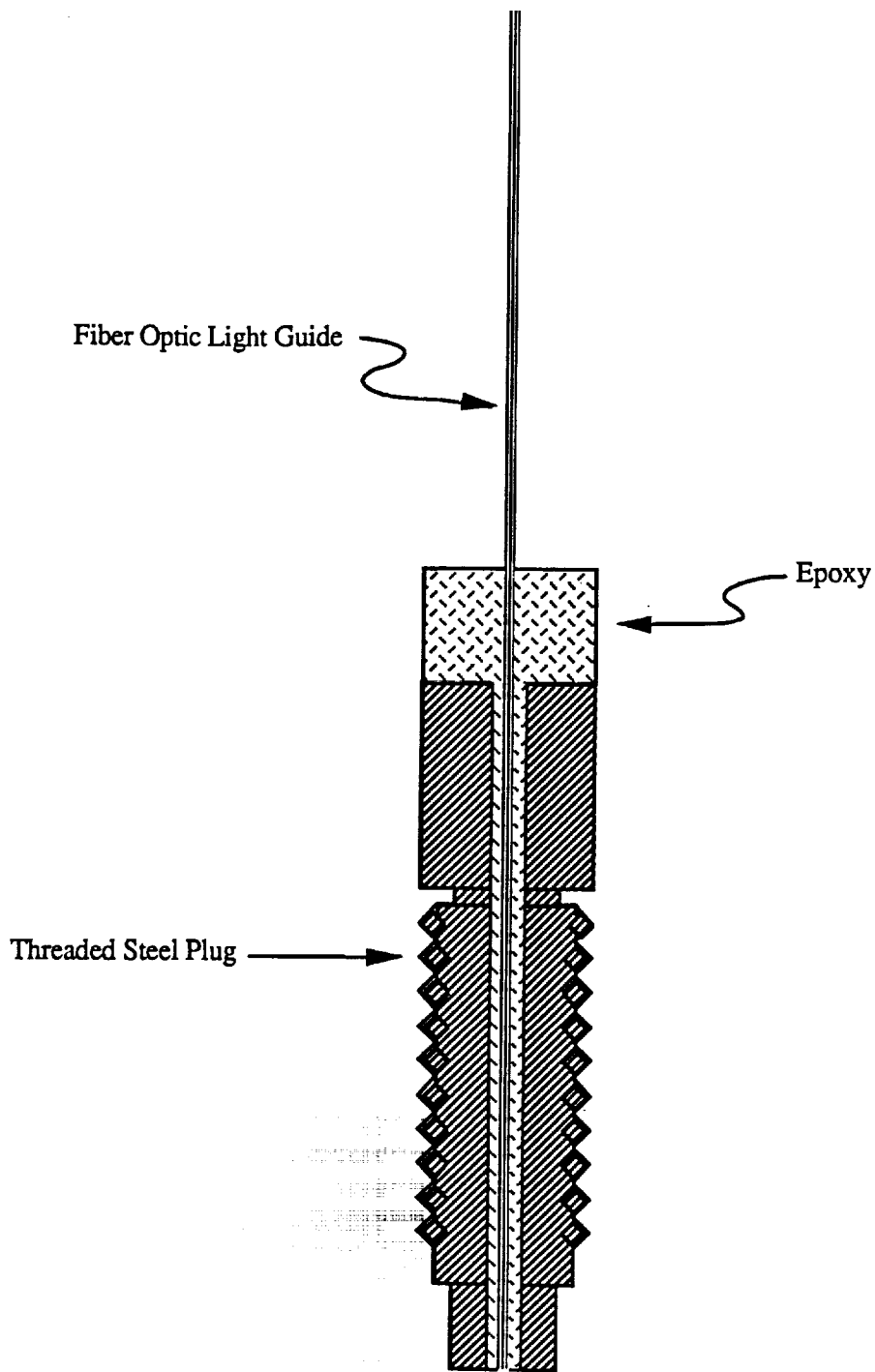
Fig. 15   Schematic of optical probe for spectroscopy.

Fiber Optic Guide

Ram Accelerator
Tube

Slit

Grating

Shutter

Image Focal Plane

CCD camera

Liquid
Nitrogen

Collimating Mirror
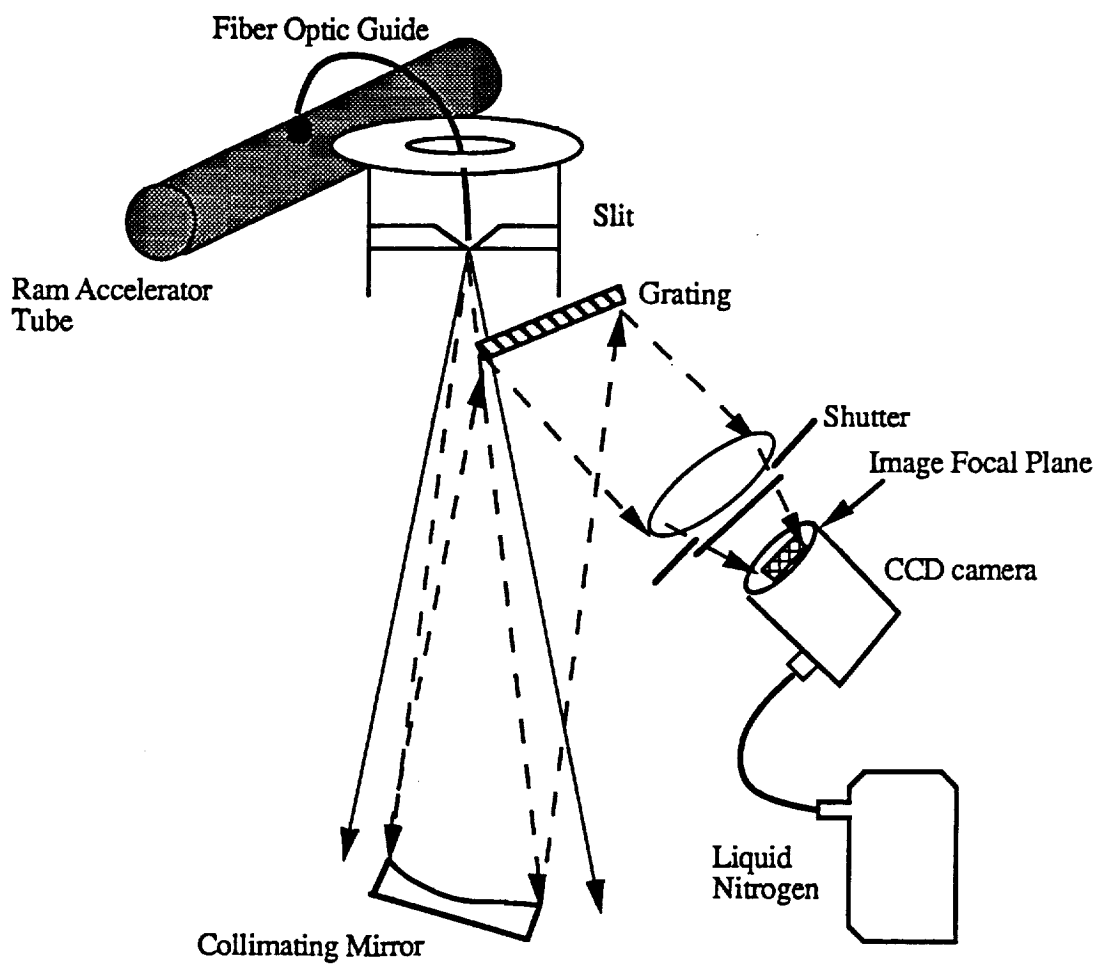
Fig. 16   Configuration of optical system for spectroscopy.
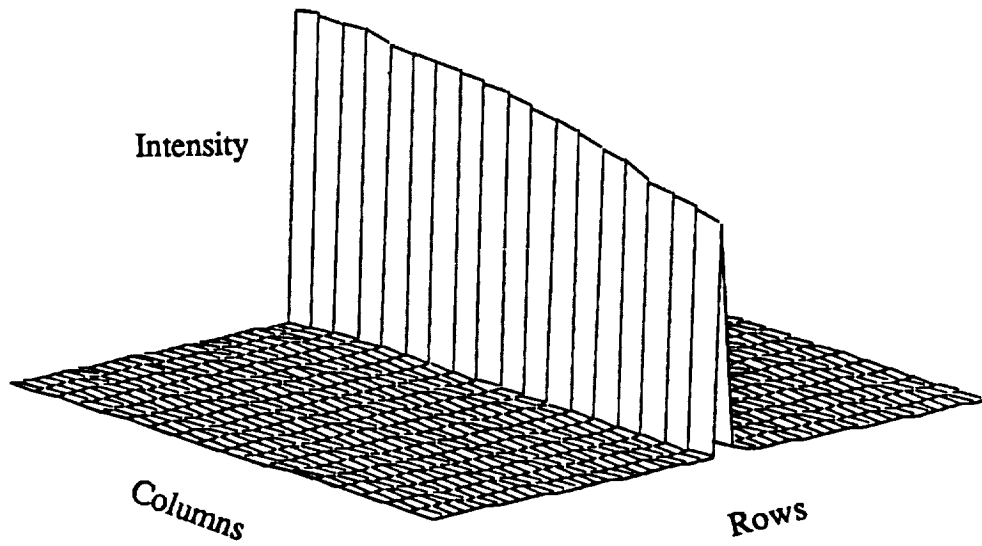
Fig. 17a   CCD illumination during experiment for data set 3.
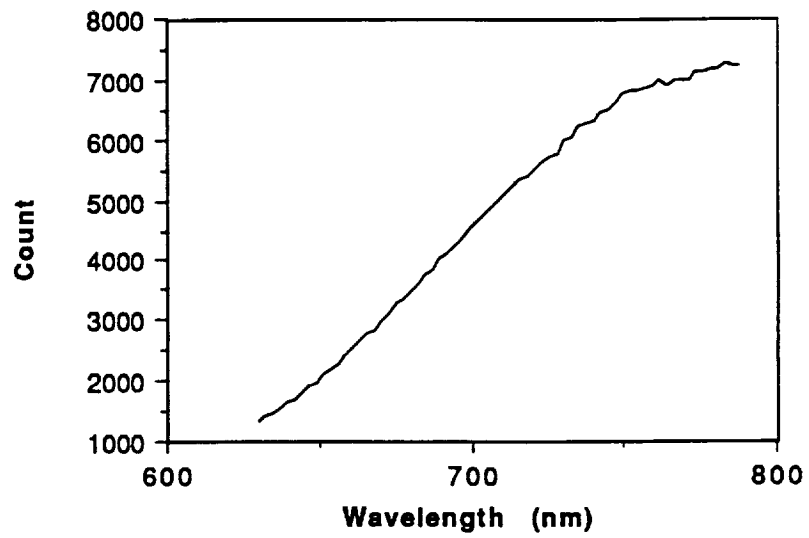
Fig. 17b   Unreduced peak row data for data set 3.
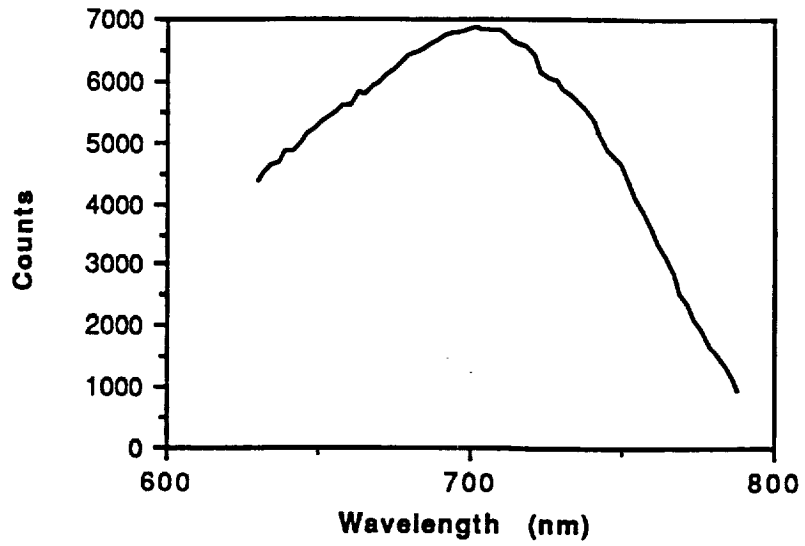
Fig. 18a   Response function for data set 3 using grating having peak efficiency at 770 nm.
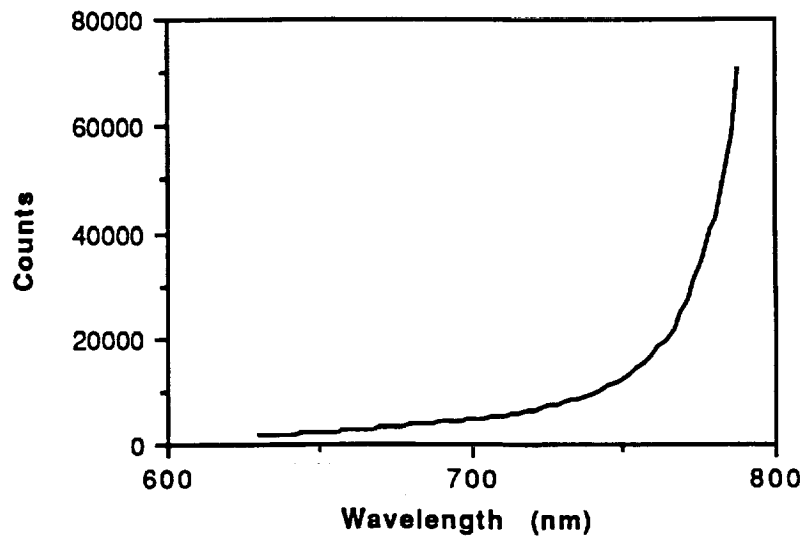
Fig. 18b   Results of reducing data set 3.

DETECTOR/PREAMPS
(1 PER FIBER)

8-BIT BUS

2048x8
(35 ns)

(AD9300) (AD9048)

CORRECTION
& IMAGING
OPTICS

LINEAR FIBER-
OPTIC BUNDLE

MPX

FLASH
ADC

SRAM

TRANSC.

TRANSPARENT
SECTION

FOCAL
PLANE

MPX

FLASH
ADC

SRAM

TRANSC.

READ-OUT BUS
(8 BITS)

Fig. 19   Schematic of system which scans a linear array of optical fibers to digitize images.

36

SECTION IV

EXPERIMENTAL RESULTS

1. THERMALLY CHOKED COMBUSTION PHENOMENA

(a) Combustion Initiation Process

Operation of the ram accelerator in the thermally choked mode is initiated by injecting the projectile, with the obturator still in contact with its base, into the accelerator tube at velocities in the 0.7-1.3 km/sec range by means of the light gas gun.[13] The entrance velocity of the projectile, its maximum outer diameter, and the composition of the pressurized propellant gas in the accelerator tube are selected so that the entrance Mach number is sufficiently high (typically M > 2.5) for its conical diffuser to "start." When the projectile-obturator combination pierces the first diaphragm and enters the first stage propellant mixture, the obturator drives a normal shock onto the projectile body, generating a subsonic flow region behind the projectile. The temperature of the shock-heated air that is compressed ahead of the projectile, as it approaches the entrance diaphragm, is sufficient to ignite the propellant mixture after the projectile enters the test section. The back plate is dislodged by the high frontal pressure on the obturator, thus allowing combustion products to flow through the passages in the obturator and t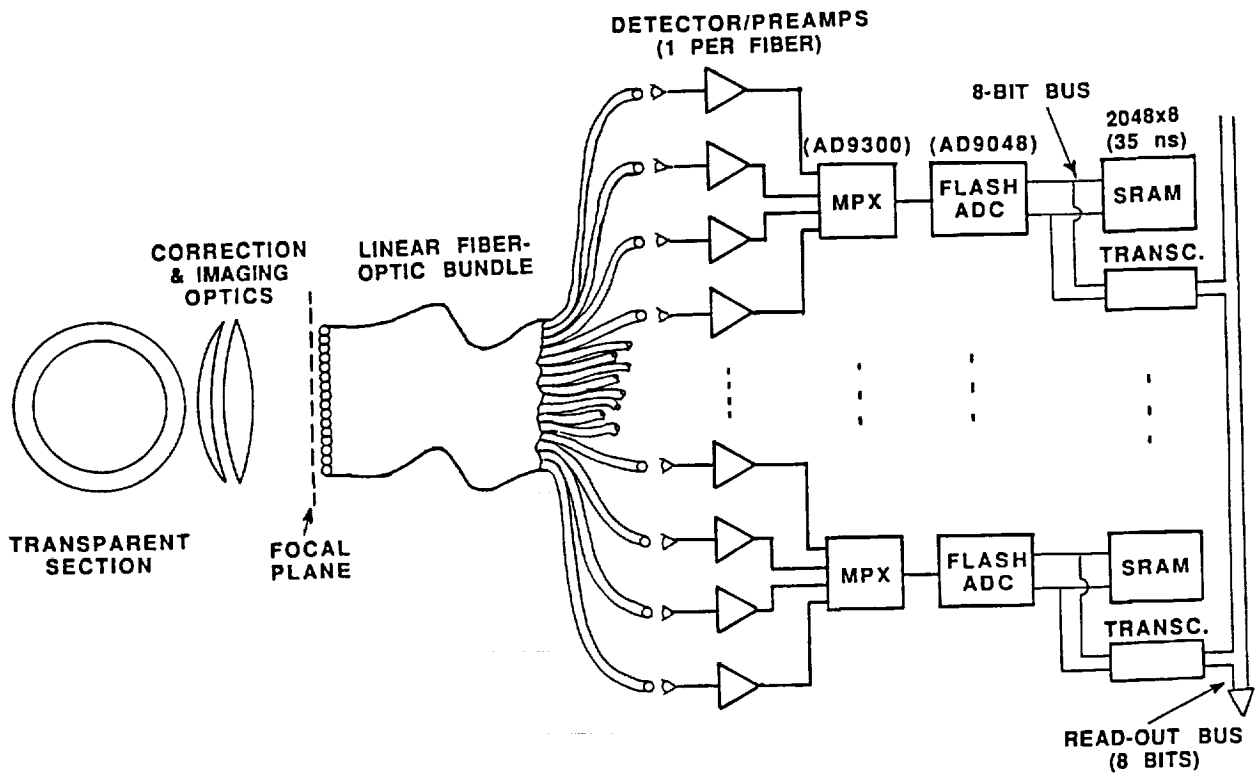o weaken the normal shock sufficiently to prevent it from outrunning the projectile. By the time the projectile has traveled one meter into the first stage of the test section (at fill pressures above 25 atm), a thermally choked zone is established behind the projectile, thus isolating the pressure field about the projectile from the effects of the decelerating obturator. The obturator continues to decelerate behind the projectile though it normally has enough residual velocity at the end of the test section to traverse the final dump tank.

(b) Effects of Propellant Composition and In-tube Mach Number

Typical data obtained while operating in the thermally choked ram accelerator mode, after the obturator has been gas dynamically decoupled, are shown in Fig. 20. Data from three different experiments are shown to compare the effects of Mach number, heat release, and the ratio of projectile velocity to CJ detonation speed (V/V$_{CJ}$) on the flow field. These data were collected from instrument stations that were simultaneously monitored with a pressure transducer, fiber-optic probe and EM sensor. The amplitudes of the pressure data have been normalized to the appropriate propellant fill pressures and the logarithmically amplified luminosity data have been normalized to the peak intensity transmitted by each of the respective fiber-optic probes.

Luminosity and pressure data for the three experiments have been time-synchronized and converted to a nondimensional length scale (tube diameters) by multiplying the time intervals (1 μsec) between data points with the projectile velocity, and dividing the result by the tube diameter. This nondimensional length scale is applied here to facilitate the comparison of data from projectiles that have very different velocities. All three experiments used the projectile configuration shown in Fig. 7, and silhouettes of this projectile are displayed (in tube diameters) in the upper left-hand corner of each pair of data traces with their throats aligned to the data by the EM signals of the respective experiments (for clarity the EM data are not shown).

The pair of data traces in Fig. 20a were collected at an instrument station located 1.03 m from the tube entrance just after the obturator has been gas dynamically decoupled from the projectile. The propellant mixture was $2.7CH_4+2O_2+5.6N_2$ and the fill pressure was 12 atm. At this point in the test section the projectile is operating at 1250 m/sec or $M_1 = 3.4$, which corresponds to $V/V_{CJ} = 0.72$. The typical tube wall pressure ratio profile for the thermally choked operating mode is observed under these operating conditions. The first abrupt rise in pressure is generated by the lead conical shock and its reflection; subsequently, the pressure rises gradually until the shock reflecting off the nose cone strikes the tube wall again, in the throat region of the projectile diffuser section. Several more reflected oblique shocks are observed in the region of supersonic flow over the projectile body. A normal shock system follows on the rear half of the projectile, producing a high base pressure. This shock system, which is believed to consist of a complex series of oblique and normal shocks, decelerates the flow to a subsonic Mach number with respect to the projectile. The tube-wall pressure ratio peaks at a value of approximately 20 in the region just behind the projectile. The decay in pressure following the peak is consistent with the assumption of subsonic heat addition (which accelerates the flow to thermal choking) and the subsequent unsteady expansion of the combustion products behind the choke point. The accompanying luminosity occurs on and behind the projectile and peaks within two tube diameters behind the base of the projectile.

Data from the fourth stage of a four-stage experiment (i.e., the test section of the ram accelerator was partitioned into four segments having different propellant mixtures) are shown in Fig. 20b. The projectile velocity is 2400 m/sec ($M_1 = 3.2$), which corresponds to 85% CJ speed ($V_{CJ} = 2840$ m/s) of the propellant mixture consisting of $3CH_4+2O_2+20H_2$ at a fill pressure of 46 atm. The pressure ratio profile over the nose cone of this projectile is similar to that observed in Fig. 20a, however, no reflected oblique shocks are observed in the region between the throat and the normal shock. A pressure ratio plateau of approximately 12, which extends for three tube diameters behind the projectile, is measured at the tube wall, followed by a region of

38

decaying pressure. The luminosity data show some activity at the normal shock front and the peak light intensity is observed to occur two tube diameters behind the projectile.

The differences between the data in Figs. 20a and 20b are primarily attributed to the difference in the value of the nondimensional heat release parameter of the propellant mixtures, i.e., $Q_a = 5.1$ and $Q_b = 3.4$. The lower heat release of the hydrogen-diluted mixture results in a lower peak cycle pressure than that of the nitrogen-diluted mixture, at a given in-tube Mach number, and a normal shock location that is farther back on the projectile. Note that the pressure spike observed near the projectile throat has the same amplitude ($\sim$10) in both mixtures, which is to be expected for mixtures having similar specific heat ratios ($\gamma_a = 1.369$ and $\gamma_b = 1.389$) and the same projectile geometry operating at nearly the same Mach numbers.

Shown in Fig. 20c are data from a projectile that passed by the sensors at 1480 m/sec ($M_1 = 4.0$) in a propellant mixture differing only slightly from that in Fig. 20a. The composition of this propellant mixture was $2.5CH_4+2O_2+5.5N_2$ ($\gamma_c=1.370$ and $Q_c=5.2$), its fill pressure was 31 atm, and the corresponding CJ speed was 1770 m/sec, thus $V/V_{CJ} = 0.84$ and $M_{CJ} = 4.9$. The amplitude of the pressure spike near the projectile throat is about 15. The peak cycle pressure ratio measured at the tube wall occurs approximately two tube diameters behind the projectile and has an amplitude of nearly 17. Ignition of the propellant in the throat region of the projectile is indicated by the coinciding peak in the luminosity data. Even though there are signs of combustion occurring on the projectile body, the experimental acceleration at this velocity is still close to that predicted for thermally choked operation. The light intensity decreases over the rear of the projectile and exhibits a relative maximum about one tube diameter behind the projectile's base.

The difference in Mach numbers in the nitrogen- and hydrogen-diluted mixtures at $\sim$85% CJ speed is due to the lower Mach number of the CJ detonation wave of the hydrogen-diluted mixture ($M_{CJ} = 3.7$) which, in turn, is due to its lower level of heat release. Thus, the higher Mach number of the nitrogen-diluted mixture increases the static temperature of the flow through the shock system and induces combustion on the projectile body at a lower fraction of CJ speed. The hydrogen-diluted mixture has not yet been driven fast enough to determine the point where ignition on the body will occur. The differences between the luminosity data in Figs. 20a-20c suggest that both Mach number and nondimensional heat release are significant factors in establishing the transdetonative propulsive cycle.

(c) Highly Instrumented Tube Section Data

The effects of projectile orientation with respect to the sensors on the tube wall data are indicated in the sequence of pressure and luminosity profiles shown in Figs. 16 and 17. These

data are from an experiment using a magnesium projectile having a 12.5° nose cone and the same body dimensions as shown in Fig. 7. The propellant composition was $2.7CH_4+2O_2+5.8N_2$, the fill pressure was 24 atm, and the in-tube Mach number was 4.2. The highly instrumented tube section was installed 4 m beyond the entrance to the test section. It was instrumented with pairs of orthogonal pressure transducers located in a helical pattern that wound itself around the tube once, resulting in sixteen separate pressure signals, two per station. Fin marks left in the tube indicated that the projectile fins passed directly over the instrument stations numbered 1, 3, 5, and 7 and the even numbered stations monitored the center line of the flow passage between the fins.

The effects of fins passing over the pressure transducers and luminosity probes are shown in Fig. 21. These data are from orthogonal sensors placed at stations 1 and 3 (data from stations 5 and 7 were essentially the same and are not presented). The pressure and luminosity probes in station 3 are rotated 90° with respect to the sensors in station 1. The redundant pressure transducers at each station showed exactly the same wave forms, thus only one pressure record from each station is shown. Below each pressure trace is a projectile silhouette with its length scaled to the local velocity and aligned with the data for reference. A large spike in these pressure traces is observed just behind the projectile throat, indicating the presence of a strong bow shock standing off the leading edge of each fin. Afterwards the pressure drops sharply as the flow expands from between the fin/wall gap. Another abrupt rise in pressure is observed on the rear body of the projectile; this is believed to indicate the intersection of the shocks from the fins. The pressure peaks again near the projectile base and subsequently decays.

Data from the fiber-optic probes at stations 1 and 3 indicate that the luminosity is strongly coupled to the shock waves generated by the projectile (Fig. 21). An abrupt rise in light intensity is observed that mimics the pressure pulse at the leading edge of the fins. Luminosity decays to nearly zero as the flow expands from between the fin/wall gap and it begins to rise again as the strong shock at the projectile base passes over the sensors. The luminosity then peaks behind the projectile in the subsonic combustion zone. Note that the peak light intensity behind the projectile has the same amplitude as the luminosity peak coinciding with the bow shock standing off the projectile fins. The projectile velocity is 88% CJ speed and the flow is nearly stagnated at the point where the fins first contact the tube wall, thus combustion in the throat region is expected to occur.

Pressure and luminosity data from orthogonal sensors that monitored the center line of the flow passages between fins, i.e., the fins were oriented 45° with respect to the sensors located at stations 2 and 4, are shown in Fig. 22. The data from station 4 are from pressure and luminosity probes located 90° with respect to the sensors in station 2. The data from stations 6 and 8 were essentially the same as stations 2 and 4 and the redundant pressure probes at each

station confirmed the symmetry of the pressure field within the flow passages. These pressure traces are significantly different from those collected directly underneath the fins (Fig. 21). The peak amplitude of the pressure pulse in the throat region is approximately one fifth that measured at the fin leading edges, and a strong pressure pulse is observed behind the throat which indicates the impingement point of the second shock wave reflected off the body. The next abrupt rise in pressure is followed by relatively small variations, which suggests that it is a normal shock rendering the flow subsonic on the rear half of the projectile. Peak cycle pressure at the tube wall is observed to occur in the combustion zone behind the projectile. Note that the four different pressure transducers measured the same peak amplitude (approximately 20) in the combustion zone (Figs. 21 and 22).

The most obvious difference in the luminosity traces from the sensors in-line with the fins and those in the flow passages is the character of the light pulse in throat region. Luminosity data from stations 3 and 4 (Fig. 22) show a rounded pulse that has approximately half the peak intensity of the luminosity in the combustion zone at the projectile base. For the logarithmic scale used here this corresponds to a relative difference of approximately one order of magnitude. This suggests that the primary ignition source at the onset of transdetonative operation may be the bow shocks standing off the leading edges of the fins. Note that the peak luminosity behind the projectile coincides with the peak pressure in the combustion zone of all four sets of data shown in Figs. 21 and 22. Variations in the luminosity data observed behind the projectile do not seem to correlate with any distinctive tube wall pressure phenomena.

The ability of the highly instrumented tube section to resolve details of the three-dimensional nature of the flow field makes it invaluable for examining ram accelerator phenomena.[14,38,39] This diagnostic capability can be used to evaluate the effectiveness of variations in projectile geometry and to provide high quality data for validation of CFD codes. Unsteady gasdynamic phenomena are now accessible to close examination and future experiments will be conducted to investigate transient events in unprecedented detail.

2. TRANSDETONATIVE PHENOMENA

The acceleration characteristics of different propellant mixtures are compared using the nondimensional thrust coefficient F/(PA), defined in Section II, where F is the experimentally determined thrust, P is the propellant fill pressure, and A is the tube cross-sectional area. The data in Fig. 23 show the variation of thrust coefficient with V/V_{CJ} for a projectile which has the same dimensions shown in Fig. 7, operating in a propellant mixture consisting of $2.5CH_4+2O_2+5.5N_2$. The reference number of this experiment is HS825. Projectile acceleration, and hence thrust, was

determined by differentiating a polynomial curve fit to the v-x data, which itself was obtained by center differencing the original t-x data. The order of the polynomial (typically 4th to 8th order) was chosen to minimize the standard deviation of the velocity data without generating excessive oscillations in the acceleration history. The solid curve in Fig. 23 is the thrust coefficient profile predicted by the one-dimensional theoretical model for the thermally choked propulsive mode.

The experimental thrust coefficient data in Fig. 23 follow the theoretical prediction very well up to about 90% CJ speed. The thrust profile drops to a relative minimum near this point and then increases with increasing projectile velocity. These acceleration "upsweeps" have been routinely observed when projectiles are allowed to approach the CJ speed of the propellant mixtures and they have proven to be very repeatable.[5-10] At the onset of the transdetonative propulsive mode it is believed that the thrust pressure acting on the projectile ceases to be sustained by thermal choking of the flow behind the projectile. At velocities between 80% and 90% CJ speed, the luminosity data from experiments indicate that ignition begins to occur in the flow passages around the projectile (Fig. 20c); however, since the experimental acceleration levels are close to the theoretical predictions, it is assumed that the flow is still thermally choked behind the projectile. The thrust of the thermally choked propulsive mode is independent of the location of the combustion processes and the relative Mach number at which heat addition occurs, if there is a thermal choking point at full tube area stabilizing the flow field. This invariance of thrust is a consequence of operating a propulsive cycle with an end state corresponding to an entropy extremum, as noted in Section II.

It is probable that the high static temperature of the shock-heated propellant gas at velocities above 90% CJ speed increases the chemical kinetic rates sufficiently to move the region of thermal choking closer to the projectile base. If all of the available heat release were to occur in the region between the projectile and tube wall in flow that is moving at a velocity less than the CJ speed with respect to the projectile, then the flow would certainly choke on the projectile body. This may result in a forward propagating overdriven detonation wave and the abrupt unstart of the projectile. If the heat addition process were only to release a portion of the available chemical energy on the projectile body, and the rate of heat addition were appropriately balanced by the area expansion due to projectile taper, then it is possible for the subsonic flow behind a normal shock to be accelerated to sonic velocity while it is still within the region between the projectile and tube wall. Heat could then be added to the flow beyond the choke point as long as the area expansion was rapid enough to maintain supersonic flow. This "mixed-mode" combustion process could readily transition to a fully supersonic combustion mode, causing a larger fraction of the available chemical energy to be released on the projectile body as its velocity increased.

When the flow is completely supersonic with respect to the projectile, only the combustion processes that occur on the projectile body can supply the energy needed to sustain projectile acceleration. In the transdetonative velocity regime, i.e., between 90% and 108% CJ speed, the experimental thrust coefficient profile shown in Fig. 23 demonstrates a trend in acceleration that increases with increasing velocity. This is consistent with a propulsive cycle that maintains a nearly constant supersonic exit Mach number, while increasing amounts of energy are released on the body as the projectile gains speed (Eq. 2.1). This could be the result of a mixed-mode combustion process which transitions to fully supersonic combustion operation as previously described.

Pressure and luminosity data taken from two different instrument stations are shown in Fig. 24 and a silhouette indicating the projectile length in tube diameters is shown for each data set. The projectile velocity for the upper and lower pair of data traces corresponds to fractions of CJ speed equal to 99% and 104%, respectively. Strong light intensities were detected in the throat region at both projectile velocities, and the higher Mach number case is beginning to show light emissions from the tip of the nose cone. There is a reduction of light intensity as the flow moves over the blunt base of the projectile, and an abrupt increase in luminosity is evident in the high pressure zone behind the projectile. Even though it is assumed that the luminosity is a function of the gas temperature, it is not clear whether or not the combustion activity behind the projectile is contributing to the thrust. Careful scrutiny of the luminosity profile from the 104% data set indicates that the light intensity on the projectile is much greater than that observed in the lower Mach number cases, indicating that a greater fraction of the propellant has combusted in the flow regions around the projectile.

3. SUPERDETONATIVE PHENOMENA

If the projectile continues to accelerate at superdetonative velocities and the propellant mixture is energetic enough, the chemical reactions will eventually go to completion within the transit time of the flow over the projectile and all of the heat release will occur on the projectile body, resulting in supersonic exit flow. At this point the projectile begins to operate in the "superdetonative" propulsive mode; i.e., all of the available chemical energy is released within the flow region between the projectile and tube wall. Experimental luminosity data from the same experiment discussed above (HS825) show a distinct zone of very low light intensity immediately behind the projectile when it is traveling at 114% CJ speed (Fig. 25). Strong nose light is evident, a slight dimming occurs in the throat region, luminosity increases on the rear half of the projectile and then abruptly drops at the projectile rear, after which a relatively long region of low level

43

luminosity is observed (approximately one projectile length long) before the light intensity again rises in the high pressure region behind the projectile.

The interpretation of these data (Fig. 25) is that significant combustion ahead of the projectile throat is occurring, which produces a drag force that counteracts the thrust generated by the expansion of combustion products over the rear of the projectile. This is consistent with the trend of decreasing thrust with increasing velocity that is indicated in Fig. 23. Similar behavior has been observed in all experiments that have accelerated projectiles to over 110% CJ speed. In the experiment numbered HS825, the projectile experienced a thrust minimum at about 115% CJ speed and then surged up to 117% CJ speed before abruptly unstarting. This final upsweep is often seen during the brief transient phase of a shock or detonation wave surging forward over the projectile.

(a) Effects of Prior Acceleration History

To gain further insight into the nature of the transdetonative and superdetonative propulsive modes, several multi-stage experiments were conducted in which projectiles were injected into a test mixture (having the same composition as the propellant mixture used in HS825) at velocities above its CJ speed (1770 m/sec). The pressure and composition of the propellant mixture in the ram accelerator stage just prior to the test mixture were chosen so that the projectile would enter the test mixture with a superdetonative velocity while the projectile was operating in the thermally choked propulsive mode in the preceding stage. This experimental condition was prescribed to eliminate the effects of entering a propellant mixture at a superdetonative velocity with the projectile already having heat release processes occurring on the body, as is suspected to be the case in the transdetonative mode. Consequently, the interpretation of these experiments is that the ensuing gasdynamic phenomena are due to the effects of the interactions of the shock wave system and accompanying boundary layers with the hypersonic projectile ($M_1 > 5$), and not a result of pre-existing on-body combustion processes interacting with the flow.

The velocity-distance profiles from the last 6 meters of three ram accelerator experiments are shown in Fig. 26. One set of data is from the single-stage shot HS825 (data from which are also shown in Figs. 20c, 23-25). The other two sets of v-x data are from the four-stage and three-stage experiments numbered HS820 and HS822, respectively. Both of these experiments had the last 4 m of the ram accelerator tube filled with a test mixture consisting of $2.5CH_4 + 2O_2 + 5.5N_2$ (same propellant used in HS825). The vertical dashed line in Fig. 26 indicates where the diaphragm station was located which separated the test mixture from the prior stage for the two multi-stage experiments. Note that no diaphragm was present at this location in experiment

44

HS825. The CJ speed of the test mixture is indicated in the lower right-hand corner of the figure and the fill pressure of the test mixture in each experiment is also shown.

Experiment HS820 was configured to have a first stage 2 m long at a fill pressure of 33 atm, a second stage 6 m long at 32 atm, a third stage 4 m long at 29 atm and a last stage, 4 m long, containing the test mixture at a fill pressure of 22 atm (Fig. 26). The propellant in the second stage consisted of $4.3CH_4+2O_2+3.6He$, which has an acoustic speed of 483 m/sec, and the composition of the third stage was $2.9CH_4+2O_2+12He$, which has an acoustic speed of 620 m/sec. This staging configuration injected the projectile at a velocity of 2140 m/sec into the test mixture, which corresponds to a Mach number of 3.5 at the exit of the third stage and a superdetonative entrance velocity into the test mixture of 121% CJ speed, corresponding to a Mach number of 5.9. The projectile gained approximately 30 m/sec within the first meter of the test mixture and then was weakly accelerated in the remaining 3 m, leaving the tube at approximately 2190 m/sec $(M_1 = 6.0)$.

Experiment HS822 was configured to have a first stage 4 m long at a fill pressure of 22 atm, a second stage 8 m long at 22 atm, and a third stage 4 m long containing the superdetonative test mixture at a fill pressure of 22 atm. The propellant composition in the second stage was exactly that used in the second stage of HS820. In this staging configuration the projectile left the second stage with an in-tube Mach number of 3.9 and a velocity of 1890 m/sec (Fig. 26), which corresponds to 106% CJ speed $(M_1 = 5.1)$ in the third stage test mixture. On this occasion the projectile passed through the test mixture at relatively constant velocity, exiting at ~1880 m/sec. This is an anomalous result, since typical one-stage experiments in this Mach number range either continuously accelerate the projectile to the end of the test section or to the point where an unstart occurs (HS825).

The relatively low accelerations observed at superdetonative velocities in experiments HS820 and HS822 were a surprising result, since the flight Mach numbers $(M_1 = 6.0$ and $M_1 = 5.1$, respectively) were sufficiently high that the drag would have decelerated them appreciably if there was not some combustion occurring on the body or behind the projectile in the base region of the flow. On the other hand, the projectile in HS822 entered the test mixture at a velocity at which it had demonstrated substantial thrust in one-stage shots. The results from these experiments raised some very important questions such as: Why did the projectile not experience the acceleration tendencies demonstrated by the thrust curve shown in Fig. 23? Why in HS820 did the projectile that entered the test mixture at a velocity above that at which it normally unstarts, not immediately unstart? The effects of mixture transition and propulsive mode transition need to be investigated further.

45

Some insight into the causes of these observed differences in performance in the superdetonative velocity regime is gained by examining the pressure and luminosity data from experiments HS820 and HS822 (Fig. 27). The effects of the higher in-tube Mach number are evident in the greater nose light intensity of the Mach 6 superdetonative shot (HS820), however, both pairs of data traces are very similar to the data shown from a superdetonatively accelerating projectile operating at a velocity of 114% CJ speed (Fig. 25). The major difference between the pressure traces of Fig. 27 and Fig. 25 is that the rise in tube-wall pressure at the projectile base appears to occur farther behind the projectile in HS820 and HS822, indicating that the effects of this pressure rise are not being communicated directly with the projectile. Perhaps the significant region of heat release is actually occurring behind the projectile and not on the projectile as previously hypothesized. In any case, it is apparent that the pre-condition of the flow field is very important in determining the operational characteristics of projectiles traveling at superdetonative velocities.

3. MICROSECOND THERMOCOUPLE DATA

Initial investigations using the thin-film thermocouples in the ram accelerator show output traces with an unexpected voltage fluctuation as the projectile passes,[32] followed by the temperature profile similar to that expected to be found in a turbulent combustion zone leading to thermal choking, as shown in Fig. 28. These data were from an instrument station located 13 m beyond the entrance diaphragm to the test section, the fill pressure was 24 atm, and the propellant composition was $2.8CH_4+2O_2+5.64N_2$. Projectile velocity and Mach number were 1700 m/sec and 4.7, respectively, ($V/V_{CJ} = 0.98$) at the time of projectile passage. The small oscillations on the temperature trace are due to a combination of mechanical vibrations and shock ionization associated with the pressure pulses. By inspecting Fig. 28 it can be seen that the spurious voltage output in the flow on the projectile body (i.e., the deviation from the zero axis is opposite in direction from the expected temperature rise) corresponds to the initial pressure oscillations (diffuser shocks) evident on the top trace. The magnetic trace shown indicates the location of the throat (the first zero crossing) and the base (the second zero crossing) of the projectile in relation to the temperature and pressure traces. Based on the representative calibration curve shown in Fig. 13, the temperature in the region of maximum pressure is ~1100K. The voltage output of the thermocouple continued to increase after the passage of the peak pressure region and reached levels corresponding to ~3000K. However, due to the spurious voltage output and excessive oscillations, these temperature data from this experiment are not considered very quantitative.

The thermocouple probe was cleaned with alcohol and reinstalled at the same location for the next experiment, which was a duplication of the prior shot (same propellant composition and

46

projectile configuration), except that the fill pressure of the mixture was increased from 24 atm to 33 atm. Consequently, the projectile passed the instrument station at a higher velocity of 1850 m/sec (106% CJ speed). The thermocouple output trace for this experiment is shown in Fig. 29, along with the corresponding pressure and magnetic traces. It can be seen that the temperature profile of the combustion zone behind the projectile body is similar to that shown in Fig. 28, however, these thermocouple data do not exhibit any signs of the spurious output previously detected on the projectile body. The temperature peaked about one projectile length behind the projectile with an amplitude of ~2000K. It is interesting that the peak cycle temperature was not at the tube wall as the projectile passed underneath the sensor, indicating that if there was any combustion activity on the body it must have been occurring away from the tube walls.

The oscillations and spurious output from the thermocouples during projectile passage has been observed with other thermocouple probes when they are first subjected to the ram accelerator pressure fields. Thermocouples being used for the first time exhibited spurious output when exposed to the shock waves generated by the projectile, but when used in subsequent shots they showed no such inclination. This led to the belief that this was a strain gauge effect caused by the depression of the face of the nickel wire into the probe body. Due to the fact that this effect is witnessed only on the first use of any thermocouple sensor, it was hypothesized that the first pressure pulse on the face of the thermocouple probe pushes the nickel wire into the epoxy, effectively seating it in such a way that additional pressure pulses have no further effect. This phenomenon eliminates the strain gauge effect and the consequent spurious voltage when the sensor is used again.

To circumvent the strain gauge effect the next series of probes was made with about 2 mm of nickel wire left protruding from their faces, and then exposed to a detonation wave having a peak pressure of approximately 1,000 atm. This "preseated" the nickel wire prior to having it nickel plated. The results showed an elimination of the strain gauge effect, as exhibited in Fig. 30, which shows a voltage trace of one of the preseated thermocouples in its first firing after being preconditioned. The corresponding pressure data are also shown. These data are from a detonation wave traveling at nearly 2500 m/sec in a combustible mixture of $1.6CH_4+2O_2$ at a fill pressure of 23 atm. No spurious output or excessive oscillations were observed from the sensor during this experiment.

The response time of the thermocouple is also a major point of interest, due to the need for it to be very fast. Theoretically, response times of 15 and 55 μsec for probes having a nickel plating thicknesses of 2.5 and 10 μm, respectively, are predicted.[32] No accurate way of measuring the thickness of the nickel layer on the face of the probe was available, although it was

believed to be between 5 and 15 μm, according to the company which did the plating. By examining the thermocouple data from the step-temperature input of the detonation wave shown in Fig. 25, the response time of the thermocouple probe can be estimated. The definition of response time is the time required for the junction temperature to reach 63.2% of the amplitude of a step-temperature change of the exposed plating surface.[33] From Fig. 30, the response time is approximately 25 μsec, corresponding closely to the times predicted for the plating thickness used.

The luminosity traces were also investigated and the preliminary findings suggest that the assumptions made previously regarding the luminosity data and how it relates to heat release may sometimes be in error. It has been assumed that the intensity of the observed light emissions is proportional to the temperature of gas and thus provides an indication of combustion activity. However, the luminosity and thermocouple data do not always correlate, as demonstrated by the pressure, luminosity, and temperature data shown in Fig. 31. Also shown is an appropriately scaled projectile silhouette that has been aligned with the data. These data are from a projectile traveling at 1910 m/sec ($M_1 = 4$) in a propellant mixture composed of $4.6CH_4 + 2O_2 + 3He$ at a fill pressure of 25 atm. It can be seen that the luminosity (logarithmically amplified) increases rapidly in the region of the initial pressure pulses, after which it abruptly decreases as the pressure decreases. The thermocouple output voltage (amplified 100 times in this case) is observed to rise behind the projectile and to reach a relatively steady plateau at a level corresponding to ~1000 K in the region where the luminosity abruptly decreases. The lack of a temperature rise at the tube wall as the projectile passes by the sensors indicates that the observed luminosity may be due to phenomena occurring on the projectile body (e.g., boundary layer combustion) or emissions from the shock-heated flow itself. The decrease in observed luminosity in the region where the tube-wall temperature is at a maximum is not at all consistent the previously stated assumption, thus there is some doubt as to the relation of the luminosity data to combustion activity in this case.

The calibration method described earlier produced calibration plots of output voltage vs. temperature which followed linear theory as predicted. However, the amplitudes of the thermocouple data based on these calibrations have failed to show a close correspondence with the temperatures predicted by the Hugoniot theory for the thermally choked propulsion mode. These discrepancies may be due to the extensive extrapolation of the calibration curves necessitated by the lack of a convenient high-temperature calibration source. The coupling of strain gauge effects with the thermal EMF may also lead to inaccuracies in the measurements. In any case, this preliminary effort in developing a robust, fast-response thermocouple has resulted in a low-cost technique for manufacturing the sensors and has indicted that high temporal resolution of the tube-wall temperature history may be achievable with further refinements.

48

5. SPECTROSCOPIC EXPERIMENTS

Spectra obtained from six experiments are discussed here. A summary of the propellant mixtures, fill pressures, velocities, Mach numbers and spectral regions investigated for each shot is presented in Table 2. The propellant mixtures of the third stage were used for this series of spectral investigations. The shot number refers to the number of the shot in the sequence of ram accelerator shots since operations began in October 1985. The data set numbers in the following text refer to the number of the shot in the sequence of the spectral experiments.

Table 2: Summary of Test Mixtures for Spectroscopic Experiments.

Data Set No.	Propellant Mixtures	Shot No.	Fill Pressure (atm)	Velocity (m/sec)	Mach No.	Spectral Region (nm)
1	$2.6CH_4+2O_2+13He$	HS779	43.2	2380	3.66	580 – 700
2	$2.8CH_4+2O_2+14He$	HS781*	41.2	2290	3.50	580 – 700
3	$2.8CH_4+2O_2+14He$	HS782*	41.8	2270	3.45	630 – 790
4	$2.5CH_4+2O_2+13He$	HS786	39.1	3100^+	4.75	710 – 860
5	$2.7CH_4+2O_2+13He$	HS788	31.3	2300^{++}	3.54	710 – 860
6	$2.7CH_4+2O_2+13He$	HS789	42.2	2270	3.50	710 – 860

* Nickel-coated projectiles.
+ Overdriven detonation wave velocity at instrument station.
++ Unstart shock wave velocity (no combustion).

As discussed earlier (Section III), two gratings were used. The first grating, blazed for 500 nm, was used for the first two data sets. The second grating, blazed for 770 nm, was used for the other data. Binning by 20 was generally used; however, data sets 5 and 6 were binned by 3. The area on the CCD array on which photons impinge varies with binning, so the counts for data binned by lower numbers are lower.

Data set 1 is presented in Fig. 32a. It spans the wavelength range of 580 to 700 nm. The projectile velocity at this station was 2380 m/sec ($M_1 = 3.66$), the propellant mixture was $2.6CH_4+2O_2+13He$, and the fill pressure was 43.2 atm. Figure 32b shows the luminosity data, pressure distribution, and throat position of the projectile at the same station. The y-axis is

unlabeled since only the qualitative features of the traces are of relevance for this discussion. The duration of radiation was approximately 250 μsec.

Data set 2 is presented in Fig. 33a. A nickel-coated projectile was fired in this shot, and the mixture was slightly different from that of data set 1 (2.6CH$_4$+2O$_2$+14He), the fill pressure was 41.1 atm, and the projectile velocity was 2290 m/sec (M$_1$ = 3.5). The curve shape of data set 1 appears slightly broader than data set 2. The pressure, luminosity and EM traces associated with data set 2 are shown in Fig. 33b. There is much less luminosity observed on the projectile body in this shot than the prior experiment (Fig. 32). Projectile orientation with respect to the sensors could account for some of the differences in the broadband luminosity data. Not enough experiments have been conducted to determine if the nickel coating provides a significant protective surface which can enhance the high speed potential of the projectiles.

Data set 3 (Fig. 34) was taken in the same mixture as data set 2, with a nickel-coated projectile as well. The fill pressure was 41.8 atm and projectile velocity was 2270 m/sec. The second grating, blazed for 770 nm, was fitted for the spectrometer in this shot. The wavelength region observed was 630 to 790 nm. The spectral curves from data sets 2 and 3 match very well. The luminosity data of data set 3 also match data set 2 and for that reason are not presented; the only variation is that a slight amount of nose light was detected at the spectrometric station in the experiment producing data set 3. One might speculate that the nickel coating on the projectile's nose cone was not as well distributed as on the first nickel-coated projectile and wore off.

The unreduced data set 4 is presented in Fig. 35a because the CCD array was saturated. Only the few parts of the spectrum that were captured can be properly reduced. The projectile unstarted prior to reaching the spectrometer probe and pushed an overdriven detonation wave ahead of it at having a velocity of 3.1 km/sec. The propellant mixture was 2.5CH$_4$+2O$_2$+13He and the fill pressure was 39.1 atm. Although the CCD was saturated, O$_2^+$ absorption bands[41] were strong enough to be detected (Fig. 35b). Concurrent luminosity data were taken with a blue filter in preparation for the following shot. This was a crude way to check if there were detectable light levels in the blue. These data did not contribute any information about the flow in this experiment.

Figure 36a is spectral data set 5. The wavelength region is 690 to 845 nm and the data are binned by 3. These data are also from an unstarted condition. The velocity of the pressure wave was approximately 2300 m/sec. The Chapman-Jouguet detonation velocity for this mixture (2.7CH$_4$+2O$_2$+13He) was 2740 m/sec. The peak of the radiation occurs around 835 nm. Near

the peak radiation, a pressure-broadened absorption band is visible (Fig. 36b). An emission line for CO at 847.5 nm also appears to be present.

Figure 37a is spectral data set 6. The projectile drove past the spectrometer probe at 2270 m/sec. The wavelength where peak radiation occurs is very similar to that for data set 5. Both of these shots had the same propellant mixture ($2.7CH_4+2O_2+13He$), but the fill pressure of data set 6 was higher (42.2 atm). An emission line near where CO emits (847.5 nm) is again detected (Fig. 37b). Molecular oxygen emits at 839.5 nm which appears to correspond to the feature labeled in Fig. 37b. The repeatability of these features lends credibility to their detection. The luminosity data at this same station are shown in Fig. 37c. The luminosity probe was newly constructed, so its fiber surface was very clean and flush-mounted to the tube wall. The first light spike is associated with the normal shock on the body. The relative intensity of the normal shock light is much higher than the following combustion light suggesting that more species reacted in a shorter period of time, reminiscent of detonation wave light emission. Thus, more radiation appears to be generated from shock heating than the combustion activity behind the projectile.

To get an idea of how much intensity attenuation is caused by soot deposition on the face of the optical probe, a response function was recorded after collecting data set 2. As can be seen from Fig. 38, the reduction in transmission was approximately 20% at the midpoint of the data. This crudely estimates the effect of the soot deposition on the transmissivity of the fiber for this shot. The amount of soot generated depends on the equivalence ratio of the propellant. In order for the effects of the soot-laden gas to be evaluated, an experiment to measure density and size distribution would have to be developed. This was beyond the scope of the present work.

Flame temperatures from continuum radiation can be estimated using the two color temperature method,[40] whereby measurements of relative intensities over two wavelength regions are used. This can be done with spectral data or with two color filters. The assumptions about the variation of emissivity with wavelength are uncertain, so the result may not be very reliable. The spectral radiance of a blackbody is dependent on temperature only, but the spectral radiance of a particle-laden gas is dependent on composition, pressure, and temperature. In addition, several experimental apparatus considerations must be taken into account before flame temperatures can be determined. First of all, the optical cable itself is acrylic and has high attenuation over the range of wavelengths studied. Second, several photodetectors are used to acquire the data, so they must be calibrated. There are also additional errors to consider in aligning the fibers with the sensors and the filters. Reflections of the light from the filters decreases the throughput.

This preliminary attempt to spectroscopically analyze the flow field of a ram accelerator projectile was successful in detecting absorption and emission bands in the near infrared region. Using detection equipment designed for resolving the spectrum of faint stars proved to be a viable way to collect spectral data from the short duration ram accelerator experiments. Greater sensitivities are required to get the temporal resolution needed to determine the points where the onset of combustion begins and other gas dynamic phenomena of interest. Pressure broadening of the spectral lines is a significant problem in the high pressure combustion zone, which may ultimately limit the potential of any in-bore spectroscopic technique. Nevertheless, the potential for gathering pertinent data on species concentrations has been demonstrated with a relative low-technology apparatus, thus a well-funded effort could realize high quality data that would be of interest to many of those who are involved with hypersonic research.
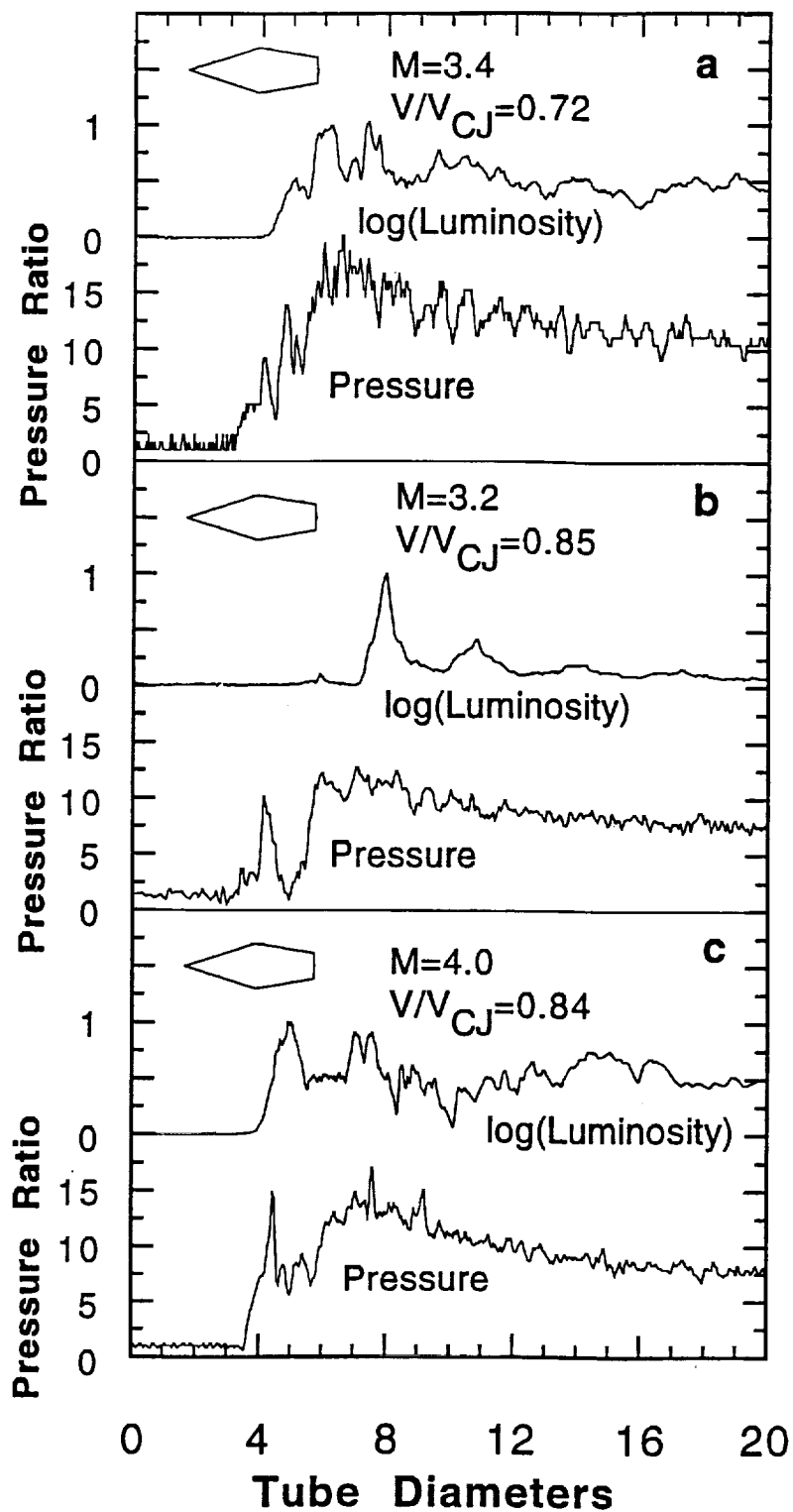
Fig. 20   The effects of Mach number and propellant mixture composition on tube-wall pressure

and luminosity data.   (a) HS833   (b) HS883   (c) HS825
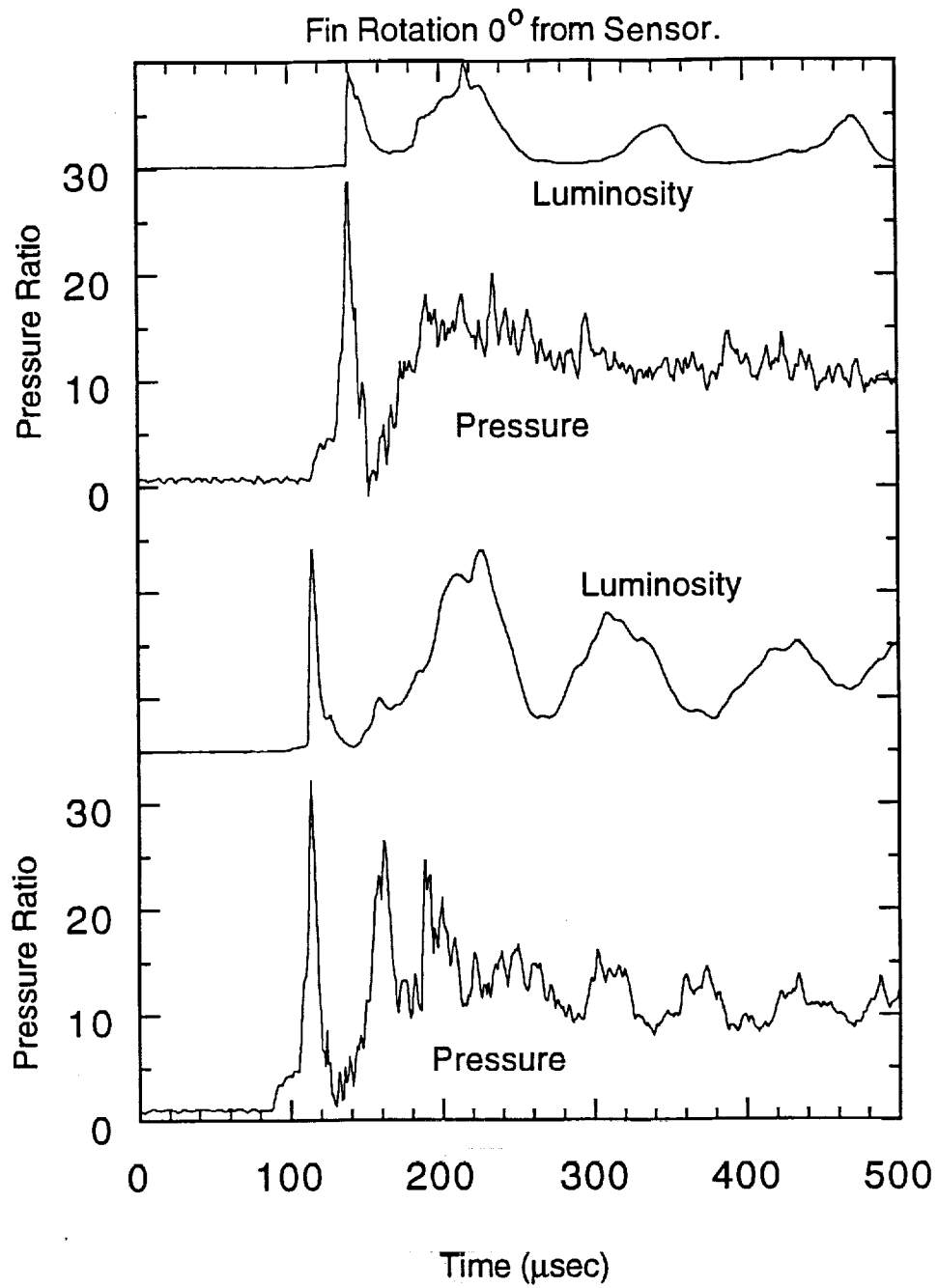
Fig. 21 Pressure and luminosity data from sensors located along centerline of fins.
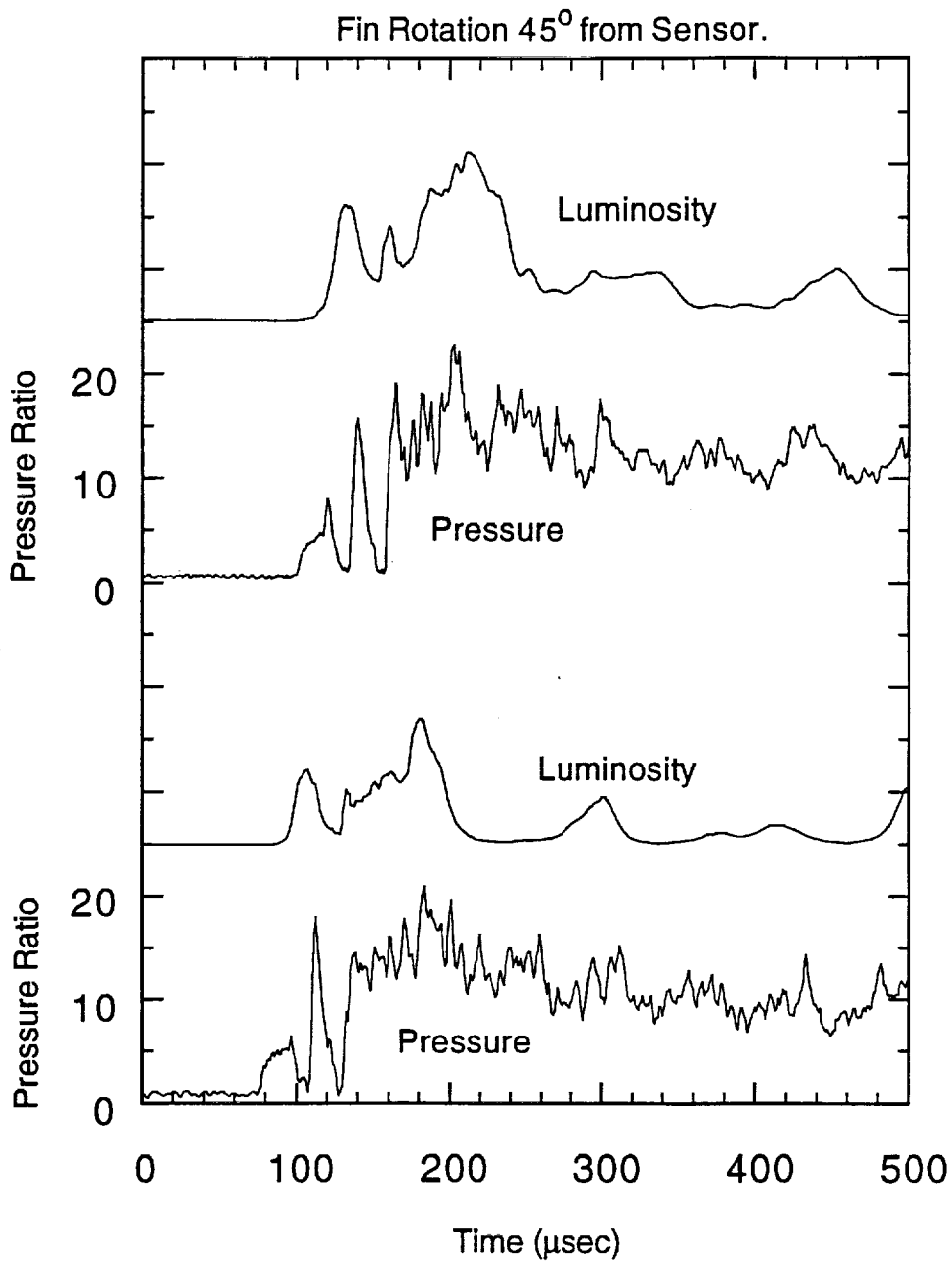
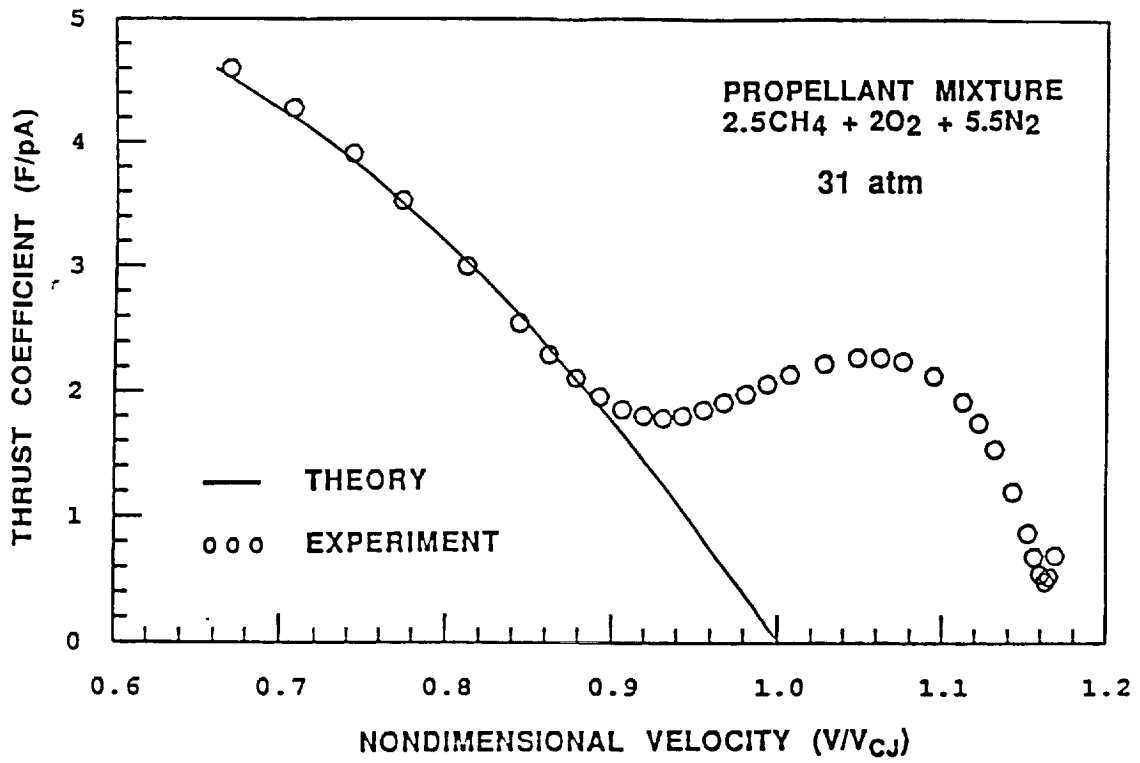Fig. 22   Pressure and luminosity data from sensors located 45° from centerline of fins.

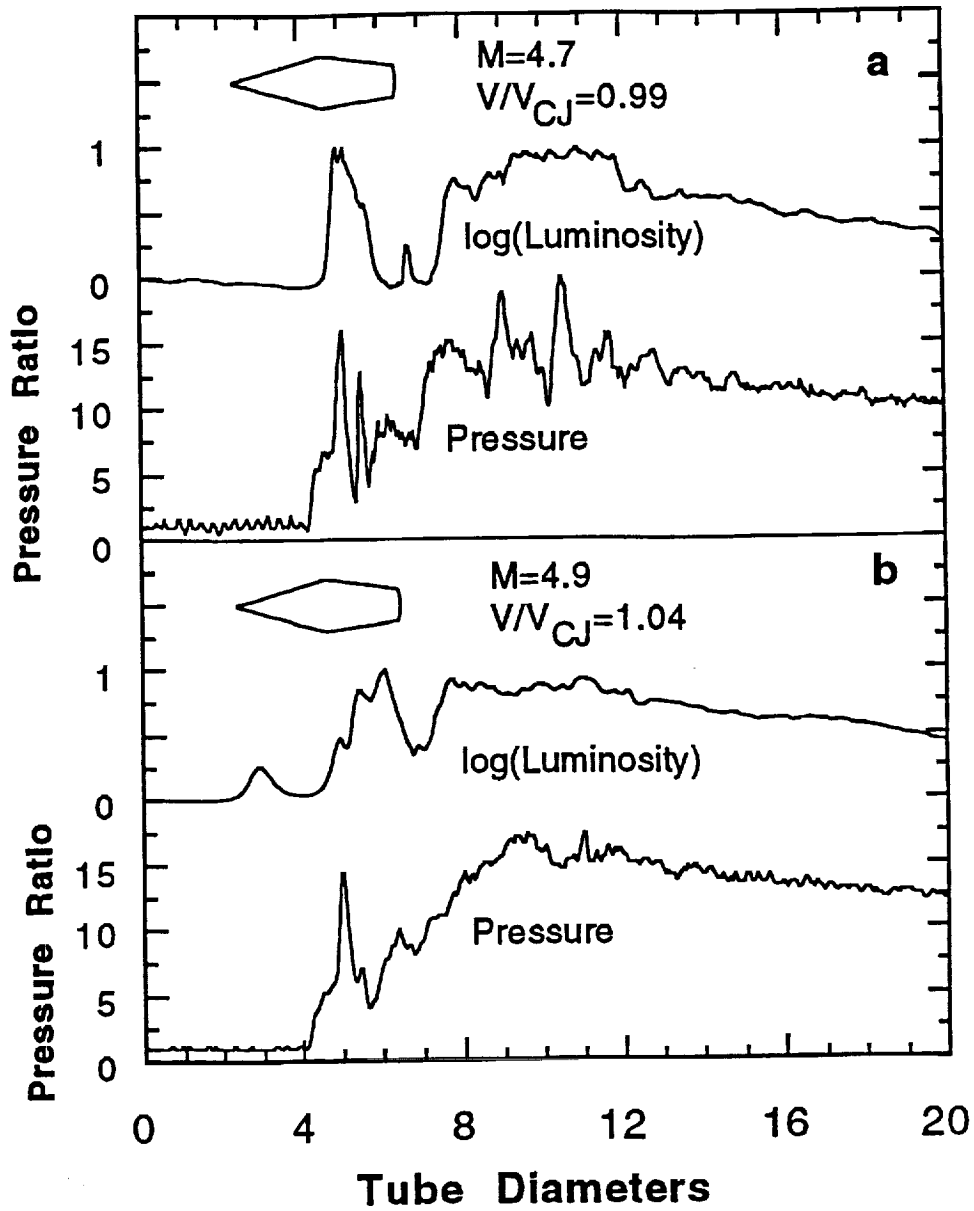Fig. 23   Theoretical and experimental thrust coefficients as function of projectile velocity.

Fig. 24   Pressure and luminosity data from the transdetonative velocity regime.
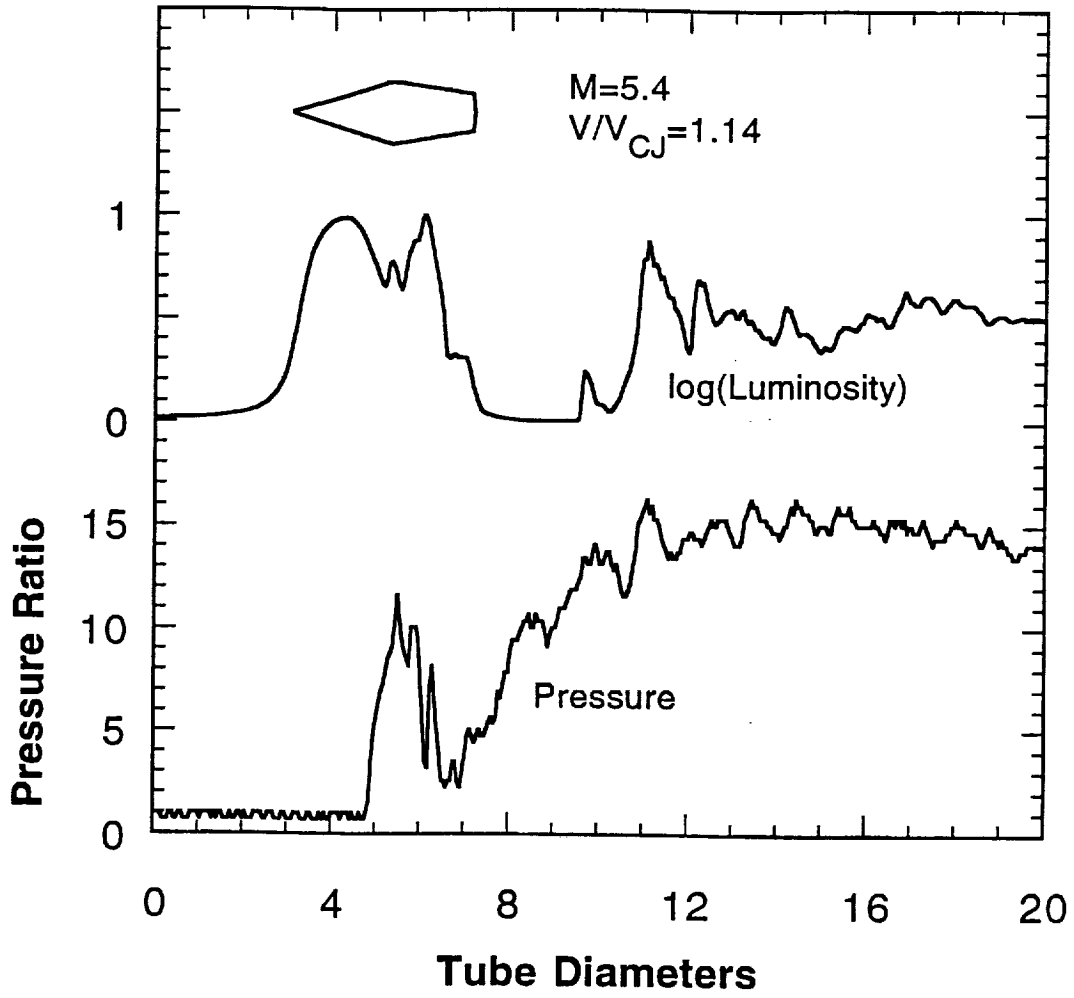
Fig. 25   Pressure and luminosity data from the superdetonative velocity regime.
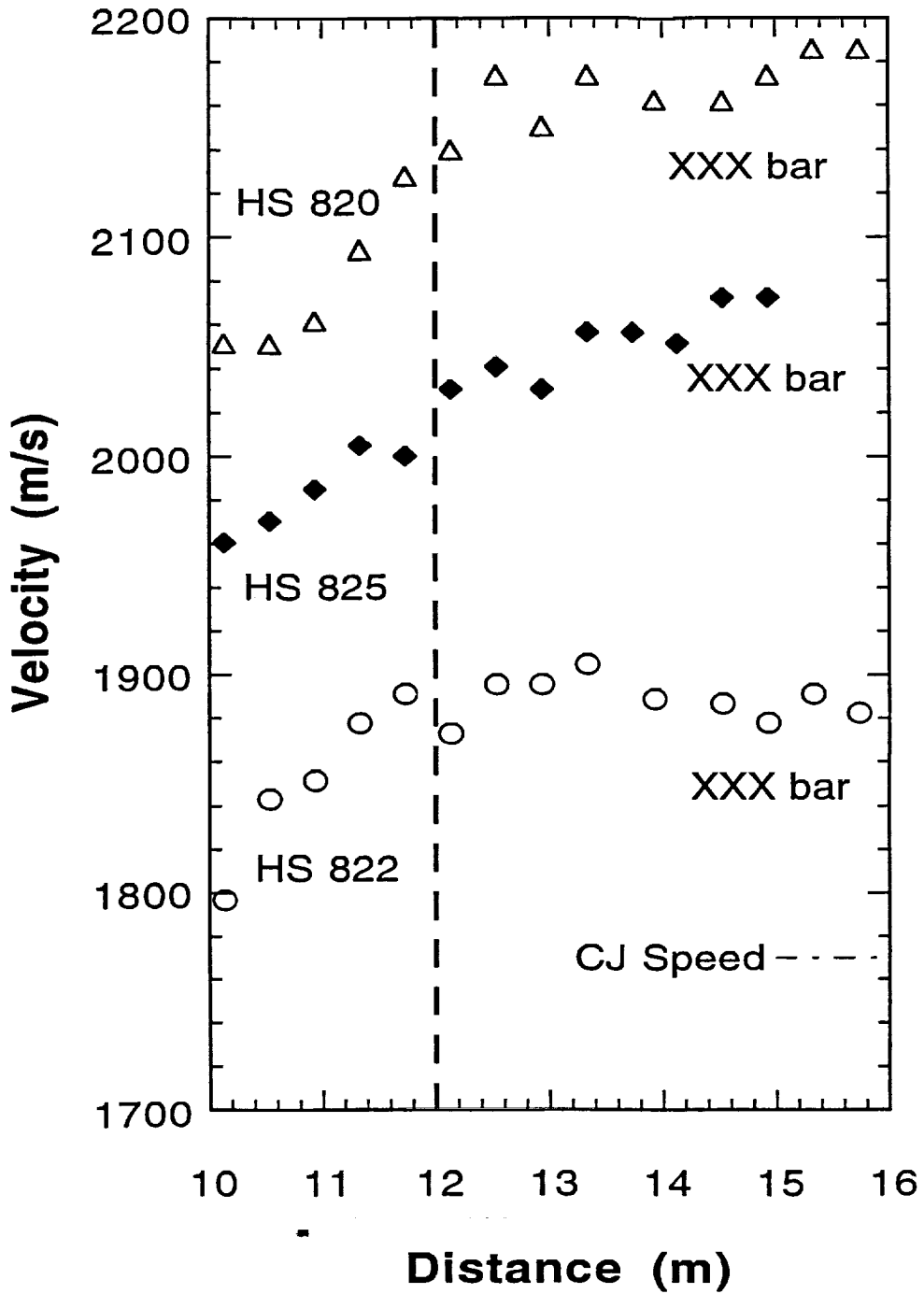
Fig. 26   Velocity-distance data from several experiments in superdetonative velocity regime.
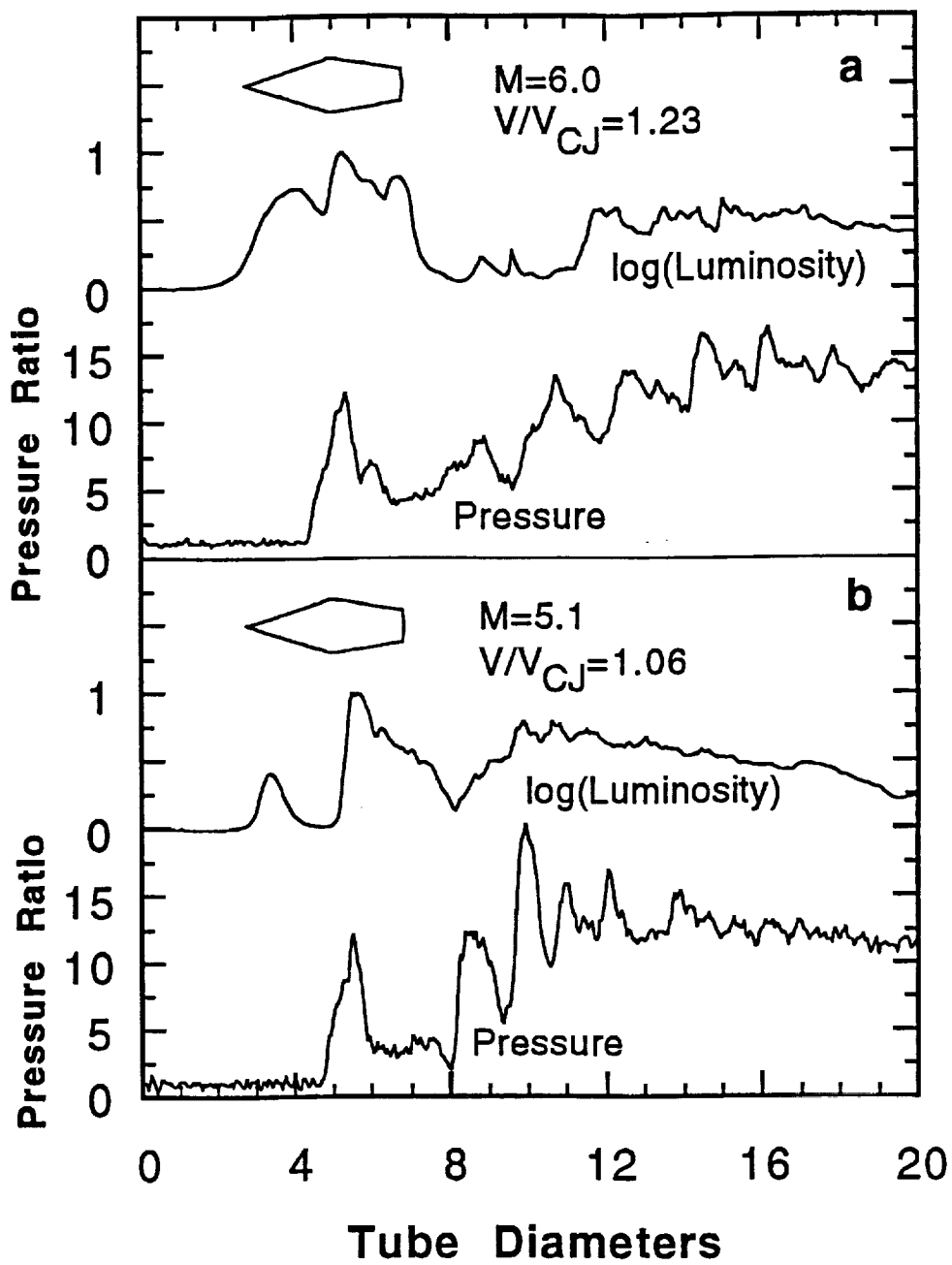
Fig. 27   Pressure and luminosity data from experiments (a) HS820 and (b) HS822.
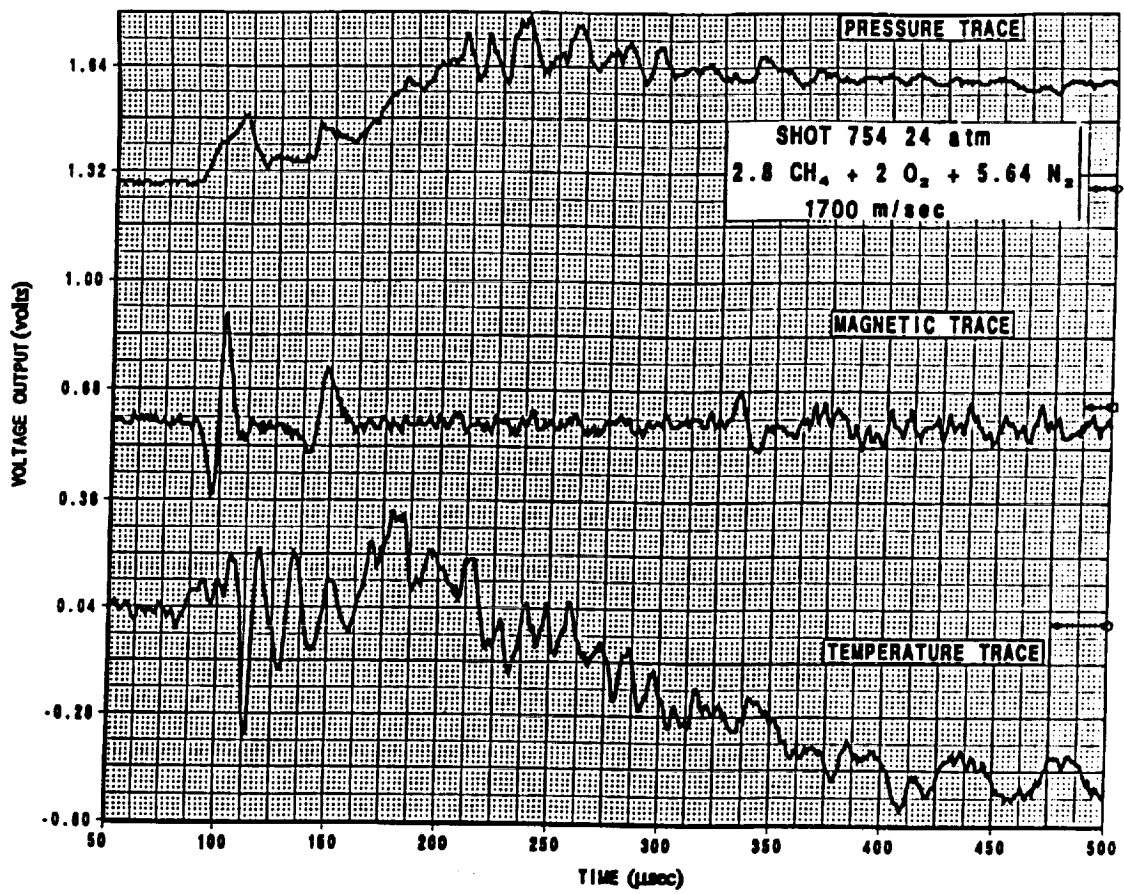
Fig. 28   Pressure, temperature, and electromagnetic data from transdetonative velocity regime.
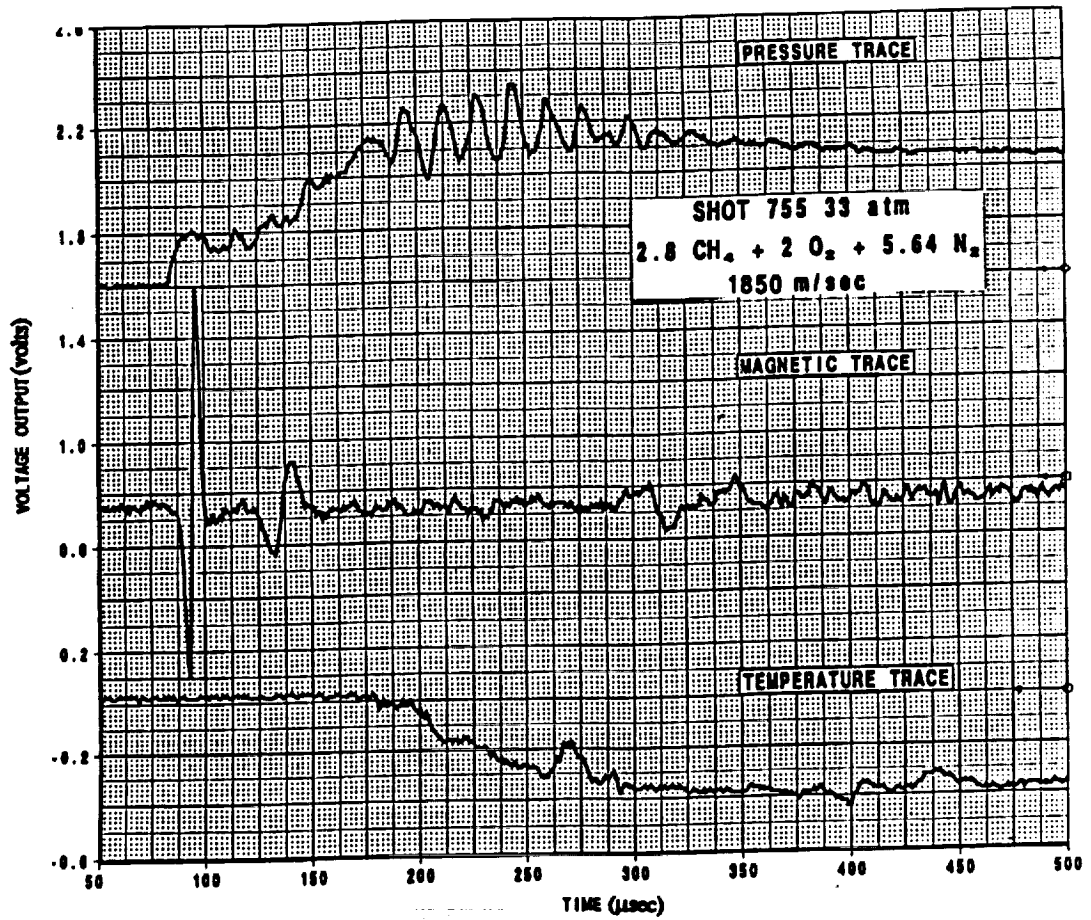
Fig. 29 Pressure, temperature, and electromagnetic data from superdetonative velocity regime.
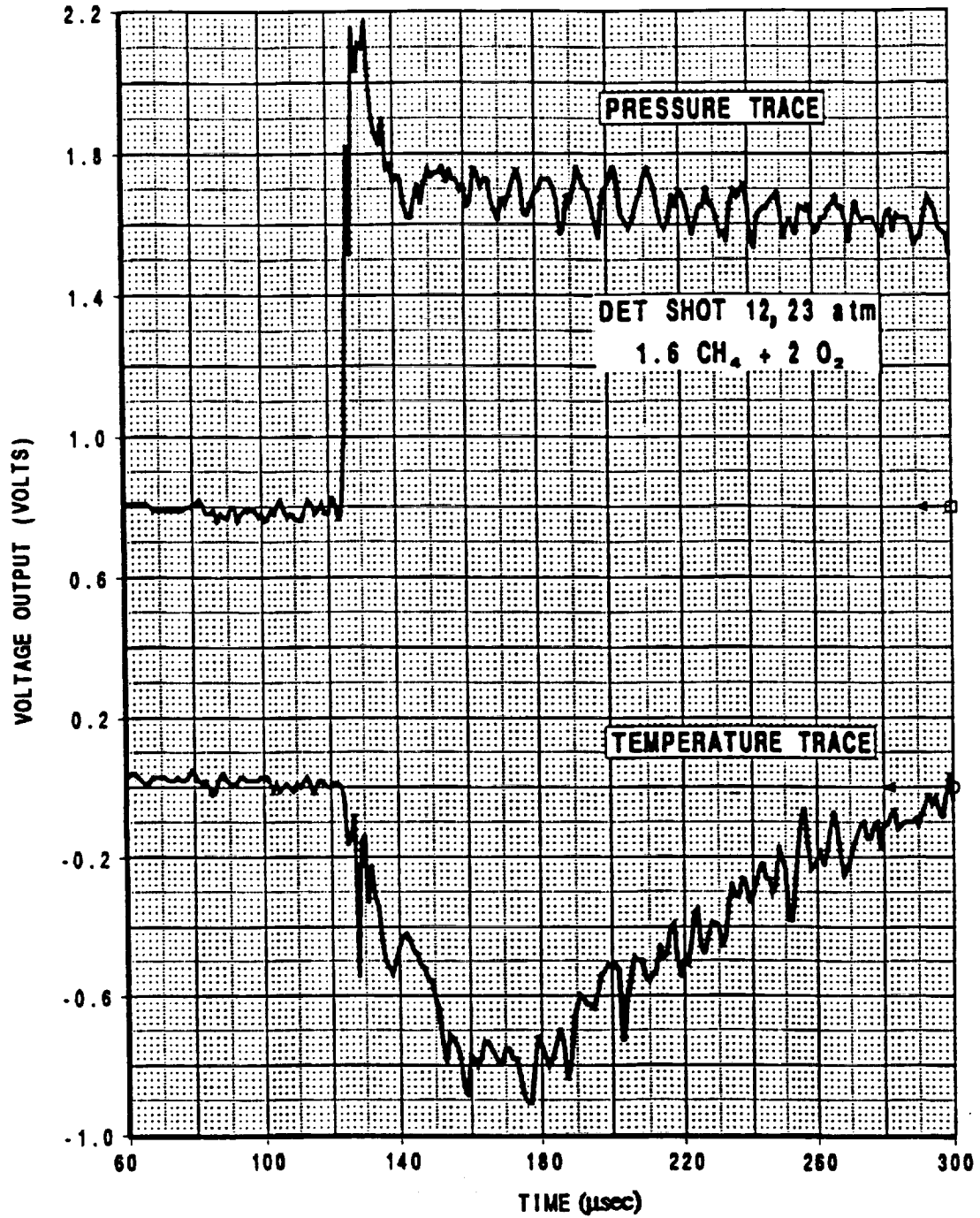
Fig. 30   Pressure and temperature data generated detonation wave.
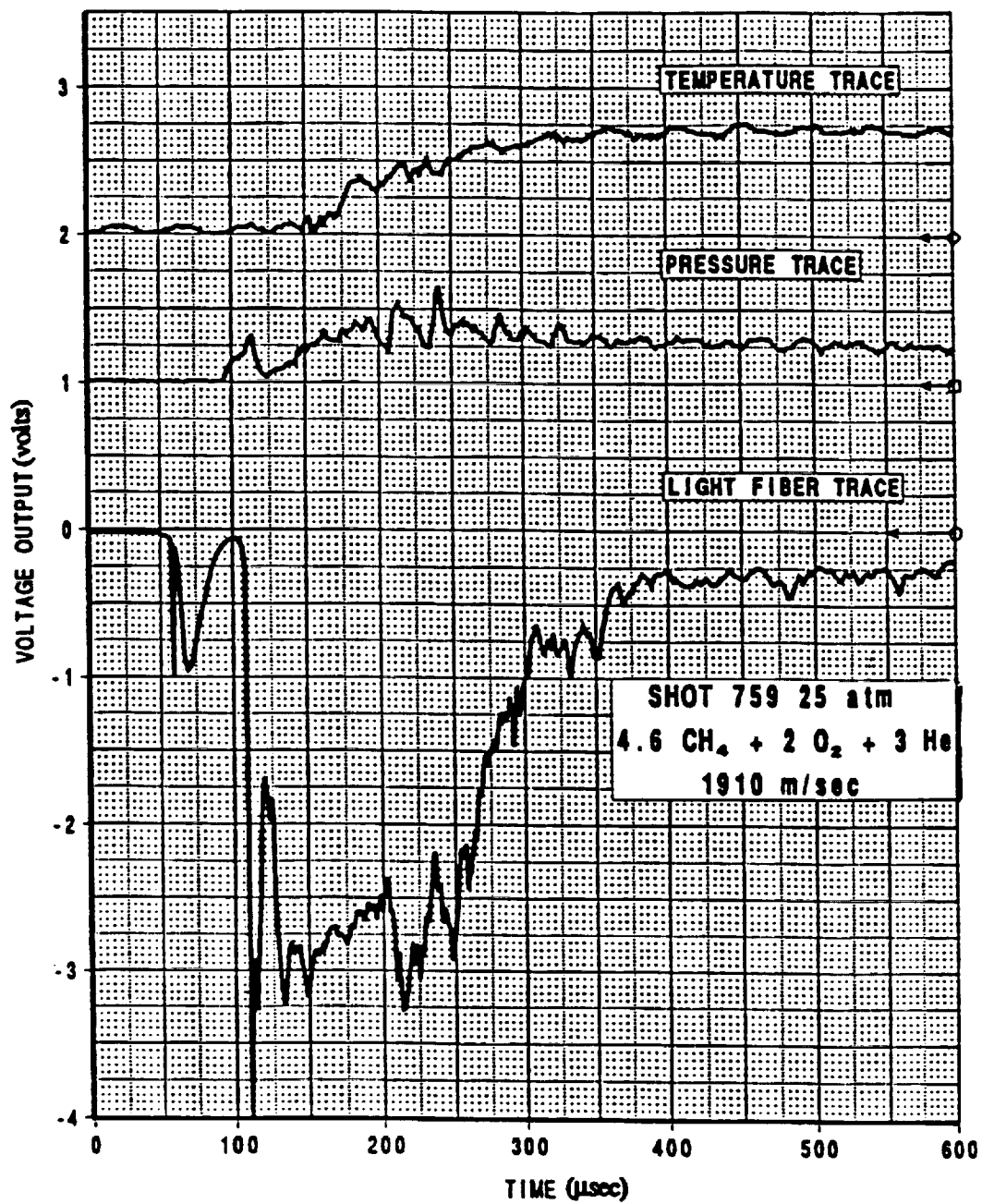
Fig. 31   Pressure, temperature, and luminosity data from subdetonative velocity regime.
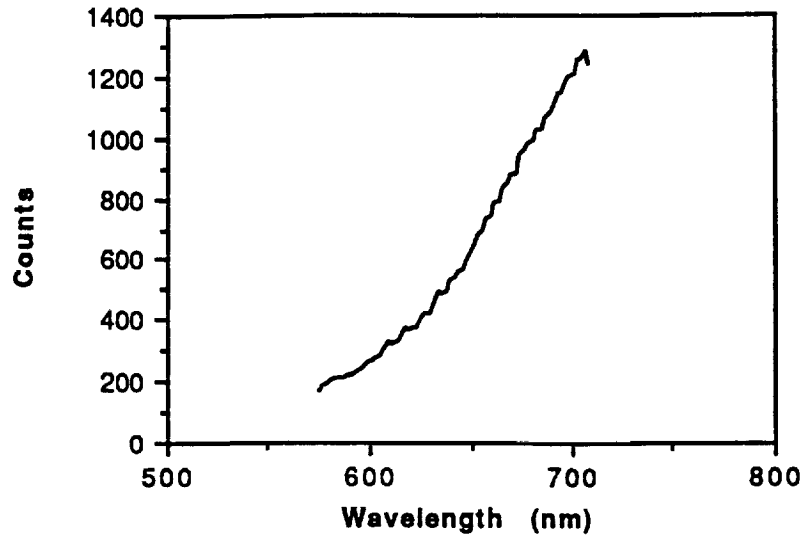
Fig. 32a   Data set 1 reduced from experiment HS779.
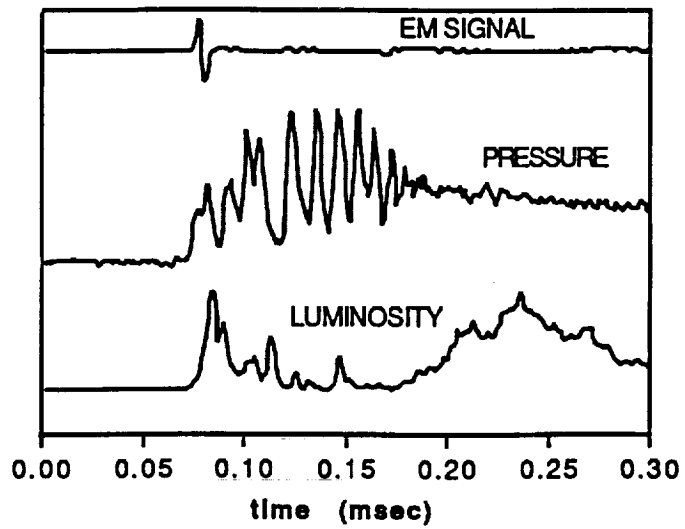
Fig. 32b   Luminosity, pressure, and EM data from spectroscopy station of HS779.
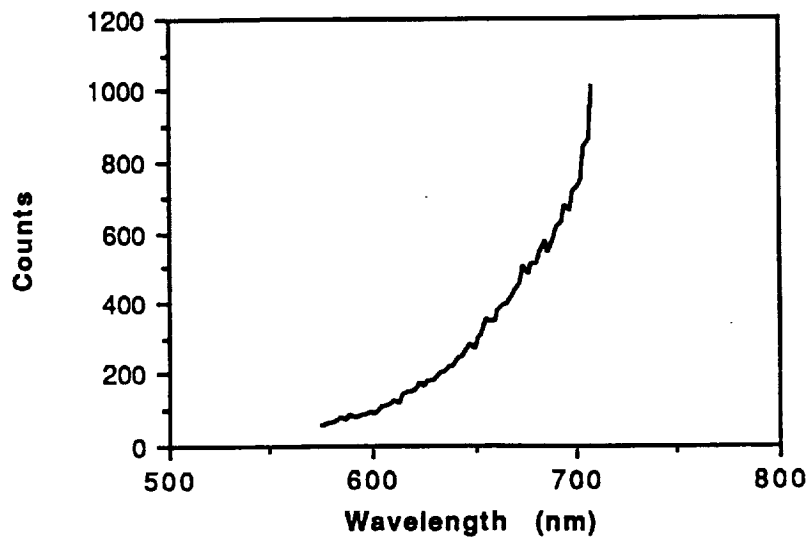
Fig. 33a   Data set 2 reduced from experiment HS781.
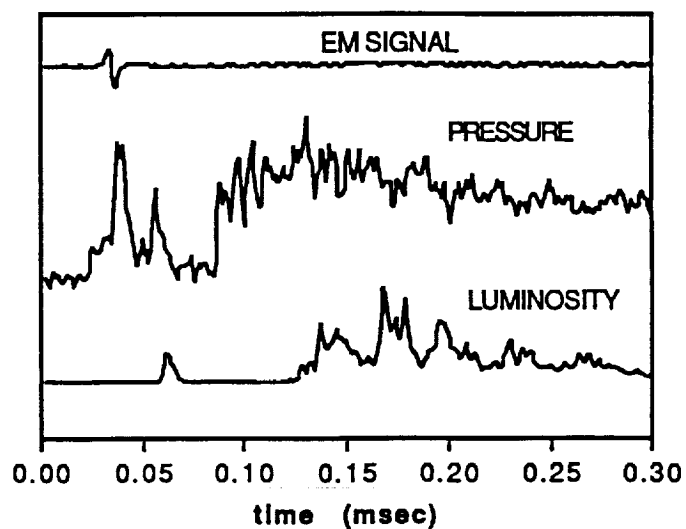
Fig. 33b   Luminosity, pressure, and EM data from spectroscopy station of HS781.
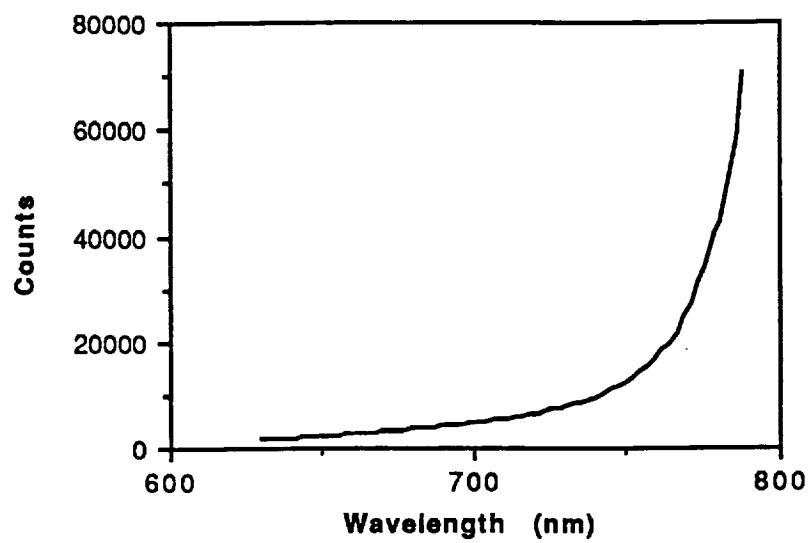
Fig. 34   Data set 3 reduced from experiment HS782.
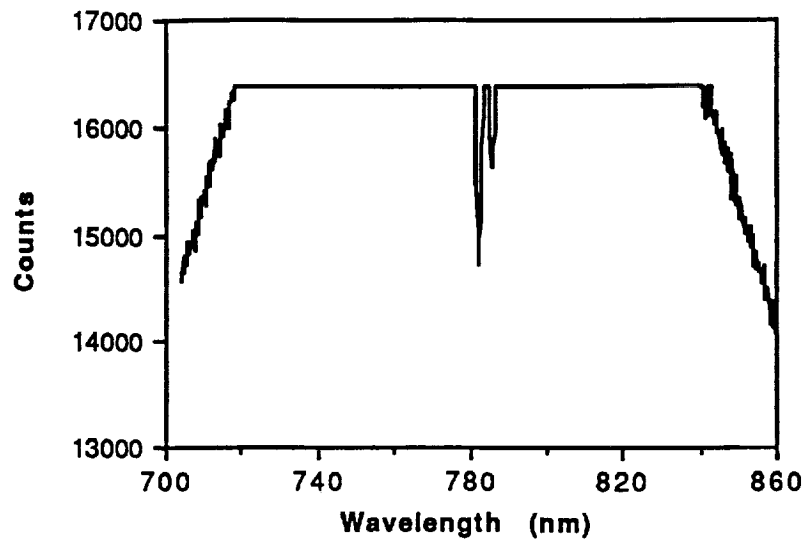
Fig. 35a   Unreduced data set 4 from experiment HS786.
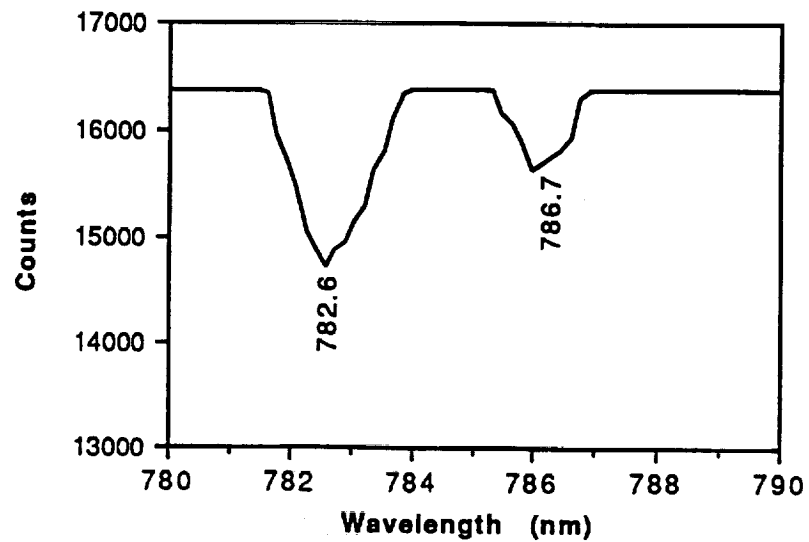
Fig. 35b O_2^+ absorption bands in the spectrum of an overdriven detonation wave.
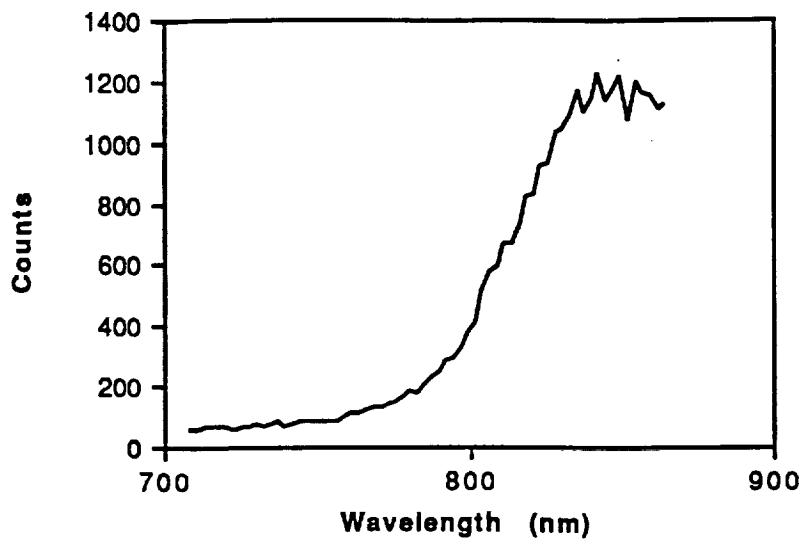
Fig. 36a   Data set 5 reduced from experiment HS788.
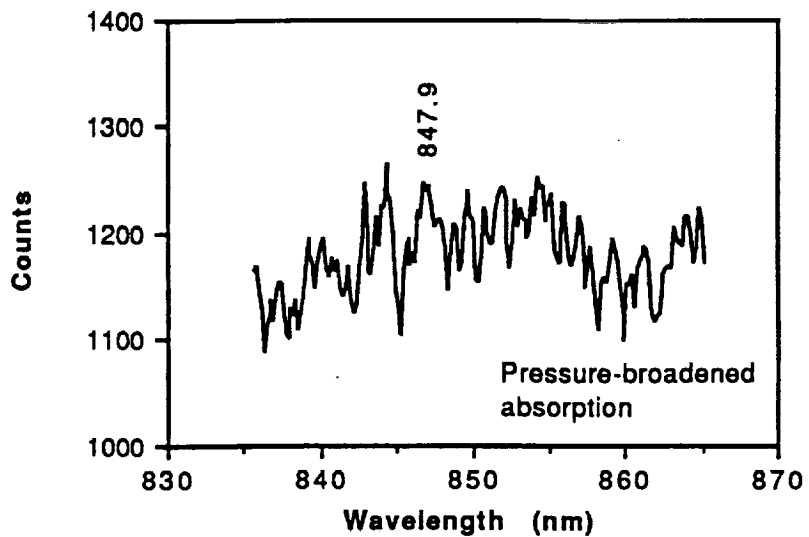
Fig. 36b   Expanded view of absorption and emission bands in the 850 nm region of data set 5.
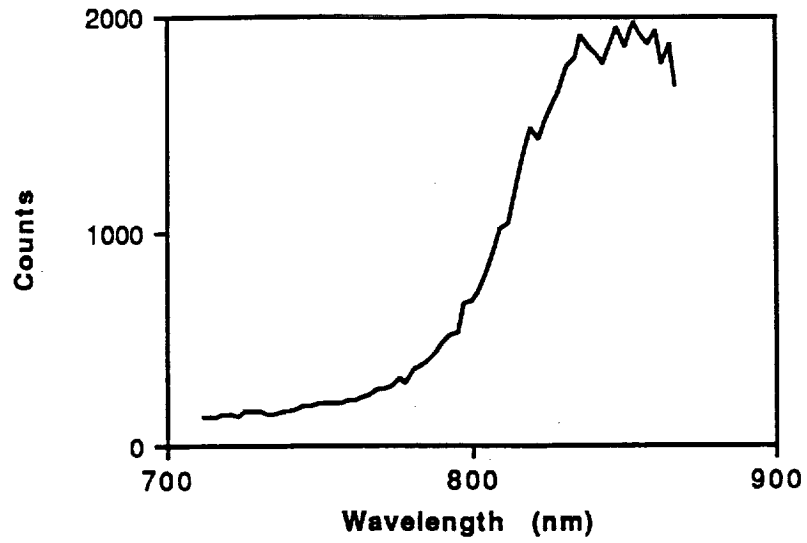
Fig. 37a   Data set 6 reduced from experiment HS789.
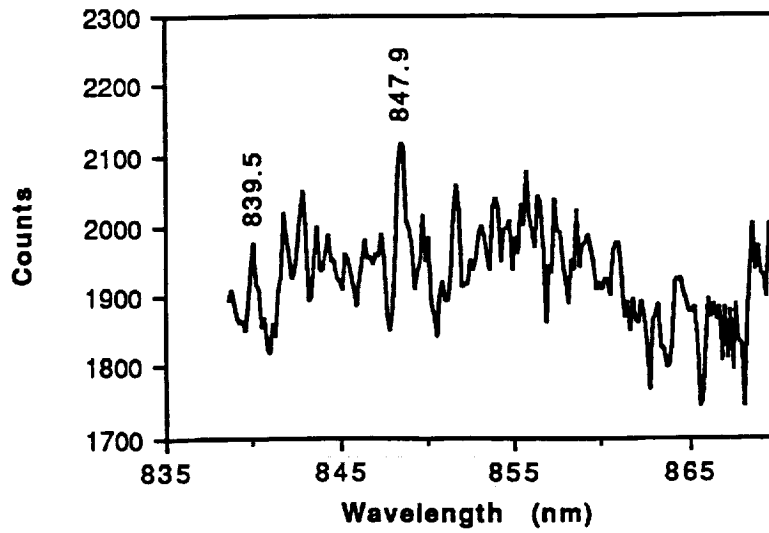
Fig. 37b   Expanded view of absorption and emission bands in the 850 nm region of data set 6.

70
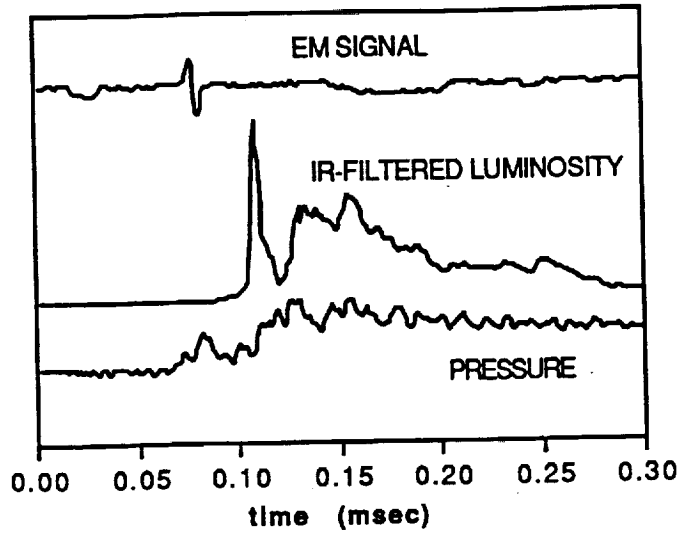
Fig. 37c Pressure, EM, and IR-filtered luminosity data from spectroscopy station in HS789.
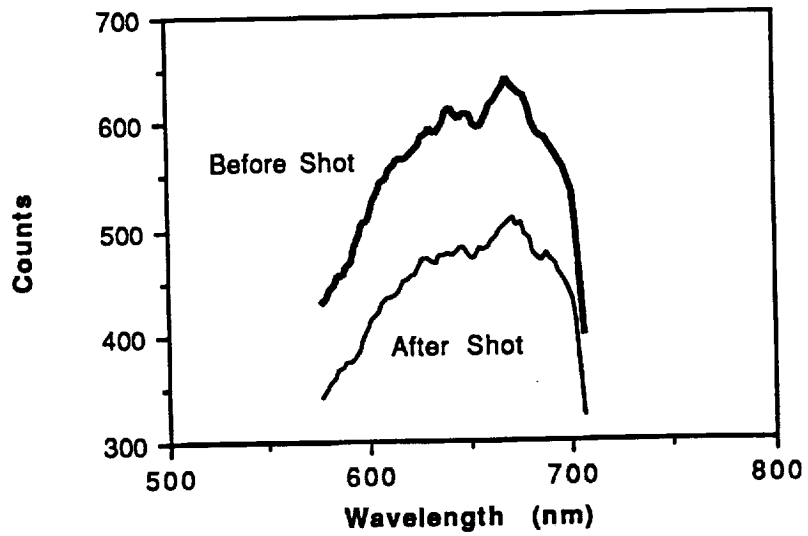
Fig. 38 Attenuation due to soot deposition on face of luminosity probe.

71

SECTION V

CONCLUSION

A preliminary experimental investigation of gasdynamic phenomena associated with the ram accelerator has been accomplished. Three velocity regimes of operation, centered about the Chapman-Jouguet (CJ) detonation speed, have been identified and were found to exhibit distinctive performance characteristics and tube wall data. Subdetonative ram accelerator operation is characterized by a region of high pressure just behind the projectile and an acceleration profile which decreases with increasing velocity, as predicted for the thermally choked propulsive mode. Transdetonative operation begins as the projectile velocity approaches the CJ speed and is characterized by a region of relatively low tube wall pressure behind the projectile with very few variations in amplitude. Combustion activity begins to occur on the projectile body and the acceleration remains nearly constant as the projectile passes through the CJ speed and then increases with increasing projectile velocity. Superdetonative performance is characterized by intense combustion activity on the projectile body, along with increasing amounts of propellant burning on the nose cone as the projectile gains velocity. At low hypersonic Mach numbers ($M < 5.5$) the thrust is observed to increase with increasing projectile velocity, whereas at higher Mach numbers, the acceleration decreases with further increases in projectile velocity, presumably due to excessive forebody drag resulting from combustion on the nose.

The applicability of several diagnostic techniques for examining ram accelerator flow fields has been evaluated in the course of these experimental investigations. The ability of the high instrument density tube to detect the presence of the strong bow shocks standing off the leading edges of the fins and the accompanying intense light emissions makes it invaluable for determining details of ram accelerator flow fields. This diagnostic capability can be used to evaluate the effectiveness of variations in projectile geometry and it allows unsteady gasdynamic phenomena to be closely examined. Thin film thermocouples have been developed which are robust and relatively inexpensive to manufacture. Better calibration techniques are needed to enable quantification of the measurements of the high temperature parts of the flow field. Spectroscopic analysis of the combustion zone has proven to be feasible, though better sensor sensitivity is required to get good temporal resolution of the data. A design for a low cost imaging system based on fiber-optics has been developed which can observe the high pressure flow fields of the accelerating projectiles and digitally store the images for later retrieval and enhancement. Transparent inserts have been tested which have satisfactory optical qualities and sufficient strength to safely contain high pressure combustion and detonation phenomena. The diagnostic techniques

developed during this grant period have indicated that quantitative measurements of ram accelerator flow fields and in-tube images can be simultaneously acquired in a cost-effective manner. These data will be invaluable for understanding the ram accelerator propulsive modes and for validating CFD computer programs designed for hypersonic reacting flow applications.

REFERENCES

1. A.P. Bruckner, D.W. Bogdanoff, C. Knowlen and A. Hertzberg, "Investigation of Gasdynamic Phenomena Associated with the Ram Accelerator Concept," AIAA Paper 87-1327, AIAA 19th Fluid Dynamics, Plasma Dynamics and Lasers Conference, Honolulu, HI, June 8-10, 1987.

2. C. Knowlen, A.P. Bruckner, D.W. Bogdanoff and A. Hertzberg, "Performance Capabilities of the Ram Accelerator," AIAA Paper 87-2152, AIAA/SAE/ASME/ASEE 23rd Joint Propulsion Conference, San Diego, CA, June 29 - July 2, 1987.

3. A. Hertzberg, A.P. Bruckner and D.W. Bogdanoff, "Ram Accelerator: A New Chemical Method for Accelerating Projectiles to Ultrahigh Velocities," *AIAA Journal* **26**:195 (1988).

4. A.P. Bruckner, C. Knowlen, K.A. Scott and A. Hertzberg, "High Velocity Modes of the Thermally Choked Ram Accelerator," AIAA Paper 88-2925, AIAA/ASME/SAE/ASEE 24th Joint Propulsion Conference, Boston, MA, July 11-13, 1988.

5. A.E. Kull, E.A. Burnham, C. Knowlen, A.P. Bruckner, and A. Hertzberg," Experimental Studies of Superdetonative Ram Accelerator Mode," AIAA Paper 89-2632, AIAA/ASME/SAE/ASEE 25th Joint Propulsion Conference, Monterey, CA, July 10-12, 1989.

6. E.A. Burnham, A.E. Kull, C. Knowlen, A.P. Bruckner and A. Hertzberg, "Operation of the Ram Accelerator in the Transdetonative Velocity Regime," AIAA Paper 90-1985, AIAA/SAE/ASME/ASEE 26th Joint Propulsion Conference, Orlando, FL, July 16-18, 1990.

7. A.P. Bruckner, A. Hertzberg and C. Knowlen, "Review of Ram Accelerator Propulsion Modes," 27th JANNAF Combustion Subcommittee Meeting, Warren AFB, Cheyenne, WY, Nov. 5-9, 1990.

8. C. Knowlen, E. Burnham, A.P. Bruckner and A. Hertzberg, "Ram Accelerator Combustion Phenomena," 28th JANNAF Combustion Subcommittee Meeting, Brooks Air Force Base, San Antonio, TX, November 1, 1991.

9. G. Chew, C. Knowlen, E.A. Burnham, A. Hertzberg and A.P. Bruckner, "Experiments on Hypersonic Ramjet Propulsion Cycles up to M=8.5 Using a Ram Accelerator," AIAA Paper 91-2489, AIAA/SAE/ASME/ASEE 27th Joint Propulsion Conference, Sacramento, CA, June 24-26, 1991.

10. A. Hertzberg, A.P. Bruckner and C. Knowlen, "Experimental Investigation of Ram Accelerator Propulsion Modes," *Shock Waves* **1**:17-25, (1991).

11. A.P. Bruckner, C. Knowlen, A. Hertzberg, and D.W. Bogdanoff, "Operational Characteristics of the Thermally Choked Ram Accelerator," *J. Propulsion and Power* **7**:5, pp. 828-836, (1991).

12. C. Knowlen, A.P. Bruckner and A. Hertzberg, "Internal Ballistics of the Ram Accelerator," 13th International Symposium on Ballistics, Stockholm, Sweden, June 1-3, 1992.

13. A.P. Bruckner, E.A. Burnham, C. Knowlen, A. Hertzberg and D.W. Bogdanoff, "Initiation of Combustion in the Thermally Choked Ram Accelerator," 18th International Symposium on Shock Tubes and Waves, Sendai, Japan, July 22-26, 1991.

14. J.B. Hinkey, E.A. Burnham and A.P. Bruckner, "High Spatial Resolution Measurements of Ram Accelerator Gas Dynamic Phenomena," AIAA Paper 92-3244, AIAA/SAE/ASME/ASEE 28th Joint Propulsion Conference and Exhibit, Nashville, TN, July 6-8, 1992.

15. J. Auzias de Turenne, G. Chew and A.P. Bruckner, "Recent Results from the University of Washington's 38 mm Ram Accelerator," AIAA Paper 92-3782, AIAA/SAE/ASME/ASEE 28th Joint Propulsion Conference and Exhibit, Nashville, TN, July 6-8, 1992.

16. D.C. Brackett and D.W. Bogdanoff, "Computational Investigation of Oblique Detonation Ramjet-in-Tube Concepts," *J. Propulsion and Power* 5:3, (1988).

17. S. Yungster and A.P. Bruckner, "Computational Studies of a Superdetonative Ram Accelerator Mode," *J. Propulsion and Power* 8:2, pp. 457-463, (1992).

18. S. Yungster, S. Eberhardt and A.P. Bruckner, "Numerical Simulation of Shock-Induced Combustion Generated by High-Speed Projectiles in Detonable Gas Mixtures," AIAA Paper 89-0673, 1989.

19. A.P. Bruckner, C. Knowlen and A. Hertzberg, "Applications of the Ram Accelerator to Hypervelocity Aerothermodynamic Testing," AIAA Paper 92-3949 AIAA 17th Ground Testing Conference, Nashville, TN, July 6-8, 1992.

20. R.D. Witcofski, W.I. Scallion, D.J. Carter, and R.W. Courter, "An Advanced Hypervelocity Aerophysics Facility: A Ground-Based Flight Test Range," AIAA Paper 91-0296, January 1991.

21. Bogdanoff, D.W., "Ram Accelerator Direct Space Launch System: New Concepts," *J. Propulsion and Power,* Vol. 8, 1992, pp. 481-490.

22. P. Kaloupis and A.P. Bruckner, "The Ram Accelerator: A Chemically Driven Mass Launcher," AIAA Paper 88-2968, AIAA/ASME/SAE/ASEE 24th Joint Propulsion Conference, Boston, MA, July 11-13, 1988.

23. A.P. Bruckner and A. Hertzberg, "The Ram Accelerator as a Space Cargo Launcher," NIST Conference on Reducing the Cost of Space Infrastructure and Operations, Gaithersburg, MD, Nov. 20-22, 1989.

24. A. Hertzberg, A.P. Bruckner and D.W. Bogdanoff, "An Exploratory Study of Ram Accelerator Principles," Air Force Armament Laboratory Final Report No. AFATL-TR-88-94, October 1988.

25. A.P. Bruckner and A. Hertzberg, "Investigation of Superdetonative Ram Accelerator Drive Modes,:" Final Report, ONR Contract No. N00014-88-K-0565, July 1, 1988 - June 30, 1989.

26. C. Knowlen, "Theoretical and Experimental Investigation of the Thermodynamics of the Thermally Choked Ram Accelerator," Doctoral Dissertation, Department of Aeronautics and Astronautics, University of Washington, Seattle, WA, 1991.

27. C. Knowlen and A.P. Bruckner, "A Hugoniot Analysis of the Ram Accelerator," 18th International Symposium on Shock Tubes and Waves, Sendai, Japan, July 22-26, 1991.

28. C. Knowlen, J.G. Li, J. Hinkey and B. Dunmire, "University of Washington Ram Accelerator Facility," 42nd Meeting of the Aeroballistic Range Association, Adelaide, Australia, October 22-25, 1991.

29. D.W. Bogdanoff, C. Knowlen, D. Murakami, and I. Stonich, "Magnetic Detector for Projectiles in Tubes," *AIAA Journal* **28**(11):1942 (1990).

30. E. Christofferson, "A Magnetic Transducer Detection System for High Speed Projectiles in Tubes," M.S.A.A. Thesis, Department of Aeronautics and Astronautics, University of Washington, Seattle, WA, December 1989.

31. K.A. Scott, "Experimental Investigation of Ram Accelerator Concept Using an Optical Probe," M.S.A.A. Thesis, Department of Aeronautics and Astronautics, University of Washington, Seattle, WA, 1988.

32. R.J. McIntosh, "A Microsecond Response Thermocouple For Use in the Ram Accelerator," M.S.A.A. Thesis, Department of Aeronautics and Astronautics, University of Washington, Seattle, WA, 1991.

33. D. Bendersky, "A Special Thermocouple for Measuring Transient Temperatures," *Mechanical Engineering*, Vol. 75, No. 2, Feb. 1953, pp. 117-121.

34. J.G. Hall and A. Hertzberg, "Recent Advances in Transient Surface Temperature Thermometry," *Jet Propulsion*, Nov. 1958.

35. American Society for Testing and Materials, "Manual on the Use of Thermocouples in Temperature Measurement," ASTM, Philadelphia, PA, 1981.

36. A.E. Prochko, "Preliminary Spectral Analysis of the Ram Accelerator," M.S.A.A. Thesis, Department of Aeronautics and Astronautics, University of Washington, Seattle, WA, 1991.

37. M.J. Webb, "Practical Considerations When Using Fiber Optics with Spectrometers," *Spectroscopy*, Vol. 4, No. 6, 1989, pp. 26-34.

38. E.A. Burnham, J.B. Hinkey, and A.P. Bruckner, "Investigation of Starting Transients in the Thermally Choked Ram Accelerator," 29th JANNAF Combustion Subcommittee Meeting, NASA Langley Research Center, Hampton, VA, October 19-23, 1992.

39. J.B. Hinkey, E.A. Burnham, and A.P. Bruckner, "High Spatial Resolution Measurements in a Single-Stage Ram Accelerator," 29th JANNAF Combustion Subcommittee Meeting, NASA Langley Research Center, Hampton, VA, October 19-23, 1992.

40. R. Siegel and J.R. Howell, Thermal Radiation Heat Transfer, 2nd ed., Hemisphere Publishing Corp., New York, 1981.

41. G. Herzberg, Molecular Spectra and Molecular Structure, Vol. 1, D. Van Nostrand Co., Inc., Princeton, N.J., 1959.

APPENDIX A

A HUGONIOT ANALYSIS OF THE RAM ACCELERATOR

A HUGONIOT ANALYSIS OF THE RAM ACCELERATOR

C. Knowlen and A.P. Bruckner
Aerospace and Energetics Research Program
University of Washington, FL-10
Seattle, WA 98195

ABSTRACT

The thermodynamic properties of a combustible propellant gas, after it has been processed by a ram accelerator propulsive mode, are related by a "ram accelerator Hugoniot" expression. These end states are determined from the 1-D conservation equations in a manner similar to that used for detonation waves, but with the addition of a force term in the momentum equation. Establishment of a region of potentially accessible thermodynamic end states that are consistent with ram accelerator operation at and above the Chapman-Jouguet detonation speed indicates that there are no fundamental constraints on accelerating projectiles over a wide range of Mach numbers in a single propellant mixture. Interpreting experimental data in the context of a generalized ram accelerator process leads to relatively simple propulsive models which can predict the projectile acceleration of any propulsive mode. The projectile velocity and acceleration histories determined by the Hugoniot analysis for the thermally choked ram accelerator mode are in excellent agreement with experiments.

INTRODUCTION

A ram accelerator is a ramjet-in-tube means for accelerating projectiles to high velocities through a stationary tube filled with a combustible propellant gas (Hertzberg et al, 1987, 1988). In general, a ram accelerator propulsive mode is any adiabatic aerothermodynamic cycle established by the interaction of a subcaliber projectile traveling supersonically through a gaseous combustible mixture in a stationary tube. The net result of such a cycle is to produce a change in the stream thrust (defined here as the sum of the axial momentum flux and static pressure) of the propellant gas after it reacts and returns to the full tube area. The high temperature exhaust gas moves away from the projectile and its combustion zone at sonic or supersonic velocities. In this manner expansion waves originating behind the projectile cannot overtake and affect the established flow conditions.

A schematic of the flowfield of the thermally choked ram accelerator (TCRA) mode is shown in Fig. 1. This propulsive cycle operates at velocities below the Chapman-Jouguet (CJ) detonation velocity and in the Mach number range of 2.5 to 4.5. In the projectile reference frame supersonic flow passes over the projectile throat and encounters a normal shock, which renders the flow subsonic. Combustion is assumed to be stabilized behind the projectile by the flame-holding ability of the flat projectile base and sufficient heat is added to thermally choke the subsonic flow. Because of the relative simplicity of igniting the propellant behind the projectile (Bruckner et al, 1991) and its low Mach number operating ability, the TCRA mode was the first ram accelerator propulsive cycle to be investigated experimentally (Hertzberg et al, 1987, 1988).

If all of the combustion activity occurs on the projectile body then the exit Mach number must be supersonic to isolate the flowfield from downstream disturbances. Subsonic combustion on the projectile can be stabilized if the flow reaches sonic velocity with respect to the projectile somewhere on the body. A nozzle is used to establish subsonic flow through the midbody combustion zone of the nozzle choked ram accelerator mode shown in Fig. 2 (Knowlen et al, 1987; Knowlen, 1991). Ideally, this propulsive cycle has a constant supersonic exit Mach number that is determined by the area ratio of the nozzle. Since the area ratio of the combustion zone can be readily specified, the end state of any propulsive mode using

supersonic combustion can, in principle, be generated with an appropriately shaped nozzle choked ram accelerator projectile. This makes the nozzle choked propulsive mode a useful model for investigating the consequences of operating ram accelerator propulsive cycles beyond the CJ speed (Knowlen, 1991).

RAM ACCELERATOR HUGONIOT

Analysis of the thermodynamics of the general ram accelerator process is carried out in a manner similar to that used for 1-D shock and detonation waves (Shapiro, 1953), but with the addition of a force term in the momentum equation. The inviscid gasdynamic conservation equations are applied across the control volume shown in Fig. 3, which consists of an entrance plane (1), an exit plane (2) and an unrestrained body centered in a straight-walled section of tube. The increase in the stream thrust of the reacted propellant mixture, after the gas has ceased to communicate with the projectile, corresponds to the maximum amount of axial force that can be applied to accelerate the projectile (Rudnick, 1947). This acceleration is sufficiently low for experimentally realizable conditions that the end state of the propellant mixture can be determined from steady flow computations (Bruckner et al, in press).

The ram accelerator Hugoniot equation can be expressed in terms of a non-dimensional thrust parameter I, or "impulse," defined as the ratio of thrust to the product of fill pressure and tube cross-sectional area, as follows:

$$h_2 - h_1 = \Delta q + \frac{v_1 + v_2}{2}\left(p_2 - p_1(I+1)\right) \tag{1}$$

where h is the static enthalpy, Δq is the heat release per unit mass, v is the specific volume and p is the static pressure. This equation has the impulse, I, as a parameter and is completely independent of the choice of the equation of state or of the process occurring between stations 1 and 2. All of the ram accelerator propulsive modes have end states that lie on a ram accelerator Hugoniot curve.

A non-dimensional heat release parameter is defined as $Q = \Delta q/c_{p1}T_1$, where c_{p1} and T_1 are, respectively, the constant pressure heat capacity and static temperature of the unreacted propellant. Normalizing the intensive thermodynamic variables at the exit (2) to those incoming (1), allows the pressure-specific volume (P-V) relationship for the ram accelerator Hugoniot to be put into non-dimensional form for an ideal gas as follows:

$$P = \frac{\dfrac{2\gamma_1}{\gamma_1 - 1}(Q+1) - (V+1)(I+1)}{V\left(\dfrac{2\gamma_2}{\gamma_2 - 1} - 1\right) - 1} \tag{2}$$

where γ_1 and γ_2 are the ratios of specific heats at (1) and (2), respectively, $P = p_2/p_1$ and $V = v_2/v_1$. Equation 2 represents the locus of end states of an arbitrary 1-D flow process in which heat is added by chemical reactions and momentum is gained or lost. The detonation Hugoniot is recovered from this equation when I=0 and the normal shock Hugoniot results when both I and Q equal zero (Strehlow, 1984). The Hugoniots shown in Fig. 4 are represented in the P-V plane by contours of constant Q and I. Each curve includes the end states of all ram accelerator modes that generate the specified impulse for the given non-dimensional heat release. Three representative Hugoniots (I = 3,6,9), based on Q=6 and a constant specific heat ratio of 1.4, have been plotted in Fig. 4 along with the corresponding normal shock (I=Q=0) and detonation (I=0,Q=6) Hugoniots to illustrate the effects of momentum change on the end state of the propellant.

79

GENERALIZED RAYLEIGH FLOW

A steady transformation from state 1 to state 2 of a truly 1-D flow is restricted to occur through states which lie on a straight line connecting the initial and final conditions in the P-V plane. The equation for this line is determined from the mass and momentum conservation equations (with I=0) and is commonly referred to as the *Rayleigh line*. End states of a steady flow that is acted upon by an intermediate process that changes its momentum before allowing the flow to continue in the same direction with the same mass flux lie along a straight line in the P-V plane that will be referred to as the "generalized Rayleigh line," which can be expressed as follows:

$$P = I + 1 + \gamma_1 M_1^2 (1 - V) \qquad (3)$$

The generalized Rayleigh lines for two different ram accelerator modes that generate an impulse of I=3, with a propellant gas having constant γ=1.4, are illustrated in Fig. 5 along with a sample Hugoniot having I=3 and Q=6. The intersection points with the Hugoniot curve indicate the end state of the propellant gas after it has been processed by a ram accelerator mode generating the specified I with a given Q, at a particular in-tube Mach number, M_1, and the minimum operating velocity is determined from the generalized Rayleigh line that lies tangent to the Hugoniot. It can be shown that this tangent point corresponds to sonic exit flow conditions, and that all points above on the Hugoniot curve are subsonic and the points below are supersonic end states (Knowlen, 1991).

Analysis of Eq. 3 shows that the generalized Rayleigh line intercepts the V=1 line at the point (1, I+1) and has a slope that depends on the initial state of the gas and the square of the incoming Mach number of the flow; i.e., $dP/dV = -\gamma_1 M_1{}^2$. The incoming flow velocity and corresponding mass flux increase as the negative slope of the generalized Rayleigh line increases, and the V=1 line represents a flow having an infinite mass flux. Thus, the intersection point of the ram accelerator Hugoniot curve with the V=1 line indicates the minimum pressure ratio that could result from a ram accelerator mode that reduces the specific volume of the propellant gas. Note that the generalized Rayleigh line does not pass through the initial point (1,1) when I≠0 (see Fig. 5). The inability of the flow to make a transition continuously from the initial state to its end state along a path in the P-V plane represented by a straight line, when there is a momentum change, indicates that there must be intermediate processes involved which are not 1-D to bring about the necessary changes in steady flow.

GENERALIZED FANNO FLOW

Thermodynamic end state histories in the P-V plane that a particular ram accelerator propulsive mode will generate, as it accelerates a projectile through a given velocity range, can be determined from the mass and energy conservation equations. The term *Fanno flow* is often associated with steady adiabatic flow in a constant area duct that experiences a change in momentum flux due to frictional effects in the absence of internal heat generation. Combining the ideal gas equation of state with the conservation equations of mass and energy, while leaving a heat release term in the energy equation, results in the following expression for a "generalized Fanno curve:"

$$P = \frac{\dfrac{\gamma_1(\gamma_2 - 1)}{\gamma_2(\gamma_1 - 1)} V(Q + 1)}{V^2\left(1 + \dfrac{\gamma_2 - 1}{2} M_2^2\right) - \dfrac{\gamma_2 - 1}{2} M_2^2} \qquad (4)$$

A series of these curves can be drawn using the exit Mach number, M_2, as a parameter which represent the history of P-V states that different ram accelerator modes produce while operating in the same propellant gas. Examples of three generalized Fanno curves in a propellant having a heat release of $Q=6$ are shown in Fig. 6. The curve labeled by $M_2=1$ corresponds to the TCRA mode and the curves labeled by $M_2=2$ and $M_2=3$ correspond to projectile geometries operating in the nozzle choked ram accelerator mode, which have the nozzle throat-to-tube area ratios required to accelerate the reacted propellant gas ($\gamma=1.4$) to exit Mach numbers of 2 and 3, respectively. All of the generalized Fanno curves intersect the V=1 line at the same point that the Hugoniot characterized by I=Q does, which indicates that end state conditions generated by any ram accelerator mode will be the same at the constant specific volume point of operation (Fig. 6). Detailed flow interactions with the body configuration must be considered in order to determine the feasibility of a particular ram accelerator propulsive mode actually generating the acceleration level corresponding to I=Q (Knowlen, 1991).

Since the locus of end states described by the generalized Fanno curve of the TCRA mode indicates points along the ram accelerator Hugoniots where the exit velocity is sonic, and this curve remains at or above the I=Q Hugoniot in the P-V plane (Fig. 6), there cannot be any steady ram accelerator process which generates a value of impulse greater than Q when V<1. Thus, the maximum impulse ram accelerator Hugoniot is characterized by I=Q, for a propellant mixture having a constant γ, and the generalized Fanno curve representing the TCRA mode forms the leftmost boundary of the region of the allowable end states in the P-V plane for any ram accelerator mode having sonic or supersonic exit velocities.

The detonation Hugoniot (I=0,Q=6) shown in Fig. 6 represents the maximum end state pressure ratios that can be developed by any ram accelerator process. The upper Mach number limit of any ram accelerator mode that has a constant M_2 corresponds to the Mach number of the "weak detonation wave" (defined here as a supersonic combustion wave which has supersonic outflow when moving at a steady velocity (Strehlow, 1984)) that has the same M_2 after supersonic heat addition. The TCRA mode has an upper velocity limit that is equivalent to the CJ speed of the gaseous propellant, and ram accelerator modes with supersonic outflows have the potential to attain velocities much greater than the CJ speed.

RAM ACCELERATOR IMPULSE EQUATION

The general expression for the impulse of any ram accelerator mode is determined from the jump conditions across the control volume (Fig. 3) as a function of flow Mach numbers, specific heat ratios, and the non-dimensional heat parameter as follows:

$$I = \frac{\gamma_1 M_1}{\gamma_2 M_2}\left(1 + \gamma_2 M_2^2\right)\sqrt{\left(\frac{\gamma_2 - 1}{\gamma_1 - 1}\right)\frac{Q + 1 + \frac{\gamma_1 - 1}{2}M_1^2}{1 + \frac{\gamma_2 - 1}{2}M_2^2}} - \left(1 + \gamma_1 M_1^2\right) \qquad (5)$$

This impulse equation applies to all ram accelerator propulsive modes, even though no details of the internal flow have been considered. If one knows how M_2 varies with M_1 in a given propellant mixture, then the projectile thrust can be readily estimated for any flight velocity. Conversely, determining the projectile acceleration-velocity history from experiments allows the end state Mach number of any propulsive cycle to be estimated. The details of the flowfield around the projectile must be considered to accurately predict M_2 for the supersonic combustion and oblique detonation modes (Yungster and Bruckner, 1989). However, thermal choking of the flow behind the projectile corresponds to a state of maximum entropy (Landau and Lifshitz, 1984); thus, the details of the process which brings the flow to

81

choking do not affect the end state conditions of the TCRA mode. This leads to the apparent paradox that the acceleration performance of the TCRA mode is independent of diffuser efficiency, which is true, as long as the projectile geometry can support a shock wave system that does not unstart the flow around the projectile (Knowlen, 1991).

The insensitivity of the TCRA performance to projectile geometry is demonstrated by the non-dimensional thrust plots shown in Fig. 7 for three different projectile configurations operated in a 38 mm bore, 16 m long tube using a propellant mixture that nominally consists of $2.7CH_4 + 2O_2 + 5.8N_2$, which has a 1700 m/sec CJ speed. Each projectile had the same throat-to-tube and base-to-tube area ratios but different body lengths and cone angles. The cone half-angles were 8°,10° and 12° and they were attached to bodies having lengths of 2.2, 1.9, and 1.7 tube diameters, respectively. The experimental impulse measurements are plotted against projectile velocity normalized to CJ speed. The last data point on the right-hand side of the plots corresponds to the velocity of the projectile as it exited ram accelerator tube. Close agreement with theory is demonstrated by all three experiments at velocities below 90% CJ speed, which strongly indicates that the projectiles were accelerated with a thermally choked propulsive cycle in this velocity regime.

The projectile with an 8° nose cone experienced a thrust minimum near the CJ speed, after which its thrust increased with increasing velocity (Fig. 7). The other two projectiles demonstrated the same tendency for the thrust profile to flatten out near the CJ speed, however, they left the accelerator tube with a trend of decreasing thrust with increasing velocity. The differences in the acceleration behavior near the detonation velocity indicate that the projectile external configuration may be significant in this flight regime. It is believed that at velocities approaching the CJ speed, combustion occurs in mixed supersonic and subsonic flow at the base of the projectile, and that the flow ceases to be thermally choked (Hertzberg et al, 1991; Chew et al, 1991; Nusca, 1991).

CONCLUSION

The ram accelerator Hugoniot analysis determines how the end state properties of the propellant gas behave as a function of the initial Mach number, heat release, and non-dimensional thrust of an arbitrary ram accelerator mode operating in a constant area tube. Resulting performance limitations indicate the widest possible bounds of operation that are consistent with steady, 1-D inviscid flow assumptions, without considering the internal details of the flow processes involved. Theoretically, the thermally choked propulsive mode ceases to accelerate the projectile at the CJ speed, and a nozzle choked propulsive cycle that produces a constant exit Mach number is limited to the velocity of the particular weak detonation wave that has the same exiting flow conditions. The excellent agreement between experimental acceleration profiles of projectiles having various geometries and the 1-D theoretical predictions at velocities below ~90% CJ speed indicates that a thermally choked propulsive cycle is operating in this velocity range, and it confirms that unsteady effects arising at these acceleration levels do not alter the end state conditions predicted for steady flow.
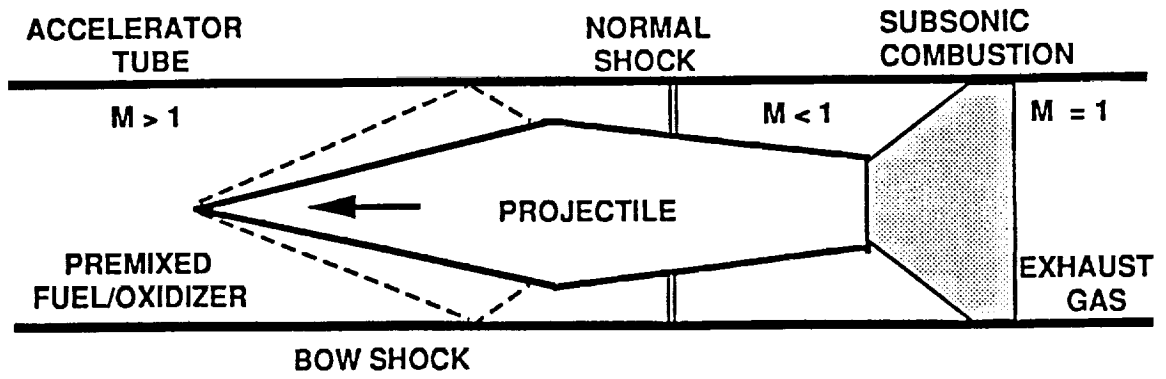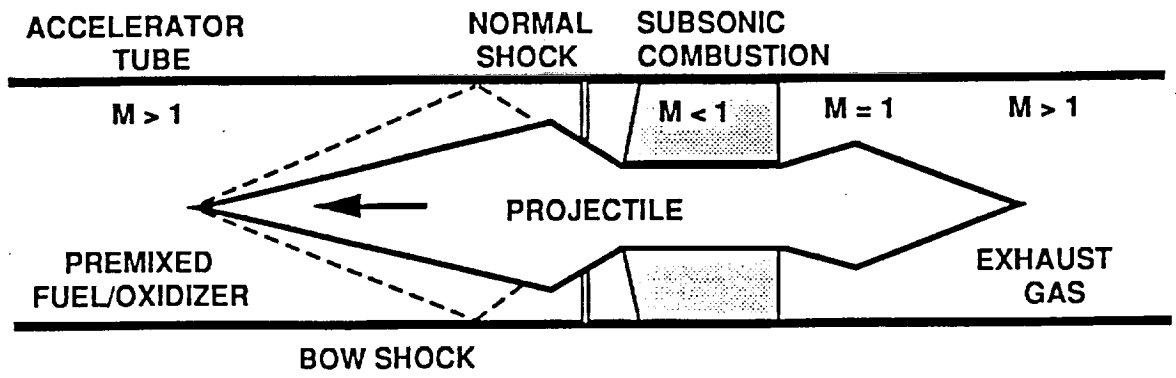
REFERENCES

Bruckner AP, Burnham EA, Knowlen C, Hertzberg A, Bogdanoff DW (1991) Initiation of combustion in the thermally choked ram accelerator. Proc. 18th Intl. Symp. Shock Waves

Bruckner AP, Knowlen C, Hertzberg A, Bogdanoff DW (in press) Operational characteristics of the thermally choked ram accelerator. J. Propulsion & Power

Chew G, Knowlen C, Burnham EA, Hertzberg A, Bruckner AP (1991) Experiments on hypersonic ramjet propulsive cycles using a ram accelerator. AIAA Paper 91-2489
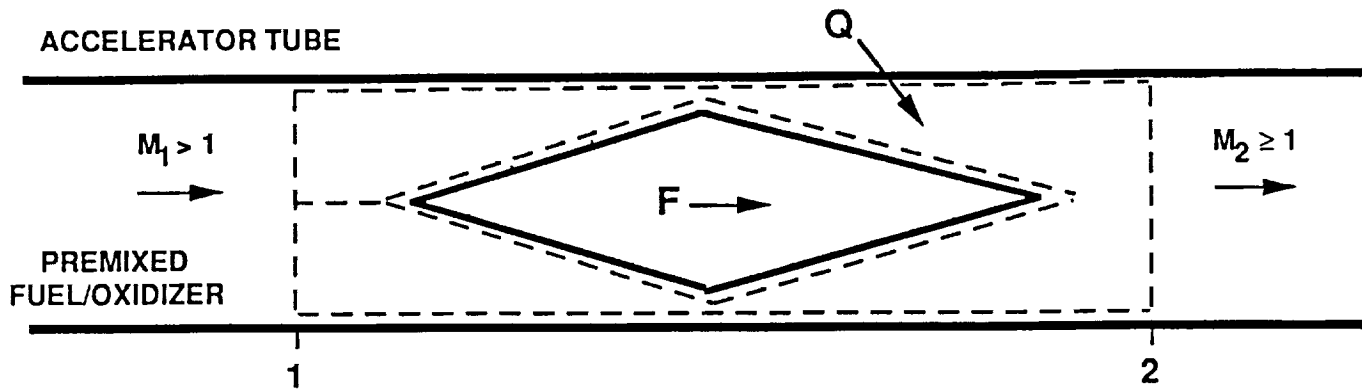
Hertzberg A, Bruckner AP, Bogdanoff DW (1988) Ram accelerator: A new chemical method for accelerating projectiles to ultrahigh velocities. AIAA J. **26**:195-203

Hertzberg A, Bruckner AP, Bogdanoff DW, Knowlen C (1987) The ram accelerator and its applications. Proc. 16th Intl. Symp. Shock Tubes and Waves; p. 117-28.

Hertzberg A, Bruckner AP, Knowlen C (1991) Experimental investigation of ram accelerator propulsion modes. Shock Waves **1**:17-25

Knowlen C (1991) Theoretical and experimental investigation of the thermodynamics of the thermally choked ram accelerator. Phd. Dissertation, University of Washington.

Knowlen C, Bruckner AP, Bogdanoff DW, Hertzberg A (1987) Performance capabilities of the ram accelerator. AIAA Paper 87-2152

Landau LD, Lifshitz EM (1984) Fluid Mechanics (Oxford: Pergamon Press) p. 319-32, 337-41, 347-53, 480-96

Nusca MJ (1991) Numerical simulation of reacting flow in a thermally choked ram accelerator projectile launch system. AIAA Paper 91-2490

Rudnick P (1947) Momentum relations in propulsive ducts. J. Aeronautical Sciences **14**:540-4

Shapiro AH (1953) The Dynamics and Thermodynamics of Compressible Fluid Flows (New York: Ronald Press) p. 73-262, 689-98

Strehlow RA (1984) Combustion Fundamentals (New York: McGraw-Hill) p. 114-39, 302-36, 360-4

Yungster S, Bruckner AP (1989) A numerical study of the ram accelerator concept in the superdetonative velocity range. AIAA Paper 89-2677
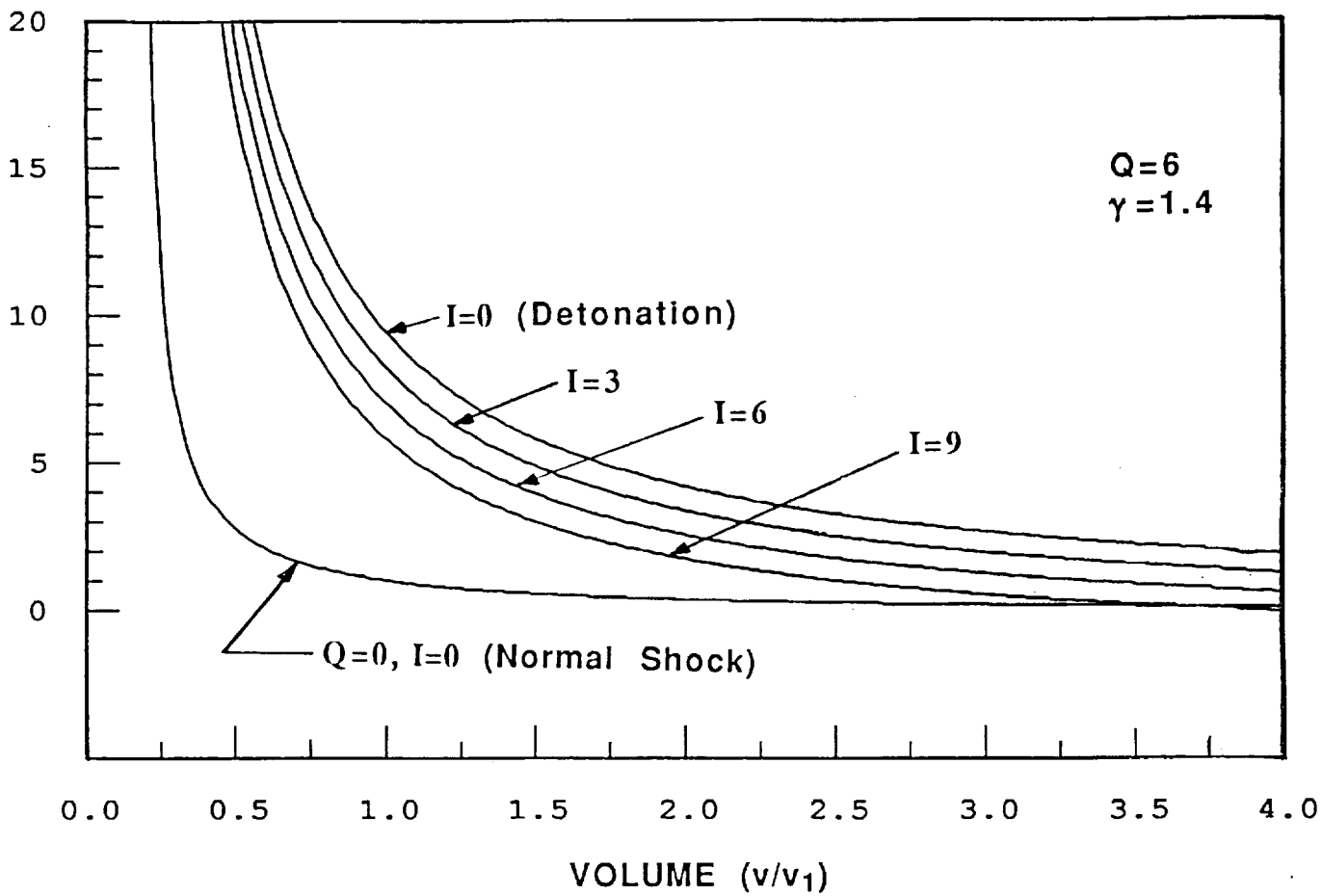
FIGURE CAPTIONS

Fig. 1 Thermally choked ram accelerator mode.

Fig. 2 Nozzle choked ram accelerator mode.

Fig. 3 Control volume for the general ram accelerator process.

Fig. 4 Effects of impulse generation on ram accelerator Hugoniots of a given propellant mixture.

Fig. 5 Generalized Rayleigh lines corresponding to two different ram accelerator modes.

Fig. 6 Generalized Fanno curves of ram accelerator modes having different exit Mach numbers.

Fig. 7 Experimental non-dimensional thrust profiles for three different projectile configurations.

ACCELERATOR TUBE NORMAL SHOCK SUBSONIC COMBUSTION

M > 1

PREMIXED FUEL/OXIDIZER

PROJECTILE

M < 1

M = 1

EXHAUST GAS

BOW SHOCK

ACCELERATOR TUBE   NORMAL SHOCK   SUBSONIC COMBUSTION

M > 1   M < 1   M = 1   M > 1

PROJECTILE

PREMIXED FUEL/OXIDIZER   EXHAUST GAS

BOW SHOCK

KNOWLEN et al.   Fig. 2

ACCELERATOR TUBE

$M_1 > 1$

PREMIXED
FUEL/OXIDIZER

Q

$F \longrightarrow$

$M_2 \geq 1$

1

2

KNOWLEN et al.

Fig. 3

Fig. 4

KNOWLEN et al.

Fig. 5

KNOWLEN et al.

Q=6 $\gamma = 1.4$

Generalized Fanno Curves
- - - $M_2 = 1$
- · - $M_2 = 2$
- - $M_2 = 3$

$I = 6$

$I = 0$

$(1, Q+1)$

PRESSURE (p/p_1)

VOLUME (v/v_1)

KNOWLEN et al.

89

C-2

Fig. 6

Fig. 7

NON-DIMENSIONAL THRUST (F/p_1A)

NON-DIMENSIONAL VELOCITY (U/U_{CJ})

Nominal Propellant Mixture
2.7CH_4 + 2O_2 + 5.8N_2

— Theory

Cone Angle	Body Length
△ 8°	84 mm
□ 10°	71 mm
○ 12°	64 mm

KNOWLEN et al.

APPENDIX B

PUBLICATIONS SUPPORTED BY CONTRACT

E. Christofferson, "A Magnetic Transducer Detection System for High Speed Projectiles in Tubes," M.S.A.A. Thesis, Department of Aeronautics and Astronautics, University of Washington, Seattle, WA, December 1989.

E.A. Burnham, A.E. Kull, C. Knowlen, A.P. Bruckner and A. Hertzberg, "Operation of the Ram Accelerator in the Transdetonative Velocity Regime," AIAA Paper 90-1985, AIAA/SAE/ASME/ASEE 26th Joint Propulsion Conference, Orlando, FL, July 16-18, 1990.

A.P. Bruckner, A. Hertzberg and C. Knowlen, "Review of Ram Accelerator Propulsion Modes," 27th JANNAF Combustion Subcommittee Meeting, Warren AFB, Cheyenne, WY, Nov. 5-9, 1990.

A.P. Bruckner, C. Knowlen, A. Hertzberg, and D.W. Bogdanoff, "Operational Characteristics of the Thermally Choked Ram Accelerator," *J. Propulsion and Power* **7**:5, pp. 828-836, (1991).

A. Hertzberg, A.P. Bruckner and C. Knowlen, "Experimental Investigation of Ram Accelerator Propulsion Modes," *Shock Waves* **1**:17-25, (1991).

C. Knowlen, "Theoretical and Experimental Investigation of the Thermodynamics of the Thermally Choked Ram Accelerator," Doctoral Dissertation, Department of Aeronautics and Astronautics, University of Washington, Seattle, WA, 1991.

G. Chew, C. Knowlen, E.A. Burnham, A. Hertzberg and A.P. Bruckner, "Experiments on Hypersonic Ramjet Propulsion Cycles up to M=8.5 Using a Ram Accelerator," AIAA Paper 91-2489, AIAA/SAE/ASME/ASEE 27th Joint Propulsion Conference, Sacramento, CA, June 24-26, 1991.

R.J. McIntosh, "A Microsecond Response Thermocouple For Use in the Ram Accelerator," M.S.A.A. Thesis, Department of Aeronautics and Astronautics, University of Washington, Seattle, WA, 1991.

A.E. Prochko, "Preliminary Spectral Analysis of the Ram Accelerator," M.S.A.A. Thesis, Department of Aeronautics and Astronautics, University of Washington, Seattle, WA, 1991.

C. Knowlen and A.P. Bruckner, "A Hugoniot Analysis of the Ram Accelerator," 18th International Symposium on Shock Tubes and Waves, Sendai, Japan, July 22-26, 1991.

A.P. Bruckner, E.A. Burnham, C. Knowlen, A. Hertzberg and D.W. Bogdanoff, "Initiation of Combustion in the Thermally Choked Ram Accelerator," 18th International Symposium on Shock Tubes and Waves, Sendai, Japan, July 22-26, 1991.

C. Knowlen, J.G. Li, J. Hinkey and B. Dunmire, "University of Washington Ram Accelerator Facility," 42nd Meeting of the Aeroballistic Range Association, Adelaide, Australia, October 22-25, 1991.

C. Knowlen, E. Burnham, A.P. Bruckner and A. Hertzberg, "Ram Accelerator Combustion Phenomena," 28th JANNAF Combustion Subcommittee Meeting, Brooks Air Force Base, San Antonio, TX, November 1, 1991.